universität wien

DIPLOMARBEIT

Titel der Diplomarbeit

Connections between Cell Mechanics and Chromatin Condensation in Embryonic Stem Cells

Verfasser

Markus Höpfler

angestrebter akademischer Grad

Magister der Naturwissenschaften (Mag. rer. nat.)

Wien, 2011

Studienkennzahl:	A 490
Studienrichtung:	Diplomstudium Molekulare Biologie
Betreuer:	Ao. Univ.-Prof. Dr. Friedrich Propst

Acknowledgments

I sincerely thank Jochen Guck for giving me the opportunity to do the research work for my diploma thesis in his group at the Cavendish Laboratory, University of Cambridge, and for inspiring discussions about our work and science in general. I particularly also thank Kevin Chalut who taught me invaluable skills, motivated me to pursue my experiments with persistence and who also became a good friend outside the lab.

I also thank Graeme, Franzi, Thorsten, Andrew, Ulysse and many others for help in the lab and with data analysis and all the group members for helpful discussions. Special thanks also go to Graeme and Dino, who always came up with good ideas in numerous coffee breaks and also made life in Cambridge outside the lab a lot more fun (together with many others!). Thanks also to Franzi, who gave me a very warm welcome in Cambridge and a first shelter and was critically involved in proofreading this thesis.

I am grateful to Prof. Propst who supervised this work from my home university and was very helpful especially in the funding application process. The University of Vienna helped me in doing this research project with financial support.

Finally, and most importantly, I thank my family for all their support throughout my studies. I have always been encouraged in my decisions and without their financial support, my studies and this work would have hardly been possible.

Zu guter Letzt danke ich meiner Familie für all die Unterstützung während meines Studiums. Ich wurde immer unterstützt in meinen Entscheidungen und ohne ihre finanzielle Hilfe wäre mein Studium und diese Arbeit kaum möglich gewesen.

Abstract

Pluripotency is a key feature of embryonic stem (ES) cells and the founder tissue of the embryo proper, the epiblast. The characterization of the properties of pluripotent cells and the molecular regulation of this state has inspired much research over the last decades. Here, we used a mix of well established and novel techniques to investigate biophysical changes that occur in the transcriptionally heterogeneous state of pluripotency in mouse ES cells even before differentiation.

The expression levels of Nanog, a transcription factor that stabilizes pluripotency, can distinguish two states of pluripotency: Cells with high Nanog expression are in a stable pluripotent state while cells with low levels are prone to differentiate. We found that differentiation-prone cells are softer on average as compared to stable pluripotent cells when we tested global cell mechanics by optical stretching. The cytoskeleton is usually critical in determinining mechanical properties of cells; therefore, we investigated the structure of the cytoskeleton in ES cells but we found no detectable difference between the two states in immunohistochemical stainings of attached and suspended cells. Furthermore, we ruled out that changes in proliferation speed or in the relative amounts of nuclear and cytoplasmatic volume caused the observed effect.

The role of nuclear stiffness on overall cell mechanics is not well understood, however, nuclei in ES cells are comparably big and so we considered a role of nuclei in cell compliance. To probe nuclear mechanics, we demonstrated a novel method that allows to stretch nuclei within intact cells. Indeed, we found changes of the response of nuclei to stretching forces that are in line with cell mechanics changes. To assess nuclear substructure, we analyzed chromatin structure by testing histone mobility using fluorescence recovery after photobleaching of a tagged histone and analyzing the distribution of the heterochromatin marker HP1α in ES nuclei. The results of both assays agree well in that chromatin was more condensed in the stable pluripotent state where cells and nuclei were stiffer. We used chemical treatments to change chromatin condensation and showed that both nuclear compliance and cell compliance increase with chromatin decondensation, indicating that nuclear mechanics influence overall cell mechanics in ES cells.

We propose that chromatin condensation plays a crucial role in the regulation of pluripotency and that chromatin has to be decondensed before lineage commitment and heterochromatinization can occur. The connection between chromatin state and cell mechanics has far reaching

implications for the regulation of early embryonic fate decisions and cell sorting processes. In addition to well-known biochemical and positional cues, biophysical properties could act as a regulatory mechanism in early embryonic development.

Zusammenfassung

Pluripotenz spielt eine Schlüsselrolle in embryonalen Stammzellen (ES Zellen) sowie im Epiblasten, dem Ursprungsgewebe des Embryos. Die Charakterisierung dieses speziellen Zustands der Pluripotenz und der zugrunde liegenden molekularen Mechanismen hat die Wissenschaft seit Jahrzehnten inspiriert. In dieser Studie haben wir eine Mischung aus bewährten und neuen Methoden verwendet um biophysikalische Veränderungen zu untersuchen, die in Stammzellen, die auf transkriptioneller Ebene heterogen sind, schon vor der Differenzierung passieren.

Nanog ist ein Transkriptionsfaktor, der Pluripotenz stabilisiert und dessen Expressionslevel zwei unterschiedliche Zustände innerhalb der Pluripotenz definieren: Zellen mit hohem Nanog Expressionslevel sind stabil pluripotent während Zellen mit niedrigen Levels zur Differenzierung tendieren. Wir haben mittels optischer Zelldehnung herausgefunden, dass letztere Zellen leichter verformbar sind als stabil pluripotente Zellen. Das Zytoskelett spielt eine prominente Rolle für die mechanischen Eigenschaften einer Zelle; deswegen haben wir die Struktur von Zytoskelettfilamenten in ES Zellen untersucht. In immunohistochemischen Analysen von adherenten sowie abgelösten Zellen fanden wir jedoch keine Unterschiede zwischen den beiden Zuständen. Zusätzlich konnten wir ausschließen, dass Veränderungen in der Proliferationsgeschwindigkeit oder in den relativen Volumenverhältnissen zwischen Kern und Zytoplasma für die mechanischen Unterschiede verantwortlich waren.

Der Einfluss des Zellkerns auf die mechanischen Eigenschaften der gesamten Zelle sind nicht sehr gut untersucht, allerdings sind Kerne in ES Zellen vergleichsweise groß und daher zogen wir in Betracht, dass Kerne die Zellverformbarkeit mitbestimmen könnten. Um die mechanischen Eigenschaften von Kernen zu messen, haben wir eine neue Methode entwickelt, bei der Kerne in intakten Zellen verformt werden können. Mit dieser Methode fanden wir Unterschiede in der Kernverformung wie wir sie für die unterschiedlichen Zellpopulationen gesehen haben. Um die Substruktur des Kerns zu untersuchen, haben wir Histon-Mobilität eines markierten Histons mit einer Photobleaching Technik untersucht und zusätzlich die Verteilung des Heterochromatin-spezifischen Proteins HP1α analysiert. Die Ergebnisse beider Analysen stimmten darin überein, dass Chromatin im stabil pluripotenten Zustant, in dem Zellen und Kerne steifer waren, stärker kondensiert ist. Mit verschiedenen Chemikalien beeinflussten wir spezifisch die Chromatin-Kondensierung und

konnten zeigen, dass sowohl Zell- als auch Kern-Verformbarkeit mit Dekondensierung steigen, ein Hinweis darauf, dass die Kernmechanik die Zellmechanik insgesamt beeinflusst.

Wir postulieren daher, dass Chromatin-Kondensation eine zentrale Rolle für die Regulation der Pluripotenz spielt und dass Chromatin erst dekondensiert werden muss bevor Zellen einer Entwicklunslinie folgen können und die Formation von Heterochromatin stattfinden kann. Die Verbindung zwischen den Eigenschaften des Chromatins mit der Zellmechanik hat weitreichende Konsequenzen für die Regulation von frühen embryonalen Entscheidungen und Sortierungsprozessen von Zellen. Zusätzlich zu bekannten biochemischen und positionsabhängigen Signalen könnten biophysikalische Eigenschaften regulatorische Mechanismen in der frühen Embryonalentwicklung darstellen.

Contents

1. Introduction

For my diploma thesis, I was working on an interdisciplinary project in the field of biophysics. Therefore, a number of different subjects will be introduced – at least on a basic level – in the following chapter. First, I will describe the relevant biological background in the field of stem cell research and pluripotency. Second, I will present basic concepts of cell and nuclear mechanics and their importance in development. Finally, I will discuss how mechanical properties of biological materials can be investigated.

1.1. Embryonic Stem Cells and Pluripotency

Embryonic stem (ES) cells are pluripotent cell lines that can give rise to all somatic cell lines in the developing embryo (reviewed in [Nichols and Smith 2011; Silva and Smith 2008]). Routinely, mouse embryonic stem (mES) cells are derived at the blastocyst stage of the pre-implantation embryo (fig. 1.1 B). Mammalian embryonic development is best studied in mice, which is a good model system also for human development and therefore I will focus on the description of the properties of mES cells. Before recapitulating the current knowledge on mES cells and the pluripotent state, I will give a short introduction on early embryonic development to allow the integration of the findings of our study into a broader *in vivo* background.

1.1.1. Early Embryonic development

Embryonic development starts with the fertilization of the ovum (egg cell) upon which several cycles of mitotic cell divisions divide the egg without increasing the volume of the embryo. This process is called cleavage and takes place within the intact zona pellucida, a layer of extracellular glycoprotein that surrounds the mammalian egg [Gilbert 2010]. Initially, the blastomeres (individual cells formed by cleavage) are loosely connected and and can be easily distinguished. Then, at the 8-cell stage, the phenomenon of compaction occurs: The cells start to express cell adhesion molecules such as E-cadherin and form a compact cell-ball, which leads to the formation of the morula at the 16-cell stage [Gilbert 2010]. At this stage, the first fate decision takes place: cells that are in the inside of the morula will form the inner cell mass and cells on the outside

mostly give rise to trophectoderm (TE, also trophoblast, fig. 1.1 B, C), which will give rise to extraembryonic tissue, precisely the embryonic portion of the placenta [Gilbert 2010; Zernicka-Goetz et al. 2009]. By the 64-cell stage, the ICM and TE (fig. 1.1 B and C) form two distinct cell layers and individual cells do not contribute to the other cell layer anymore [Gilbert 2010]. At this early blastocyst stage, the blastocyst cavity (blastocoel) forms (fig. 1.1 B). Cells of the ICM will consequently give rise to both embryonic and extraembryonic tissue: The second fate decision separates the epiblast (EPI) and the primitive endoderm (PE) (fig. 1.1 B, C). Epiblast cells from the late blastocyst are also a source for ES cell derivation. The late blastocyst finally hatches from the zona pellucida and attaches to and implants into the uterus. After the implantation and the formation of more extraembryonic structures, embryonic development continues with the formation of the three germ layers by gastrulation [Gilbert 2010].

1.1.2. Regulation of Pluripotency

ES cells are defined by three specific properties: unlimited self-renewal, chimera formation and pluripotency [Silva and Smith 2008]. The first describes the potential to propagate indefinitely in culture, a feature that most primary cell lines do not have due to cell senescence [Alberts et al. 2002]. The second property describes the ability to form adult tissue if ES cells are injected into a blastocyst and the embryo is implanted into a foster mother. The third property is particularly important: pluripotent ES cells have the ability to differentiate into any somatic cell type in the adult [Nichols and Smith 2011]. In embryonic development, pluripotency is established in the ICM of the blastocyst; before that cells are totipotent and can also give rise to the extraembryonic TE [Gilbert 2010]. Apart from the ICM, cell lines with similar pluripotency characteristics have been derived from primordial germ cells (precursors of germ cells and gametes in the embryo) and by somatic reprogramming [Matsui et al. 1992; Takahashi and Yamanaka 2006]. The latter cells are called induced pluripotent stem (iPS) cells and the induction of pluripotency in somatic cells can be achieved by the introduction and expression of the regulatory transcription factors (TFs) Oct3/4, Sox2, c-Myc and Klf4 [Takahashi and Yamanaka 2006].

Many questions about pluripotency are still open; however, intense research in the last decades has revealed some of the key features of pluripotency: transcriptional regulation is comparably well studied and the TFs Sox2, Oct4 and Nanog were shown to form the main regulatory transcriptional network (SON-network) for the maintenance of pluripotency (reviewed in [Silva and Smith 2008]). Sox2, an SRY-related HMG box-family TF, cooperates with Oct4 to promote Oct4-target gene expression (e. g. *Nanog* [Kuroda et al. 2005]). *Sox2* $^{-/-}$ embryos die immediately after implantation [Avilion et al. 2003] and *Sox2*-knock-down in ES cells leads to differentiation into

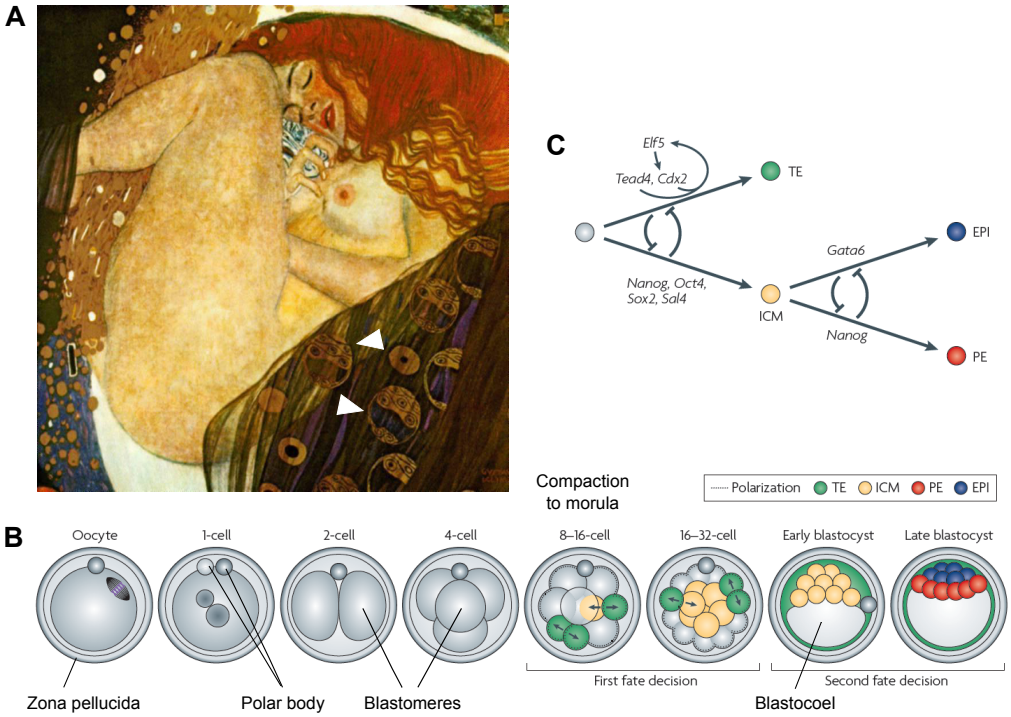

Figure 1.1. – Early embryonic development in the centuries. While (A) shows the painting 'Danae' from 1907/08 by Gustav Klimt in which blastocysts were displayed to a public audience for the first time, (B) and (C) summarize the current view of pre-implantation embryogenesis. (A) Klimt was inspired both by greek mythology and science: The legend has it that Danae conceived Perseus from the god Zeus who came to her in the form of a gold shower. In the lower right part, blastocysts are depicted (white arrowheads). Klimt had heard from blastocysts from a doctor and scientist friend. Image modified from http://www.ibiblio.org/wm/paint/auth/klimt/klimt.danae.jpg (B) Schematic of the pre-implantation development of a mammalian embryo. Polar bodies form as a result of the asymmetrical meiotic cell divisions of the oocyte. Before compaction of the morula, the blastomeres are visible as distinct cells. The first two fate decision (trophectoderm (green) vs. inner cell mass (yellow) and primitive endoderm (red) vs. epiblast (blue)) are indicated. By the late blastocyst stage, the blastocoel (fluid filled cavity) and the three cell types TE, PE and EPI form distinct layers. At this developmental stage, embryonic stem cells can be derived from the epiblast cells of the blastocyst. (C) Schematic of the first two fate decisions in the embryo with the relevant transcription factors indicated. (B) and (C) modified from [Zernicka-Goetz et al. 2009].

multiple lineages [Ivanova et al. 2006], indicating the functional relevance of Sox2 in ES cells and in the embryo.

Oct4 (also Oct3/4) is a POU family transcription factor expressed from the *Pou5f1* gene and is a central regulator of pluripotency [Nichols et al. 1998]. However, its expression is not limited to pluripotent cells (reviewed in [Niwa 2007]). Oct4 acts in a dose-dependent manner and its repression leads to differentiation to the TE lineage while its overexpression leads to PE differentiation [Niwa et al. 2000].

Nanog is a homeodomain-containing TF and has raised special interest in recent years due to some unique properties. Nanog was discoverd as one of the central factors in self-renewal [Chambers et al. 2003], however, conditional deletion studies showed that Nanog is not necessary for maintaining pluripotency [Chambers et al. 2007]. Nanog is required for the establishment of pluripotency in embryogenesis and also for the development of germ line cells [Chambers et al. 2007; Silva et al. 2009]. Although it is not part of the canonical combination of reprograming factors for the induction of pluripotency [Takahashi and Yamanaka 2006], it has been shown that endogenous Nanog expression is necessary to induce pluripotency. The initial dedifferentiation does not require Nanog, but the final transition to pluripotency requires Nanog and does not happen in *Nanog*$^{-/-}$ cells [Silva et al. 2009]. Although Nanog function is still not entirely clear, it was concluded that it is required for the final steps of establishing pluripotency but not for its maintenance [Theunissen and Silva 2011].

In line with these properties are findings about the fluctuation of Nanog expression in regular ES cell culture: While most cells express Nanog at high levels (HN), about 25 % of cells down-regulate Nanog to undetectable levels (low Nanog, LN) while still staying pluripotent [Chambers et al. 2007; Kalmar et al. 2009]. This equilibrium is dynamic and cells with down-regulated Nanog can switch back to high expression levels. The two cell populations show similar transcription patterns, however, the LN cells represent a state that is more prone to differentiate: Oct4 expression is slightly down-regulated and differentiation specific proteins such as Fgf5 [Kalmar et al. 2009] and Gata6 [Singh et al. 2007] are upregulated. Since Gata6 is a marker for primitive endoderm formation, it was proposed that the fluctuating Nanog expression reflects the heterogeneity that has also been observed in the ICM cells of the early blastocyst stage [Chazaud et al. 2006; Singh et al. 2007]. Nanog overexpression, however, stabilizes pluripotency and seems to restrict global differentiation options [Chambers et al. 2007].

Taken together, the SON-network plays a crucial role in regulating pluripotency. Nanog is special in a way that it is necessary for the establishment of pluripotency and its stabilization, but not needed for its maintenance. However, the exact molecular mechanisms of how pluripotency is established are still not well understood. In the next section I will discuss chromatin structure

and epigenetic regulatory mechanisms and finally how the SON-network is involved in epigenetic control of pluripotency.

1.1.3. Epigenetic Mechanisms in Differentiation and Development

Chromatin Condensation and Epigenetics

In eukaryotic cells, structural proteins associate to DNA to pack it into chromatin. To form the most basic level of DNA compaction, the nucleosome, a 147 bp segment of DNA, is wrapped around a core histone octamer consisting of two histone H2A-H2B-dimers and two H3-H4-dimers. Linker histones such as histone H1 and non-histone chromatin proteins can associate to the nucleosomes and accomplish higher order packaging [Alberts et al. 2002]. Reversible covalent modifications of DNA or the histone proteins (fig. 1.2 A) lead to changes in chromatin compaction and thereby allow a form of transcriptional control called epigenetic control. DNA sequences that are compacted into the highly condensed heterochromatin are generally not transcribed and genes in these chromatin regions are therefore repressed, or 'silenced'. Typically, large regions of heterochromatin occur at centromeres, telomeres and stretches of highly repetitive DNA. In contrast, loosely packed euchromatin is accessible to the transcriptional machinery [Alberts et al. 2002]. Chromatin remodeling enzymes are responsible for the creation and removal of epigenetic modifications and besides DNA methylation there is a variety of possible histone modifications (methylation, phosphorylation, acetylation and ubiquitylation). Combination of those allows for a great variety of specific signals and control options. Importantly, when cells divide, DNA methylation and histone modifications can be inherited, specifically histone H3 and H4 modifications since these proteins do not dissociate from the DNA during replication [Alberts et al. 2002]. Therefore, epigenetic control can serve as a memory mechanism for gene expression and cell function.

Euchromatin and heterochromatin can be distinguished both microscopically and on a molecular level: Heterochromatin appears dense both in electron microscopy and light microscopy where DNA-specific dyes are enriched at regions of dense packaging. On a molecular level, specific covalent chromatin modifications can be used to distinguish the two chromatin states: Repressive marks include di- and tri-methylation of lysine 9 of histone H3 (H3K9me2/3) or lysine 27 (H3K27me3) and associated proteins such as the HP1-family (heterochromatin protein) [Eissenberg and Elgin 2000; Fisher and Fisher 2011]. Acetylated histone H3K9 (H3K9ac), H3K4me3 and H3K36me3 are associated with transcriptionally active regions [Fisher and Fisher 2011]. Chromatin states can also be investigated in live cells, e. g. by probing the dynamics of fluorescently labelled structural proteins using photo-bleaching techniques (flourescence recovery after photobleaching, FRAP) [Kimura and Cook 2001; Phair et al. 2004]. Higher level organization

of chromatin in nuclei is non-random and is specific for certain stages of differentiation and cell types [Joffe et al. 2010].

Chromatin in ES Cells and Differentiation

ES cells exhibit unique features in their chromatin organization: Global DNA demethylation occurs during early embryonic development leading to a demethylated state in the blastocyst stage [Rougier et al. 1998]. This coincides with reactivation of the inactive X-chromosome in female embryos in the ICM of the blastocyst [Silva et al. 2009].

Additionally, ES cells contain less heterochromatic regions than differentiated cells and several structural proteins were shown to be less tightly bound to DNA [Meshorer et al. 2006; Bhattacharya et al. 2009]. Heterochromatin can be organized in distinct foci that are distinguishable from euchromatic regions, e. g. in immunohistochemistry. In ES cells there are fewer of these foci and they appear more diffuse than in lineage committed neuronal progenitor cells (NPCs) [Meshorer et al. 2006] or in differentiated cells (fig. 1.2 C, D). Globally, chromatin is in a more decondensed, or open, conformation (fig. 1.2 B, reviewed in [Meshorer and Misteli 2006; Fisher and Fisher 2011; Orkin and Hochedlinger 2011]. These structural properties are also reflected functionally: Chromatin in ES cells is more permissive for transcription and global low-level transcription was detected, even in otherwise silent repetitive DNA regions [Efroni et al. 2008]. The globally open conformation seems to be functionally relevant as Chd1, a chromatin remodeler associated with transcriptional activation, was shown to be essential for pluripotency [Gaspar-Maia et al. 2009].

Histone modifications in ES cells show some very specific patterns: Bernstein et al. [2006] first reported the existence of so-called 'bivalent' chromatin domains where short regions of activating histone H3K4me3 are nested in large regions of repressive H3K27me3 marks. Interestingly, many of these bivalent domains were found at developmentally important TF genes and were proposed to be in a state that is poised for rapid activation while still being silenced in the pluripotent state [Bernstein et al. 2006]. In the course of differentiation, most bivalent domains get resolved to either activated (H3K4me3 only) or silenced (H3K27me3 only) state [Mikkelsen et al. 2007]. Significantly, bivalent domains were also found *in vivo* in ICM cells and become less frequent along the course of differentiation as demonstrated for NPCs, mesenchymal stem cells (MSCs) and hematopoietic stem and progenitor cells [Mikkelsen et al. 2007; Mohn et al. 2008; Cui et al. 2009; Collas 2010; Mazzarella et al. 2011].

DNA methylation, specifically at cytosines of CpG sequences in promotor regions, is considered an epigenetic mechanism for stable gene silencing [Cedar and Bergman 2009]. In ES cells, the global level of methylated cytosines in CpG is low and *de novo* methylation of several hundred

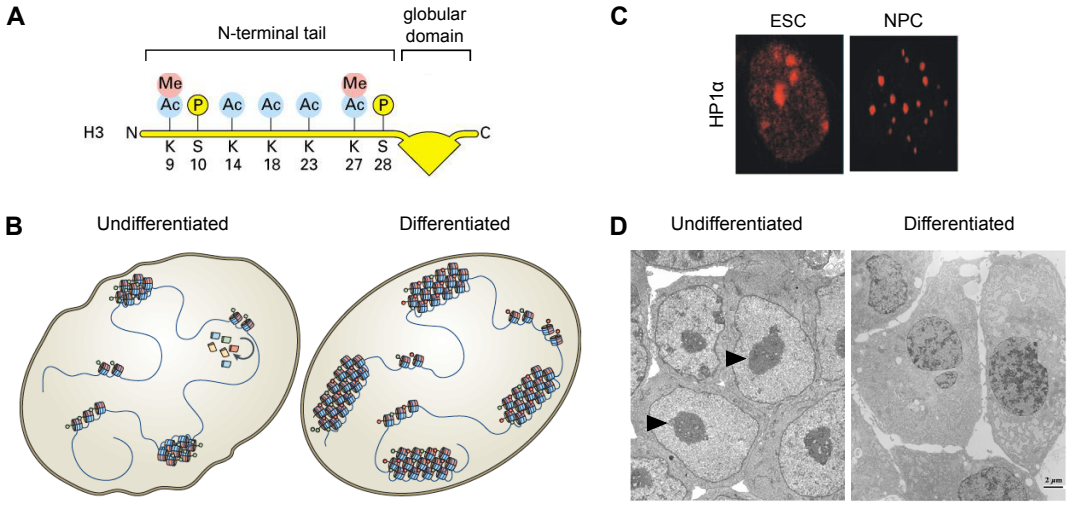

Figure 1.2. – Chromatin structure in ES cells and differentiation. (A) Schematic view of the structure of the core histone H3. The globular domain is part of the histone octamer that forms the core of nucleosomes around which DNA is wrapped. The N-terminal tail domain can be modified covalently at various positions, which determines the interaction properties with DNA and other structural proteins. Abbreviations: Me: methylation, Ac: acetylation, P: phosphorylation, K: lysine, S: serine. (B) Schematic model by Meshorer and Misteli [2006] of how the global chromatin structure changes in the course of differentiation of embryonic stem cells. Chromatin is globally decondensed in undifferentiated cells and chromatin structure changes dynamically. In differentiated cells, large regions of chromatin are compacted into heterochromatic foci and genes in these regions are silenced. (C) Staining patterns of the hetereochromatin marker HP1alpha. While the distribution is more diffuse in nuclei of embryonic stem cells (ESC), many small and distinct foci appear in neuronal progenitor cells (NPC). (B, C) modified from [Meshorer and Misteli 2006]. (D) Electron micrographs of ES cells and differentiated primitive endoderm cells. Chromatin is decondensed and nuclei are bigger in ES cells, where they comprise a large portion of the total cell volume. Nucleoli (arrow heads) appear electron dense. In PE cells, nuclei are smaller and electron dense heterochromatin foci are distributed throughout the nucleus. Image modified from [Niwa 2007].

genes was reported to happen at lineage commitment of NPCs [Mohn et al. 2008]. Active DNA demethylation was reported for both ES cells and in the ICM *in vivo* and was shown to be essential to prevent *Nanog* and transcriptional down-regulation of Nanog [Ito et al. 2010].

Although chromatin is generally considered to be in an open state in ES cells, chromatin decondensation and transcriptional promiscuity are also counterbalanced, e. g. by repressive marks in bivalent domains or repressive chromatin remodeling proteins such as undifferentiated transcription factor 1 (UTF1). UTF1 was associated with gene repression in ES cells and its knock-down resulted in differentiation defects [Kooistra et al. 2010].

The SON-Network in Epigenetic Control of Pluripotency

Chromatin organization in ES cells is unique and therefore it is not surprising that the core transcription factors associated with pluripotency, Sox2, Oct4 and Nanog, are implicated in the complex regulation of chromatin remodeling on multiple levels. The DNA sequences of the three core TFs are targets of the esBAF chromatin remodeling complex, a protein complex that is unique in ES cells (reviewed in [Fisher and Fisher 2011]). On the other hand, numerous protein-protein interactions between the core TFs and chromatin remodeling complexes have been reported [Wang et al. 2006; Mallanna et al. 2010; Pardo et al. 2010]. Specifically, members of the Polycomb group (PcG) and trithorax group (trxG) proteins (e. g. esBAF) that are critically involved in developmental processes are relevant in this context [Fisher and Fisher 2011] and many of these remodeling complexes in turn target the SON-network genes (reviewed in [Orkin and Hochedlinger 2011]).

Nanog seems to play a special role in the regulation of chromatin modifications. Its expression is required twice in embryonic development: First, when the pluripotent epiblast is specified in the blastocyst stage between E3.5 (day 3.5 of embryonic development) and E4.5 in mice. Second, from E7.75 to E11.5 in developing primordial germ cells (PGCs) [Theunissen and Silva 2011]. Interestingly, ICM cells and PGCs share unique epigenetic features: Both reactivate the second X-chromosome in female cells and show global DNA demethylation [Monk and McLaren 1981; Rougier et al. 1998; Reik et al. 2001; Silva et al. 2009; Theunissen and Silva 2011]. The SON-network was functionally implicated in X-reactivation [Navarro et al. 2008] and *Nanog*$^{-/-}$ cells failed to develop to pluripotent epiblast cells and did not reactivate the inactive X-chromosome [Silva et al. 2009].

Summarizing recent findings on epigenetic mechanisms, it becomes apparent that chromatin condensation and modifications are of significant importance for the establishment and maintenance of pluripotency. The global state of chromatin fundamentally differs from differentiated

cells in its open conformation, the presence of two active X-chromosomes and globally demethylated DNA. In the next section, I will focus on the role of mechanical properties of cells, nuclei and substrates and how these parameters can be critically involved in developmental processes.

1.2. Mechanical Properties of Cells and Nuclei

1.2.1. Mechanics in Development

Mechanical properties of cells play a crucial role for many aspects of cell function. I will describe a few examples that will illustrate the importance of physical properties of cells and tissues in the course of development, before giving insight into general concepts of cellular and nuclear mechanics.

The question of how tissues and organs are formed in the embryo (morphogenesis) is one of the central questions of developmental biology. Apart from processes such as cell growth, division and apoptosis, changes in cell shape contribute to morphogenesis [Paluch and Heisenberg 2009]. Cell shape is determined by the interaction of internal properties of cells, i. e. material properties and active properties, and external forces acting on cells, such as the adhesion to neighboring cells and the extracellular matrix (ECM) and its properties. Essentially, all of these factors are integrated via biochemical signaling pathways and result in distinct physical properties of cells and tissues [Paluch and Heisenberg 2009].

The measurement of physical properties of cells in the developing embryo is challenging, and while genetic and biochemical aspects of development were intensely studied in the past, the contribution of physical properties is poorly understood in many processes. However, there are a number of phenomena in which the involvement of mechanical forces are well established. These include e. g. the 'convergent extension' in vertebrate gastrulation, where myosin-dependent cell intercalations lead to the elongation of the anterior-posterior-axis in the embryo [Keller 2002; Skoglund et al. 2008]. Also, actin-myosin dependent cortical tension was reported to play a crucial role in cell sorting processes of germ-layer organization in gastrulation [Krieg et al. 2008]; in this paper, the authors also suggested a role of cortical tension in differential cell adhesion, which had previously been shown to play a role in cell sorting processes [Foty et al. 1996].

Even at earlier stages in development cell sorting and movements were observed: Cells of the ICM in the early blastocyst that express EPI- or PE-markers are initially intermixed and eventually sort out to form two distinct cell layers in the late blastocyst stage. Active actin-dependent cell movements to the correct positions were shown to play a major role in this cell sorting process [Meilhac et al. 2009] and the latest models propose that both positional induction and cell sorting are involved [Zernicka-Goetz et al. 2009].

In addition to these *in vivo* studies, numerous reports have demonstrated interconnections between cell and substrate mechanics and the degree of differentiation *in vitro*. Among these are studies that report stiffening of cells [Pillarisetti et al. 2011] or nuclei [Pajerowski et al. 2007] in the course of differentiation of stem cells. In contrast to that, substrate stiffness was

reported to influence cell behavior: Plating of mesenchymal stem cells on matrices with different elasticities directed cells to differentiate along distinct lineages [Engler et al. 2006]. The authors of this study report that substrate stiffnesses mimicking the *in vivo* environment induce cells to differentiate into according cell types, e. g. soft substrates were neurogenic and rigid substrates osteogenic. Furthermore, a dependence of this behavior on the cytoskeletal motor protein non-muscle myosin-II was reported, indicating that force generation plays a crucial role in this process.

Mechanical properties of cells also reflect cell function and properties: Cell mechanics studies revealed that acute promyelocytic leukemia (APL) cells become more compliant when they differentiate along the neutrophilic lineage [Lautenschläger et al. 2009]. This allows higher mobility for neutrophils which is important for their physiological function. Similarly, pathological changes in cell function were related to changes in cell mechanics: Metastatic oral cancer cells were found to be softer than non-metastatic cells [Remmerbach et al. 2009].

Several key questions are raised by the apparent importance of mechanics in living organisms: What defines mechanical properties of cells and tissues? How can mechanical cues be sensed and integrated with biochemical signals to change cell behavior? Detailed knowledge about specific structures that contribute to cell mechanics is described in many textbooks (e. g. Alberts et al. [2002]), so I will not go into great detail but rather describe the fundamental principles of cell mechanical properties that are most relevant to my work.

1.2.2. The Cytoskeleton

The cytoskeleton is built up by filamentous networks and serves three key functions in eukaryotic cells: Organizing the cell content spatially including intracellular transport, establishing a physical and biochemical connection to the outside of the cell (via adapter proteins), and the generation of forces to accomplish movement and cell shape changes [Fletcher and Mullins 2010]. Microtubules, actin filaments and intermediate filaments contribute to the cytoskeletal network and, although they serve different functions, they have common features. All of these filaments are built up by smaller building blocks that self-assemble dynamically. The individual subunits and filaments can be arranged to form structures that differ significantly in their function and properties. Finally, filaments can disassemble and reassemble to change their architecture [Alberts et al. 2002; Fletcher and Mullins 2010].

The three polymers give rise to a complex network that can resist deformations while keeping the ability to reorganize upon the application of forces from outside. The network architecture and properties are controlled by a great number of regulatory proteins that control processes such as the initiation and termination of filaments, polymerization and depolymerization as well

as cross-linking of filaments to form higher order structures [Alberts et al. 2002; Fletcher and Mullins 2010].

Microtubules

Microtubules (MTs) are built up by tubulin subunits that form protofilaments which assemble into ∼25 nm thick tubular structures and form e. g. the mitotic spindle in dividing cells [Alberts et al. 2002]. MTs are the thickest cytoskeletal filaments and can form radial arrays of relatively straight filaments that are important for intracellular transport in interphase nuclei in combination with molecular motor proteins. Their thickness and tubular structure is reflected functionally in their high stiffness and MTs are proposed to bear compressive forces [Ingber 2003]. MTs are polarized and their assembly is characterized by either stably growing or rapid shrinking, a feature called 'dynamic instability' [Alberts et al. 2002].

Actin Filaments

Actin subunits assemble into two-stranded helical polymers to form the 5-9 nm thick actin filaments. Individual filaments are much less rigid than MTs, however, actin filaments can arrange in very stiff structures, e. g. linear bundles, two-dimensional networks or three-dimensional gels [Alberts et al. 2002]. Individual filaments steadily assemble and disassemble in a 'treadmilling' fashion. Actin plays a crucial role in cell movements and is found in the leading edge of different cell protrusions. Cortical networks form beneath the cell membrane and bear tensile loads in multiple directions [Fletcher and Mullins 2010]. Together with motor proteins (myosins), the polarized actin filaments can form contractile structures (e. g. stress fibers) that allow adherent cells to deform and also to probe their extracellular environment [Fletcher and Mullins 2010]. The ends of stress fibers are bundled in focal adhesions, where they are connected via adapter proteins such as vinculin and talin to integrins which span the plasma membrane [Wiesner et al. 2005]. Integrins bind ECM proteins and thereby establish a physical connection from the cytoskeleton to the ECM.

Intermediate Filaments

A heterogeneous family of proteins provides the building blocks for the unpolarized, rope-like, 10 nm thick intermediate filaments (IFs). They are the least stiff filaments but resist tensile forces and often form as a response to mechanical stresses, which is seen, for instance, in epithelial tissues [Alberts et al. 2002]. IFs can be linked to the neighboring cells or the ECM via protein complexes called desmosomes or hemi-desmosomes [Alberts et al. 2002]. The type-V IFs lamin A/B/C, together with associated proteins, form the nuclear lamina, which critically contributes

to the structural integrity of the nucleus, specifically lamin A and C [Pajerowski et al. 2007; Dahl and Kalinowski 2011]. Various chromatin-binding and regulatory proteins also bind to lamins and indirect regulatory functions of lamins on gene expression were proposed [Dorner et al. 2007].

1.2.3. Nuclear Mechanics

The structure of the eukaryotic nucleus can basically be divided into two main components: the nuclear envelope and the nuclear interior. The envelope consists of the inner and outer nuclear membrane (INM and ONM), nuclear pore complexes that connect the interior to the cytoplasm and the nuclear lamina [Dahl et al. 2008]. The outer nuclear membrane is continuous with the endoplasmatic reticulum. The nuclear interior, the nucleoplasm, is occupied by chromatin and some nuclear substructures, such as nucleoli, Cajal bodies and promyelocytic leukemia bodies [Dahl et al. 2008]. The role of the interior in nuclear mechanics is subject of debate, however, several structural proteins have been reported to reside in the nuclear interior: nucleoplasmic lamins A/C [Broers et al. 2005], actin [Pederson and Aebi 2005], myosin [Hofmann et al. 2006] and other proteins [Young and Kothary 2005]. The structural proteins of the nucleus as a whole form the nucleoskeleton [Dahl and Kalinowski 2011].

The eukaryotic nucleus has been shown to be the stiffest organelle of cells, being 3–10 times stiffer than the cytoplasm [Guilak et al. 2000; Caille et al. 2002]. Both the nuclear lamina and the interior contribute to these mechanical properties of the nucleus in different ways. The lamin proteins and in particular lamins A and C were shown to be major determinants of the mechanical properties of the envelope and the nucleus as a whole [Dahl et al. 2005; Lammerding et al. 2006; Pajerowski et al. 2007]. This is in line with findings that nuclei are mechanically weak in certain laminopathies where the encoding genes are mutated (reviewed in [Worman and Bonne 2007]). The nuclear lamina was shown to stretch more elastically as compared to nuclear interior, which seems to be more viscous and deforms permanently (plastically) in response to applied forces [Pajerowski et al. 2007].

In this context, it is interesting that ES cells lack expression of lamin A/C [Constantinescu et al. 2006]. It has been demonstrated that the nuclei of ES cells are considerably softer than nuclei of differentiated cells and that nuclei of lamin A/C knock-down cells resemble ES cell nuclei in their mechanical properties [Pajerowski et al. 2007]. Chromatin was proposed to contribute to mechanical properties of the nucleus and the relative importance is enhanced in nuclei that lack lamin A/C [Dahl et al. 2005; Pajerowski et al. 2007]. Highly condensed heterochromatin has different mechanical properties than euchromatin and condensation of chromatin was shown to stiffen nuclei [Dahl et al. 2005; Mazumder and Shivashankar 2007, 2010]

Mechanical Connections form the ECM to Chromatin

The nucleus is not an isolated organelle in eukaryotic cells but is connected to cytoplasmatic structures (fig 1.3). At the inner side of the nuclear envelope, adapter proteins like the lamin B receptor (LBR) or emerin connect chromatin, the nuclear lamina, the INM and INM transmembrane proteins [Ye and Worman 1996; Schirmer and Foisner 2007]. INM proteins include SUN1 and SUN2 (Sad1-UNC homology domain) which span the INM and interact with nesprin-proteins in the perinuclear space between the INM and ONM [Schirmer and Foisner 2007]. Nesprin proteins in turn span the ONM and can interact directly with actin filaments or indirectly with IFs via plectins [Crisp et al. 2006]. The protein complex formed by nesprins and SUN-proteins that connects the nucleoskeleton with the cytoskeleton was termed the LINC (linker of the nucleus and cytoskeleton) complex (fig. 1.3) [Crisp et al. 2006]. MTs have also been proposed to directly and indirectly interact with the nucleus [Dahl et al. 2008]. As described above, the cytoskeleton is connected to the outside of the cell via transmembrane proteins, thereby establishing a physical connection that reaches from outside of the cell to the chromatin. Several studies demonstrated that externally applied forces are actually transmitted to the nucleus [Guilak 1995; Maniotis et al. 1997; Guilak et al. 2000].

Integration of Mechanical Signals

The existence of a direct mechanical connection from outside the cell to chromatin raises the question if and how the mechanical environment affects nuclear substructure or even gene expression. Mechanotransduction is defined as the molecular mechanisms that translate mechanical stimuli or cues into biochemical signals [Dahl et al. 2008]. It has long been known that mechanical stress can activate biochemical signaling pathways [Xu et al. 1998], which is not surprising given that actin alone has more than 150 binding partners of which many are involved in signaling cascades [dos Remedios et al. 2003]. The balance between filamentous and globular actin itself was shown to affect certain signaling pathways [Posern and Treisman 2006; Medjkane et al. 2009]. Findings that nuclei change shape and adapt in response to mechanical stress [Deguchi et al. 2005] and that mechanical signals can affect chromatin assembly [Wang et al. 2009] indicate that mechanical signals might influence gene expression in a more direct way than via biochemical signals. There is no direct evidence that mechanical cues directly, via physical connections, affect the expression of a gene, however, several recent reviews propose possible mechanisms [Dahl et al. 2008; Wang et al. 2009; Shivashankar 2011] (fig. 1.3).

Since the properties and composition of any of the parts of the physical link from the outside of the cell to chromatin – cell membrane receptors, cytoskeleton and the nuclear envelope – can

undergo significant changes in the course of development, cells potentially react differentially to mechanical cues. In addition to that, biophysical properties of chromatin could influence the susceptibility to external signals [Shivashankar 2011]. This motivated us to investigate if biophysical properties of cells or nuclei would change in the transition from stable pluripotency to a differentiation-prone state in ES cells.

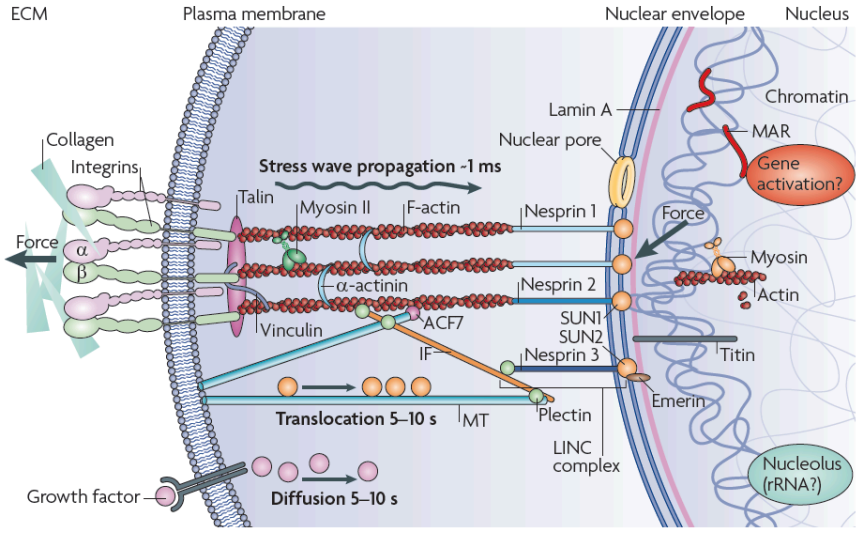

Figure 1.3. – Physical connections link chromatin to the outside of a cell. A model by Wang et al. [2009] of how external forces can be transmitted to the inside of cells: actin filaments in stress fibers (with myosin-II) are connected to the ECM (collagens) at focal adhesions via integrins. Several adapter and linker proteins (talin, vinculin) connect the actin cytoskeleton to integrins. Other proteins establish interactions to and between the intermediate filament and microtubule network. The LINC (linker of the nucleus and cytoskeleton) connects the cytoskeleton to the nuclear interior: Nesprins are attached to the cytoskeleton directly or via adapters and span the outer nuclear membrane, SUN proteins interact with nesprins in the perinuclear space and span the INM. In the inside of the nucleus, adapter proteins like emerin connect SUN proteins with the nuclear lamina and chromatin, possibly at special matrix attachment regions (MAR). Nuclear actin, myosin and titin might help forming a nuclear scaffold. Forces could be transmitted fast in comparison to diffusing signals. Figure reproduced from Wang et al. [2009].

1.3. Rheology of Biological Materials

As described above, mechanical properties of cells and substrates play a crucial role for many cell functions and can vary from cell type to cell type and in the course of differentiation and disease. In this section I will point out basic concepts of mechanical measurements of cells and nuclei and provide an overview over the techniques that are used in the field.

Rheology is the technique that measures how materials deform or flow in response to applied mechanical forces [Gardel et al. 2008]. The response of material properties to forces can be described as elastic or viscous or a combination thereof. Elastic properties of solids like a rubber band or a spring can be described using the elastic modulus which is defined as the proportionality between stress (force per unit area, σ) and strain (deformation per unit length, γ). [Gardel et al. 2008]. Different measurement geometries allow the characterization of elastic moduli for tensile, compressive, bending or shear stresses. This is relevant for the interpretation of results from different measurement techniques. In an elastic solid, steady shear stress would result in a constant strain. For a simple fluid like water, however, shear stress results in a constant flow, i. e. a constant rate of strain change [Gardel et al. 2008]. To describe this, the viscosity η, defined as the proportionality between stress and strain rate can be used. Viscous materials can be modeled as dashpots. Cells and cytoskeletal or chromatin polymer networks display features of both elastic solids and viscous fluids, therefore they are visocelastic [Gardel et al. 2008; Verstraeten and Lammerding 2008].

1.3.1. Tools to Study Cell Mechanics

A number of different tools have been developed in the last decades that allow the measurement of rheological properties of living cells. I will give an overview over the most important ones and point out their potential strengths and weaknesses (reviewed in [Guck et al. 2010], [Verstraeten and Lammerding 2008] and [Lammerding et al. 2007]). Generally, one can distinguish techniques that are used to probe global rheological properties of cells in the attached or suspended state versus techniques to investigate local properties of smaller parts of cells.

To measure global rheological properties of cells like their overall stiffness (or the inverse, compliance), several techniques have been established: Micropipette aspiration was one of the first techniques that have been used and it is still used nowadays [Leblond et al. 1971; Hochmuth 2000]. Parts of cells are pulled into a micropipette with a diameter smaller than the cells' with a given pressure. Speed and length of the protrusion into the micropipette can be used to infer mechanical properties (fig. 1.4 (Aa)).

In microplate manipulation, cells are attached to two glass-microplates in a sandwich-like configuration (fig. 1.4 (Ac)). These can be moved together or apart to measure active or passive cell responses [Thoumine and Ott 1997; Caille et al. 2002].

A method which allows relatively quick measurements of suspended cells is microfluidic deformation where cells are forced through narrow channels [Brody et al. 1995; Gabriele et al. 2009] (fig. 1.4 (Ab)). The deformation properties of cells can then be used to infer mechanical properties.

Another tool, which I use in my study, is the optical cell stretcher (OS) [Guck et al. 2001]. Two counter-propagating, non-focussed laser beams are used to trap and deform cells in a contact-free fashion (fig. 1.4 (Ad)). The principle of optical trapping is that dielectric particles are pushed away from a laser source and pulled into the region of highest light intensity and was first described by Ashkin [1970]. Cells have a higher refractive index than the surrounding culture medium and therefore are dielectric objects which results in the transfer of momentum to the cell membrane in a laser beam [Guck et al. 2001]. In optical stretching, cells are pushed away from the sources of two counter-propagating gaussian laser beams and and pulled towards the center of the laser axis, which is the same for both lasers and where the light intensity is highest. As a result, cells can be stably trapped in the center between the two laser sources and forces normal to the surface and away from the cell center act on the cell surface (fig. 1.4 (Ad)) [Guck et al. 2001]. Whole cell deformation measurements can then be performed by trapping cells and applying a step-stress by increasing the power of the lasers. Viscoelastic properties of the cells can be calculated from the response of the cells to the applied stress [Ananthakrishnan et al. 2006]. Figure 1.4 (B) shows how elastic and viscous responses or a combination thereof would look like when a step stress is applied to a material.

In combination with a microfluidic system, a relatively high throughput of around 100 cells/h can be reached and cells that grow in suspension can be probed in their physiological environment. Adherent cell types have to be detached and suspended first.

To measure mechanical properties of specific parts of cells at high spatial resolution, microrheology and atomic force microscopy (AFM) are most widely used (fig. 1.4 (C)). In microrheology, movements of intracellular particles are analysed, either endogenous organelles or externally delivered particles, to calculate rheological properties of the cell (reviewed in [Cicuta and Donald 2007]). There are several different variants of this technique, including active microrheology where – in contrast to passive microrheology – active forces using optical tweezers or magnetic beads are applied to the particles. Particles that are attached on the outside of cells can also be used to do similar measurements at the cell surface (magnetic twisting cytometry). Microrheology provides high resolution and gives the possibility of a complete characterization of the viscoelastic

properties of a material [Verstraeten and Lammerding 2008]. However, particle delivery into cells and the dependence of the measurement on intracellular substructure are limiting factors for microrheology [Verstraeten and Lammerding 2008].

In AFM experiments, the tip of a cantilever is used to indent cells (fig. 1.4 (Cb)). Quantification of the deflection of the cantilever can be used to calculate mechanical properties of cells. While the cantilever tip allows high spatial resolution, modifications of the cantilever like the attachment of spherical beads or the use of tipless cantilevers modify the indented area [Guck et al. 2010; Verstraeten and Lammerding 2008]. AFM is most useful to study the effect of compressive forces. A less common high resolution technique is acoustic microscopy where sound waves are used for contact-free mechanical measurements [Hildebrand and Rugar 1984].

1.3.2. Tools to Study Nuclear Mechanics

To study nuclear mechanics, similar tools as for cell rheology can be used [Verstraeten and Lammerding 2008]. However, modifications in the technical details and the theoretical models used in data analysis have to be made. Generally, one has to distinguish between methods that probe the nucleus in its physiological environment inside the cell and methods that require the extraction of nuclei. Micropipette aspiration has been demonstrated on both extracted nuclei [Dahl et al. 2005; Deguchi et al. 2005] and nuclei inside living cells after cytoskeletal disruption [Pajerowski et al. 2007]. Similarly, AFM measurements were performed on extracted nuclei [Dahl et al. 2005] but may also be used on nuclei that can be close to the plasma membrane in adherent cells [Verstraeten and Lammerding 2008]. Particle tracking microrheology can be performed in nuclei inside cells with only minor disturbances of cellular structures [Verstraeten and Lammerding 2008; Tseng et al. 2004]. Cellular strain experiments where substrate strain is applied and deformations of the cell and the nucleus are monitored can also be used to probe nuclear mechanics [Caille et al. 1998].

For the investigation of isolated nuclei, they have to be extracted from intact cells. This can be achieved by detergent treatment or osmotic swelling of nuclei in combination with mechanical disruption of the cell [Dahl et al. 2005; Lammerding et al. 2007]. Isolated nuclei are extremely sensitive to buffer conditions and particularly divalent cations were shown to condense and stiffen nuclei while they swell in the absence of divalent cations [Dahl et al. 2005]. Mimicking the conditions of the cellular interior is therefore a major challenge. The drawbacks of methods that leave the nuclei inside cells is that nuclei are highly connected to the cytoskeleton and results can only be interpreted with this background [Verstraeten and Lammerding 2008].

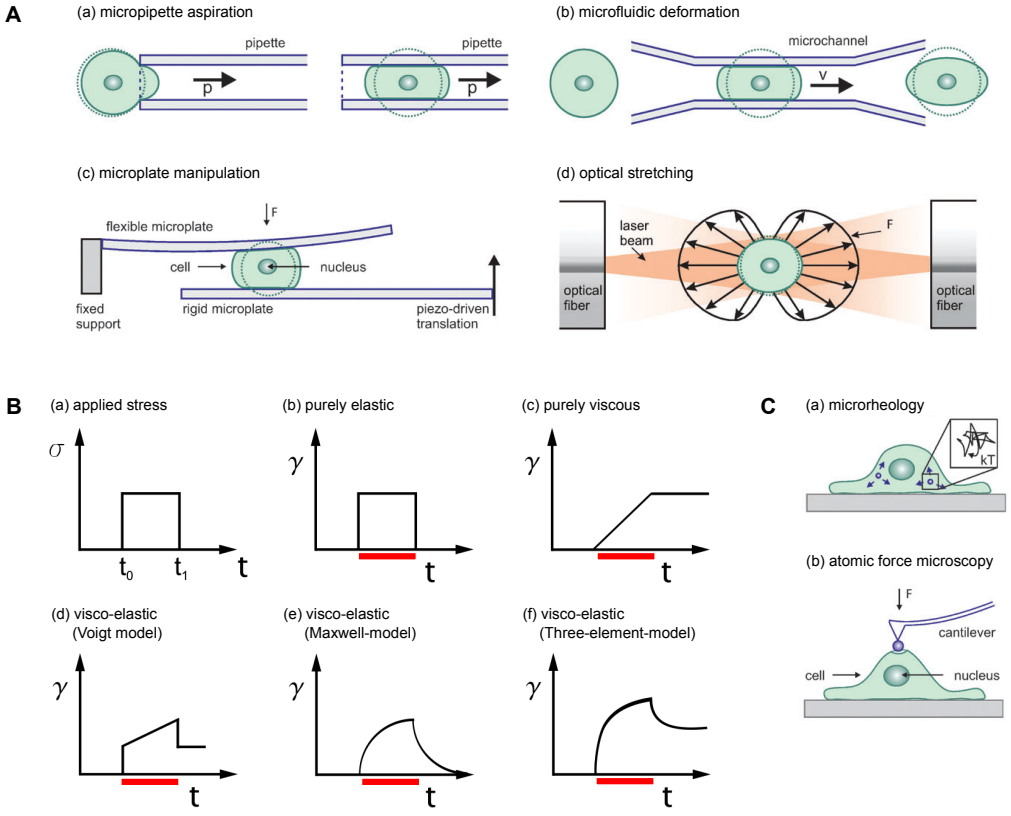

Figure 1.4. – Tools to study cell mechanics. (A) Schematics of methods to measure global mechanical properties. Cells can be pulled into micropipettes (a) or through channels (b) to measure cell mechanics. In microplate manipulation, cells can be compressed or stretched (c). In optical stretching (OS), two laser beams exert forces on the cell membrane to trap and stretch cells (d). (B) Possible response patterns to a step-stress in OS. (a) Shape of the applied stress σ which is indicated in (b–f) by red bars. The relative deformations (strain γ) for different material properties are shown in (b–f). (b) and (c): purely elastic (like a spring) or viscous (dashpot) responses, respectively. Combinations of viscous and elastic properties lead to the response curves shown in (d–f) [Lautenschläger 2011]. (d) Response of viscous (dashpot) and elastic (spring) materials that are connected in series. (e) Properties of a spring and dashpot in parallel. (f) Spring and dashpot in parallel connected to another dashpot in series. (C) The main methods used to probe cell mechanics at high resolutions. The displacement of particles inside cells is monitored in microrheology (a). A cantilever tip is used to indent cells in atomic force microscopy (b). (A) and (C) modified from [Guck et al. 2010], (B) modified from [Lautenschläger 2011].

1.4. Motivation and Aims

Biophysical properties of cells and tissues undergo dramatic changes in the course of development. Therefore, a better understanding of the role of physical properties in embryogenesis is needed to fully understand developmental processes.

Biophysical changes are, on the one hand, a result of signals acting on cells, but on the other hand, differential biophysical properties can act as regulatory mechanisms in fate decisions, cell sorting processes and morphogenesis. Substantial phenotypical transitions like modifications in the global chromatin state or in cell mechanics are well-established between various stages of differentiation, particularly where two clearly distinct stages were compared.

In this study, we took advantage of a cell line that allowed us to discriminate between two pluripotent states: a stable pluripotent state and a differentiation-prone state. The stable state is characterized by high Nanog expression while Nanog is down-regulated in the latter state, thereby rendering these cells susceptible to differentiation cues. A reporter system made it possible to study biophysical changes even before the onset of differentiation. Based on preliminary studies and results that we got in the course of this study, we focussed on changes in cellular and nuclear mechanics as well as chromatin condensation. Establishing a biophysical heterogeneity – along with transcriptional heterogeneity – could give insight into how physical cues are involved in the regulation of pluripotency and early fate decisions.

In addition to a better understanding of development, our study is also interesting from a biomedical point of view: ES cells offer great promise in regenerative medicine and a deeper understanding of their biology can help in the development of new therapeutic applications.

2. Materials and Methods

2.1. Embryonic Stem Cell Culture

The TNGA mouse embryonic stem (mES) cell line we used was a kind gift from the lab of Austin Smith and were described previously [Chambers et al. 2007]. Briefly, an *eGFP* reporter gene was inserted at the AUG codon of one of the *Nanog*-alleles and eGFP expression is therefore correlated with Nanog expression [Chambers et al. 2007]. All cells used for the experiments in this study had passage numbers ranging from 44 to 54. ES cells were cultured in GMEM-medium (Sigma-Aldrich, G5154) supplemented with 10 % fetal bovine serum (FBS, Biosera cat.# S1900-500, lot.# S0495251900), 2 mM GlutaMAX (35050), Penicillin-Streptomycin (100 U/ml and 100 $\mu g/ml$, respectively, 15140-148), 1xMEM nonessential aminoacids (11140035), 100 µM 2-mercaptoethanol (31350010, all from Invitrogen), 1 mM sodium pyruvate (Sigma-Aldrich S8636-100ML) and 1000 U/ml LIF (ESGRO, Millipore ESG1107). The described medium will be referred to as 'LIF+ medium', the same medium without LIF is referred to as 'LIF- medium'.

Routinely, ESCs were passaged every two days and half of the medium was exchanged after one day. For passaging, the medium was removed and the cells were washed with PBS (Source Bioscience PBS0002052 or Biochrom AG L1825), trypsinized with 1 ml trypsin (0.5 g/l, with 0.2 g/l EDTA, Invitrogen 25300-054) for approximately 1 min until cells started detaching. After tapping the culture flask gently with forceps or a pen to detach the cells, the trypsin was neutralized by the addition of LIF- medium (6 ml for a 25 cm^2-flask (T25)). Cells were consequently centrifuged for 5 min at 1000 rpm and resuspended in 1 ml LIF+ medium. For reseeding, culture flasks were gelatinzed for 10 min with a 0.1 % gelatin solution in PBS (gelatin from porcine skin, type A, Sigma-Aldrich G1890). Cells were reseeded in a 1:6–1:10 ratio depending on the density of the harvested culture flask, resulting in a density of approximately 3E4 cells/cm^2. For a T25 flask 5 ml of LIF+ medium were used and the volume was scaled to the growth area of the cells when other dishes or flasks were used. When cell density was crucial or cells were seeded in round dishes, the concentration of the resuspended cells was determined using an Improved Neubauer counting chamber. Cells were cultured in flasks (with filter caps), dishes or multiwell plates of

the Greiner Bio-one Cellstar series unless stated otherwise. All other consumable items were also purchased from Greiner Bio-one unless stated otherwise.

2.2. FACS Analysis and Cell Sorting

2.2.1. Flow Cytometry

To monitor the expression of eGFP and the coupled Nanog expression, the cells were regularly checked using a Dako Cyan ADP FACS analyzer. Cells from a T25 flask or a 6-well plate were trypsinized as described and resuspended in 0.5-1 ml LIF+ medium. A protocol developed by T. Kalmar [Kalmar et al. 2009] was used to analyze the GFP-profile of a cell population. To exclude dead cells or cell doublets, the cells were selected based on their forward scatter (FS), side scatter (SS) and pulse width properties. Typical plots for FS versus SS and pulse width versus FS with the gates we applied are shown in figure 2.1. The laser intensity at 488 nm was set to 400 mW and the gain was adjusted so that GFP-negative cells had intensity values between 10^0 and 10^1. The calibration was done in initial experiments with the non-GFP expressing parental cell line E14 and the left peak in the histogram presented in figure 2.1 (C) represents the autofluorescence of the ES cell-line [Kalmar et al. 2009]. The GFP-positive cells (high Nanog or 'HN') typically showed signal intensities 100-fold that of GFP-negative cells (low Nanog or 'LN') and could therefore easily be distinguished. Only if the profile showed the typical 2-peaked shape with 20–35 % of the cells being GFP-negative and 50–65 % being GFP-positive the cells were used for experiments.

2.2.2. Cell Sorting

To sort the cells into HN and LN populations, the cells were cultivated to around 80-90 % confluency in T75 or T175 flasks depending on the number of cells needed. The cells were trypsinized and resuspended in 2–3 ml of LIF+ medium at a concentration of 1.5-2E7 cells/ml. The suspension was filtered and the cells were sorted using a Dako MoFlo high-speed cell sorter. To select only viable single cells according to their FSC/SSC/pulse width characteristics, the gates described for FACS analysis were used. Two additional gates for each of the two peaks were set to sort HN from LN cells (gates R3 and R4 as shown in fig. 2.1). Cells with intermediate fluorescence intensity were discarded. The sorted cells were collected in 15 ml tubes that had been prepared with 3 ml of LIF+ medium, centrifuged (5 min, 1000 rpm) and resuspended in LIF+ medium. Sorted cells were directly used in stretching experiments or recultured.

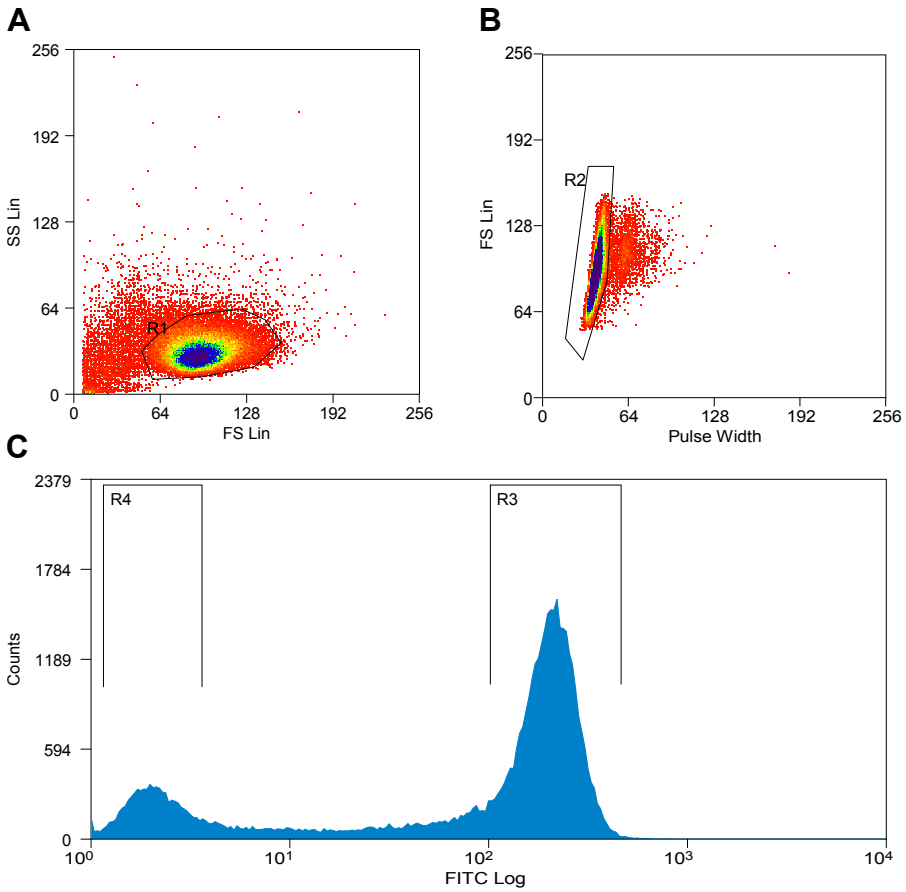

Figure 2.1. – FACS plots from a typical measurement of TNGA cells on a Dako Cyan ADP FACS analyzer. (A) Forward- versus side-scatter plot where the R1 gate was set to exclude apoptotic cells and debris. (B) Pulse width versus forward-scatter plot of the cels gated by R1. The R2 gate was set to exclude cell doublets from analysis and sorting. (C) shows a typical profile of the distribution of green fluorescence intensity (FITC Log, x-axis) in a TNGA cell population. The GFP-negative (LN) peak contained 20–35 % of the cells while the peak with GFP-positive cells contained 50–65 % of the cells. When cells were sorted, the gates R3 and R4 were adjusted to sort a TNGA population into LN and HN cells.

2.3. Optical Stretching Experiments

2.3.1. Optical Stretcher Setup

All optical cell stretching experiments were performed on a custom built OS and the same equipment and settings were used throughout all experiments of this study. The microscope used for imaging phase contrast videos in OS experiments was an inverted Nikon Eclipse TE2000–U equipped with a Nikon Plan Fluor ELWD 40x/0.60 NA objective. A 1.5x C-mount was used to attach either a Hamamatsu ORCA-05G or an AVT Marlin F146B video camera leading to an overall magnification of 60x. Pixel size was typically between 0.0775 and 0.215 µm and video framerates between 20–35 frames per second (fps).

The stage of the microscope was modified so that a microfluidic flow chamber designed for OS experiments could be attached (fig. 2.2). Details on the design of the microfluidic chamber are described by Lautenschläger [2011]. Briefly, a three-dimensional channel structure produced by photolithography was used to align two optical fibers on an axis perpendicular to a glass capillary. The glass capillary, through which the cells were delivered to the optical trap, was connected to microfluidic tubing and the ends of the inlet and outlet tubes were inserted in reservoirs with the growth medium of the cells. Cells from a single cell suspension were inserted into the system with a 1 ml syringe (Terumo) connected to a 4-port-switching valve. By changing the relative position of the inlet and outlet reservoir, hydrostatic pressure was used to control the flow of cells into the capillary.

The laser used in OS experiments was a single mode continuous-wave fiber laser at a wavelength of $\lambda = 1064\,\text{nm}$ (YLM-5-1070-LP, IPG Photonics, UK). Both the laser and the cameras were controlled using a custom-made LabVIEW-software (National Instruments) [Lincoln et al. 2007a,b].

2.3.2. Experimental Procedure

For OS experiments, cells were grown to approximately 80-90 % confluency, trypsinized, optionally sorted as described above and resuspended in LIF+ medium at a concentration of 1-2E6 cells/ml. After an incubation period of 10-20 min at room temperature cells were injected into the microfluidic system and only individual cells with good phase contrast were stretched. We stuck to the incubation period because it has been found that attached cells show a higher compliance immediately after trypsinization [Maloney et al. 2010]. Experiments typically took no more than 2 h from trypsinization or 4 h if the cells were FACS-sorted directly before OS measurements. Repeated experiments did not reveal significant differences between cells stretched directly after trypsinization or after sorting.

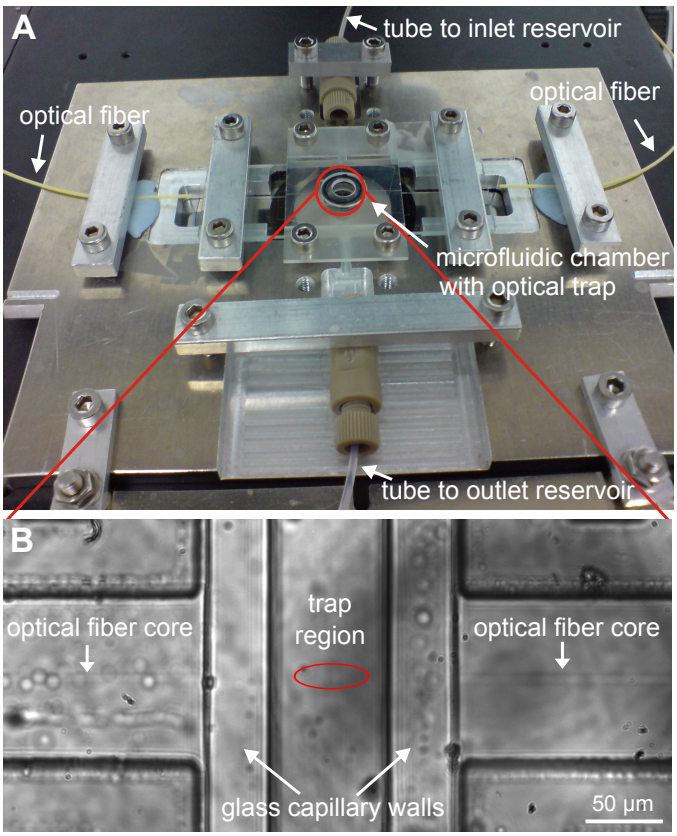

Figure 2.2. – Stage and microfluidic flow chamber of an optical stretcher. (A) Image of the stage of an OS with the microfluidic chamber, optical fibers and tube connections to inlet and outlet reservoirs. Image courtesy of F. Lautenschläger. (B) Phase contrast image of the flow chamber with the optical fibers and the glass capillary. The red ellipse highlights the region where cells are trapped.

In all OS experiments presented in this study, the relative deformation of cells or nuclei in response to the application of a step stress was measured. To start a single measurement a cell was first trapped and allowed to settle somewhere around the middle of the trap so that initial rotations were over. After that, the measurement sequence consisting of three consecutive parts, namely a trapping part, a stretching and a relaxation part was started. The length of the individual parts was 1–3–3 sec and the laser powers applied were 0.2–1.1–0.2 W per fiber, respectively (see fig. 2.3).

2.3.3. Data Processing and Statistical Evaluation

The raw output of an OS measurement is a video of a stretching sequence of a cell. Prior to analysis, all videos were viewed and cells that rotated were excluded from analysis. An exception to this routine was made for cells that showed minor rotations around the laser-axis that did not influence the analysis of the relative deformation along that axis. To quantify the deformation of cells or nuclei, a custom-built edge-detection program (LabVIEW, National Instruments [Lincoln et al. 2007b]) was run for each cell in a first step. Using another LabVIEW program, the data from the edge detection were fitted to ellipses to obtain the relative deformation along the ellipse major axis which is parallel to the laser axis. This gave the stretch curves where relative deformation (strain) is presented, while the peak strain bar diagrams give the value at the end of the stretching period when the highest deformation was observed (see fig. 2.3). The analysis program also allowed to exclude cells that did not follow a visco-elastic response (e. g. contracting cells) or that did not match certain basic quality criteria (stable trapping, no deformation during trapping). The same criteria were applied to all cell measurements.

The data were then imported into Origin 8.5 software (OriginLab), plotted and statistical analysis was performed. The relative deformations for each time-point were averaged over all cells of an experiment and the resulting curves were plotted with standard error of the mean (SEM) as errors. As the shape of the visco-elastic deformation curves was found to be very similar for all cell populations and treatments, we used the time-point with the highest relative deformation at the end of the stretching period for statistical comparison of different conditions. For each experimental day, the null-hypothesis that two populations were the same was tested using a two-sample, two-tailed Student's t-test. The normality of the samples was checked using a Kolmogorov-Smirnov test. To compare replicates of the same experiment from different days, a 2-way-ANOVA test was done. For the ANOVA-test, one factor was defined as the different conditions/populations and one factor was defined as the different experimental days. This made it possible to take minor influences on deformability such as passage number or growth density

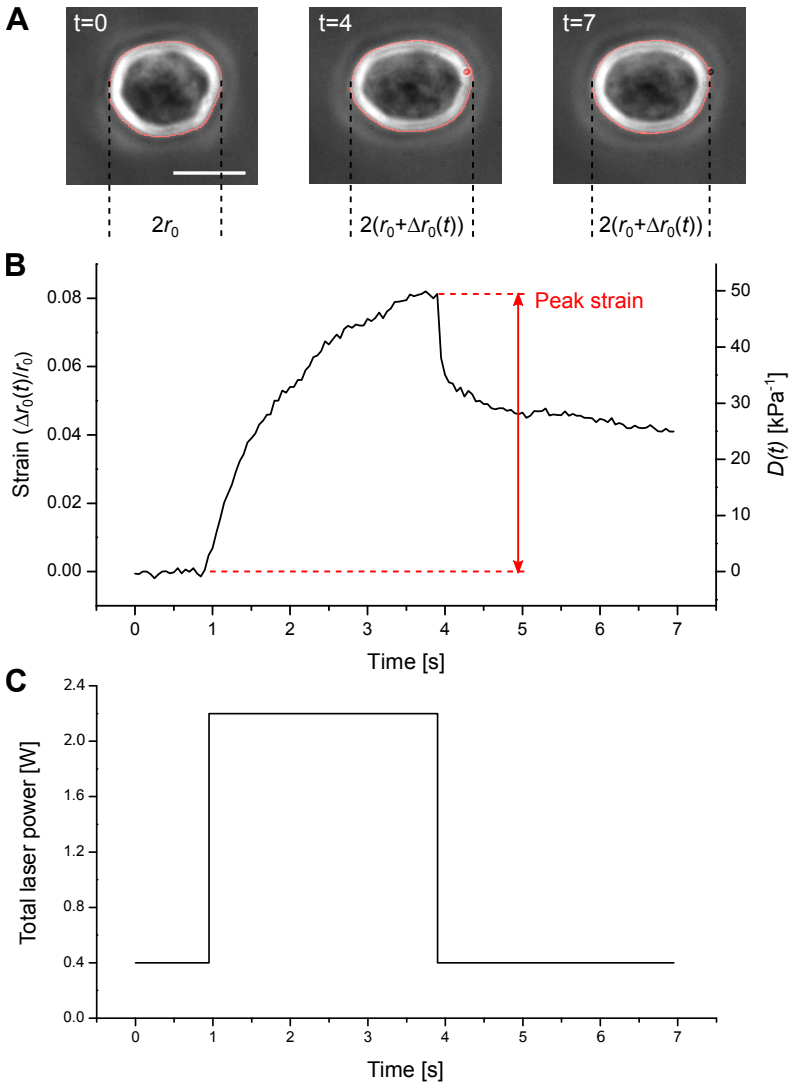

Figure 2.3. – Schematic of an optical stretcher measurement and data processing. Panel (A) shows a cell at three time-points of and OS measurement: At the beginning of the measurement (t=0), after 4 sec where the highest deformation is reached and at the end of the measurement after 3 sec of relaxation. The detected edges of the cell are highlighted in red. r_0 is defined as the radius of the cell along the laser axis. Scale bar 10 µm. To quantify the deformation, an ellipse is fitted to the edge and the relative deformation along the laser axis (strain, $\Delta r_0(t)/r_0$) is plotted as a function of time (B). The secondary y-axis shows the compliance *D(t)* of the cell as calculated by using the global geometrical factor. To compare multiple experiments, the peak strain as indicated in red was used in bar diagrams. (C) shows the total laser power for the step function applied during a measurement as a function of time.

into account. These varied slightly from one experiment to the next but were the same or very similar for all populations of a given day.

For stretching curves that represent more than one replicate, data points for all cells were pooled and the mean of all values is presented with SEM. For bar diagrams of the peak strain, the average of the means from individual experiments with the standard deviation is shown. Statistical significance is indicated by an asterisk (*) for $p \leq 0.05$ or two asterisks (**) for $p \leq 0.01$.

2.3.4. Compliance Calculation

The strain (relative deformation) of a cell or strain along the laser axis

$$\gamma(t) = \frac{\Delta r_0(t)}{r_0}\,, \tag{2.1}$$

where r_0 is the cell radius measured along the laser axis, can directly be used to compare different cell populations. However, it is also possible to calculate mechanical properties of the cells from OS measurements. For the creep compliance measurements performed in this study, this has been demonstrated by Lautenschläger [2011]. To calculate compliance values for the cells, informations about the setup of the optical stretcher and properties of the cells have to be known. Important factors for the stretcher setup are the trap geometry with the exact fiber distances, the materials used for the capillary and the laser power used. On the other hand, properties of the cells like their size, shape, refractive index and and Poisson's ratio play a role [Boyde et al. 2009; Ananthakrishnan et al. 2006]. The calculation of a geometrical factor F_g that takes these properties into account was described in [Ananthakrishnan et al. 2006]. The theory for the calculation of the peak stress on the cells along the laser axis, σ_0, was published in [Boyde et al. 2009]. The combination of these factors can be used to calculate a global geometrical factor F_{gg} in [Pa]. The compliance $D(t)$ can then be calculated as

$$D(t) = \frac{\gamma(t)}{\sigma_0 F_g} = \frac{\gamma(t)}{F_{gg}}\,. \tag{2.2}$$

The compliance $D(t)$ therefore has the units [Pa^{-1}].

The calculation of F_{gg} was done using a custom-made Matlab (MathWorks) program and the relevant input parameters are given in table 2.1.

Compliance values are only presented for untreated HN and LN cells for which we exactly measured the required parameters. None of the instrument parameters used to calculate F_{gg} was changed throughout the this study, and we found that small deviations of the cell size have

Table 2.1. – Parameters used for the calculation of the global geometrical factor F_{gg} of high and low Nanog cells. The parameters were either measured in experiments, values from material specifications or found out via personal communication with other lab members.

Parameter	Value	Comment
n_{medium}	1.335	Refractive index
n_{cell}	1.3768	Refractive index
$r_{spherical}$	6.08 µm	Radius of assumed spherical cell
ν	0.45	Poisson's ratio
ϵ	0.0662	Cell stretching ratio
λ	1064 nm	Laser wavelength
W_0	6.2 µm	Beam waist of fiber
P_l	1.1 W	Laser power left fiber
P_r	1.1 W	Laser power right fiber
D_gel	1 µm	Thickness of index matching gel
D_glass	42 µm	Thickness of glass capillary
D_med	38.5 µm	Distance capillary-cell middle
n_gel	1.449	Refractive index
n_glass	1.474	Refractive index

only minor influences on F_{gg}. Therefore, strain or peak strain values will be presented for all OS measurements. This allows easy comparison between all OS experiments, especially for those where we could not calculate the compliance, in particular nuclear deformation, due to the lack of theoretical models and refractive index values, which are hard to measure intracellularly.

2.3.5. Drug and Chemical Treatments

To test the role of different structures of the cell on deformability, cells were treated with different drugs or chemicals. To influence the actin cytoskeleton, cells were treated with cytochalasin D (Sigma-Aldrich C8273) which depolymerizes filamentous actin and greatly softens cells [Petersen et al. 1982; Wakatsuki et al. 2001; Mazumder and Shivashankar 2010]. To disrupt the microtubule cytoskeleton, nocodazole (Sigma-Aldrich M1404) was used. This drug was shown to block tubulin assembly and disrupt MTs [Head et al. 1985; Samson et al. 1979]. To influence chromatin condensation the histone deacetylase (HDAC) inhibitor trichostatin A (TSA, Millipore 19-138) was used [Yoshida et al. 1990; Tóth et al. 2004]. To reversibly condense chromatin, divalent cations ($MgCl_2$ and $CaCl_2$ (both Sigma-Aldrich)) were used. Divalent cations were shown to enhance chromatin condensation both *in vivo* and *in vitro* [Widom 1986; de Frutos et al. 2001; Pajerowski et al. 2007].

Except for cytochalasin D, which was added directly to the resuspended cells before OS experiments, the cells were incubated with the treatments prior to trypsinization. Times and concentrations are indicated in table 2.2. The medium used for resuspension and for the reservoirs of the

OS microfluidic system contained the same concentration of drugs or chemicals. The protocols were adapted from values in the literature [Mazumder and Shivashankar 2010; Tóth et al. 2004; Pajerowski et al. 2007; Lautenschläger 2011] or methods established in the lab were used.

Table 2.2. – The table gives an overview of the different treatments used to influence the cytoskeleton or chromatin condensation of ES cell in OS experiments. Concentrations, incubation time and proposed effect are indicated.

Treatment	Concentration	Incubation time	Effect
Cytochalasin D	1 µM	10 min	Actin depolymerization
Nocodazole	1 µM	1 h	MT depolymerization
Trichostatin A	330 nM	2 h	Chromatin decondensation
$MgCl_2$+$CaCl_2$	2 mM each	30 min	Chromatin condensation

2.3.6. Stretching of Nuclei within Intact Cells

For the quantification of nuclear deformation within living cells, the cells were stained with the cell permeable nucleic acid dye Hoechst 33342 (Invitrogen H3570). The cells were incubated with 5–10 µg/ml for 15 min prior to trypsinization and the dye was kept in the resuspension medium of the cells. Except for the Hoechst-staining, cells were processed in exactly the same way as for whole cell measurements. During the OS measurements a mercury lamp (Olympus) and a DAPI filter were used to visualize the blue fluorescence signal of the stained nuclei. Data analysis was performed in a similar way as for whole cells but was adapted to account for differences in the stretching behavior of cells and nuclei. The LabVIEW edge detection program was used to track edges of the nuclei and data were further processed using Matlab software. The peak strain for nuclear deformation was calculated as the median value of the ten timepoints with the highest deformation in the stretching period.

2.4. Cytoskeleton Stainings

2.4.1. Actin Staining

Actin stainings were performed using a phalloidin-Alexa Fluor 546 dye (A546, Invitrogen A22283). For stainings of cells in the attached state, samples were prepared and handled during staining as described in detail for HP1α-stainings in section 2.8.1. Cells were grown in 35 mm dishes, washed twice with prewarmed PBS and fixed in prewarmed 4 % formaldehyde in PBS for 10 min at RT. The fixative was removed and cells were washed three times with PBS. To permeabilize the cells they were incubated for 3–5 min in 0.1 % triton X-100 (Sigma-Aldrich T8787) in PBS

and washed twice afterwards. Phalloidin-A546 was diluted in a 1 % BSA solution in PBS for a final concentration of 165 nM and 60 µl were pipetted on the cells. A coverslip was placed on top and the cells were incubated for 20 min at RT in the dark in a moist chamber. Then, the coverslip was removed and the cells were washed three times with PBS. One drop of Vectashield mounting medium containing DAPI (4',6 diamidino-2-phenylindole) (Vector Laboratories, H-1200) was placed on a coverslip and cells were covered. The coverslips were allowed to settle for 1 h and then excess mounting medium was carefully removed and the samples were sealed using clear nail polish. For stainings of actin after cytochalasin D treatment the cells were incubated with 1 µM cytochalasin D for 30 min prior to fixation. For all washing steps and dilutions in staining procedures used after fixation of cells, 1x PBS prepared from a 10x concentrate was used (Sigma-Aldrich D1408).

For actin stainings of cells in suspension, trypsinized cells were left to settle on poly-D-lysine coated slides and subsequently fixed and stained. To prepare the coated slides, a liquid blocker pen (Daido Sangyo, Japan) was used to draw circles on microscopy slides. The circular wells were then filled with 100 µl of a 100 $^{\mathrm{mg}}/_{\mathrm{ml}}$ poly-D-lysine (PDL; P1149, Sigma-Aldrich) solution, incubated for at least 2 h or o/n (overnight) at RT and washed three times with PBS. The cells were trypsinized and resuspended at 0.5-1E6 cells/ml in LIF+ medium, optionally containing 1 µM cytochalasinD. 100 µl of resuspended cells were allowed to settle on poly-D-lysine coated slides for 30 min in a standard cell culture incubator at 37 °C. To fix the cells, 100 µl of an 8 % formaldehyde in PBS solution was added to the wells (final concentration 4 %) and slides were incubated for 10 min at 37 °C. From this point on, the actin staining protocol described above was followed except that for incubation with the staining solution the wells were not covered. Rectangular coverslips (24x55 mm) were used for mounting.

Actin stainings were imaged both in epifluorescence and confocal mode using a Leica SP5 II confocal microscope. Epifluorescence images were taken in a blue channel to image DAPI-staining of the DNA, a green channel for the eGFP signal and a red channel to image the phalloidin-Alexa Fluor 546. Confocal imaging was used to show detailed structure of the actin network. Confocal stacks were recorded at a distance in the z-axis of 1-1.5 µm.

2.4.2. Microtubule Staining

Stainings for MTs were performed based on the protocol as described in section 2.8.1 with minor modifications. Differences were as follows: Cell permeabilization was only performed using 0.1 % Triton-X 100 for 10 min and no saponin. As primary antibody (AB) an anti-β-tubulin AB (Invitrogen, 18-0093) was used at a dilution of 1:50 and as secondary AB a goat anti-mouse Alexa-Fluor 568 AB (Invitrogen A11004) in a 1:200 dilution. Mounting was done as described

for actin stainings using Vectashield mounting medium. It was found essential to use the non-hardening mounting medium for cytoskeleton stainings while for HP1α stainings the FluorSave reagent gave equally good results.

2.5. Analysis of Cellular and Nuclear Size

2.5.1. Experimental Procedure

To analyze the sizes of nuclei and cells in the suspended state as well as the nuclear versus cytoplasmic ratio (N/C ratio), I developed a staining and analysis routine. The N/C ratio was defined as the volume fraction of the nucleus from the whole cell. On day 0, cells were sorted (optionally) and seeded into a gelatinized 12-well plate at 1.04E5 cells per well and half of the growth medium was changed on day 1. On day 2, approximately 40 h after seeding, the cells were incubated with a staining solution for 30 min. The final concentrations of the dyes used were 5 $^{\mu g}/_{ml}$ Hoechst 33342 to stain the nuclei and 250 nM MitoTracker Orange CMTMRos (MTO, Invitrogen M7510). The unspecific staining properties of MTO used at this concentration were exploited to use it as a stain for the whole cell. To quanitify the effects of nocodazole and cytochalasin D on the nuclear and cellular sizes, cells were incubated with 1 µM of the respective drug together with the staining solution. Cells were then trypsinized, resuspended in 1 ml of medium, centrifuged at 200 g for 5 min and resuspended in 200 µl of staining solution in LIF+ medium. Cytochalasin D or nocodazole were also kept in the resuspension medium. For imaging, the cells were allowed to settle on coverslips (55x24 mm) that had been coated with PDL o/n as described in section 2.4.1. After 10 min of settling, cells were immediately imaged in epifluorescence mode using a 40x 1.25 NA oil objective. Imaging settings for the red and blue channel (MTO and Hoechst, respectively) were optimized for each sample. For each condition two replicates from different wells of the 12-well plate were taken. For each replicate at least three different regions were recorded and 100–250 cells per replicate were analyzed.

2.5.2. Data Analysis

To quantify the cellular and nuclear sizes, the images were processed in Fiji software (an ImageJ distribution [Rasband]). The basic strategy was to make the images binary where the size of particles can easily be found automatically. I found that the analysis of multiple cells simultaneously from one microscopy image did not give accurate results due to variations in staining strength between individual cells. Therefore, I developed an analysis routine to measure cell or nucleus areas individually.

The cells were cropped from an image and Fiji's batch job function was used to subtract background, threshold the images to binary masks and fill internal holes. The process was evaluated for nuclei and cells of different staining intensities by comparing the outlined binary masks with the original images and was found to detect cell/nuclear edges accurately. For the final measurement of cellular or nuclear size, particles were restricted to predefined criteria to exclude debris or cell doublets (0.6–1 circularity value, 30–200 μm^2 for nuclei and 60–250 μm^2 for cells). All cells and all nuclei were processed in the same way, respectively. The projected area was then used to estimate average radii for cells and nuclei. Statistical analysis was performed using Origin 8.5 software.

2.6. Cell Cycle Analysis

Cell cycle analysis was performed by quantifying the DNA content of a TNGA ES cell population using a flow cytometer. For DNA content measurements, cells were cultured in 6-well plates and incubated with 10 $\mu g/ml$ Hoechst 33342 for 15 min. To avoid losing any detached mitotic cells, the growth medium and PBS used for washing the cells prior to trypsinization was collected in a tube. After trypsinization, the collected medium/PBS was used to neutralize trypsin and cells were centrifuged (1000 rpm, 5 min) and resuspended in 1 ml PBS containing 10 $\mu g/ml$ Hoechst 33342. Cells were then directly analysed using a Dako CyAn ADP. When the cells were not analysed immediately, they were fixed after resuspension in 2 % formaldehyde in PBS for 15 min and stored at 4 °C. The Hoechst dye was added 15 min prior to FACS analysis.

The settings for the FACS analysis were similar to the ones described in section 2.2 with an additional channel for the Hoechst fluorescence signal. At least 25,000 viable cells were recorded per sample and analyzed using Summit Software (Beckman Coulter). Histograms for cell numbers versus linear Hoechst signal were created for both HN and LN cells as distinguished by their GFP signal. Data were exported for further analysis using Origin software.

To test the method we used, we did the same type of analysis for HL60 cells. As these cells grow in suspension, they were simply centrifuged and resuspended in PBS containing 10 $\mu g/ml$ Hoechst 33342 and fluorescence intensity was measured.

2.7. FRAP Experiments

2.7.1. Transfections with H2B-RFP

Plasmid

The plasmid-vector for the expresson of an RFP-tagged histone H2B was purchased from Evrogen (pTag-RFP-H2B vector, cat.#FP368). The tag-protein (TagRFP) was selected for its compati-

bility in microscopy with the *eGFP* transgene having its excitation and emission maxima at 555 and 584 nm, respectively. The monomeric structure and bright fluorescence were also considered as important features for FRAP experiments as dimerization of the tag-proteins may influence diffusion properties of the labelled histones. The H2B-RFP construct is under the control of a $P_{CMV\ IE}$ promotor and the vector also features kanamycin and neomycin (G418) resistance genes for selection in prokaryotic and eukaryotic cells, respectively.

Plasmid Amplification

To amplify the amount of plasmid, competent DH5α E. coli cells (kindly provided by N. Thomson) were transformed with the plasmid. 200 µl of competent cells were thawed on ice and 100 ng of plasmid DNA was added. After incubation for 30 min on ice, the bacteria were heat-shocked for 45 sec at 42 °C, put back on ice and 800 µl LB medium was added. The cells were then incubated on a shaker at 37 °C for 30 min and 250 µl were plated on a LB+kanamycin plate (30 µg/ml) and incubated o/n.

The plate with individual colonies was stored at 4 °C and for minipreps individual colonies were picked and incubated in 5 or 10 ml of LB+kanamycin (30 µg/ml) on a shaker o/n at 37 °C. Frozen stocks were made the next day by mixing 300 µl of bacterial culture with 300 µl of a 50 % glycerol solution and freezing them at −80 °C. For plasmid purifacation, the equivalent of 5 ml bacteria culture was harvested in 2 ml Eppendorf tubes by centrifugation in a table-top centrifuge (1 min, full speed). Extraction of the plasmid was done using the GeneJET Plasmid Miniprep Kit (Fermentas K0503) and all steps were performed according to the manufacturer's protocol. The DNA concentration of the purified plasmid was measured using a Nanodrop 2000 (Thermo Scientific) and was between 280–400 ng/µg. To assure the quality of the plasmid, 350 ng of both linearized and undigested plasmid were loaded on a 0.8 % agarose gel containing SYBRSafe (1:10,000, Invitrogen S33102), separated for 1 h at 80 V and imaged under UV light in a GelDoc-It imaging system (UVP).

Transfection

For the transfection of TNGA cells with pTag-RFP-H2B, Lipofectamine LTX and PLUS Reagent (Invitrogen 15338-100) were used. Transfection conditions were carefully optimized according to guidelines provided by the manufacturer. Best results for 35 mm dishes were obtained using 1000 ng of DNA, a ratio of 5:1 of LTX reagent (in µl) to DNA (in µg), and using 1 µl PLUS reagent for the DNA obtained from the minipreps. Using no PLUS reagent was found to work better with the original plasmid from Evrogen. Repeated freeze-and-thaw cycles of the plasmid DNA proved

to affect transfection efficiency and therefore DNA was stored at 4 ℃ for short-term storage and only stored at −20 ℃ for long-term storage.

The final protocol used for FRAP experiments was as follows: 2.4E6 TNGA cells in 2 ml of LIF+ medium were seeded in gelatinized 35 mm diameter μdishes (Ibidi 80136) on day 0 so that cells were about 50 % confluent for transfection after 20 h on day 1. For the transfection mix, the amount of plasmid DNA solution equalling 5 µg was mixed with 500 µl prewarmed (37 ℃) LIF+ medium, 5 µl PLUS reagent was added, mixed gently and incubated for 10 min. 25 µl LTX reagent was then added, the solution was mixed again and incubated at RT for 30 min. All mixing steps were performed by pipetting up and down for 3–5 times with a P1000 pipette. After incubation, the transfection mix was added dropwise to the cells and the medium was mixed by gently rocking the dish. Cells were then incubated for about 20 h prior to FRAP experiments and the whole medium was changed after 6 h post transfection.

2.7.2. FRAP Microscopy

All FRAP experiments were performed using a Leica SP5 II confocal microscope equipped with an environmental chamber to control for temperature and CO_2 concentration (BOC Gases 225742-L). All experiments were performed at 37 ℃ and with 5 % CO_2 concentration using the HCX PL APO CS 63.0x NA 1.4–0.6 OIL UV objective. After initial problems with focus drifts over time both in the z-axis and in x-y, the heating of the environmental chamber was switched on at least 2 h prior to any measurements to ensure temperature equilibration of the whole equipment. Furthermore, a metal stage inset was used and the μdishes were attached firmly to the stage inset by squeezing in blue tack around the edges of the dish to fill the gap between the dish and the rim of the stage inset.

The FRAP Wizard of the Leica LAS AF software was used to configure the settings for FRAP experiments. To reduce acquisition photobleaching to a minimum, imaging settings and especially framerates were adjusted for the investigation of histone dynamics on different time scales ranging from 15 sec to 30 min. To ensure both good bleaching depth in the z-axis and high section thickness spanning the whole nucleus, the numerical aperture of the objective was reduced to approximately 1 by using the built-in iris diaphragm of the objective. Settings that seemed to represent the best compromise between imaging quality, time resolution and acquisition photobleaching are summarized in table A.1 (see appendix) for different time-scales.

Only cells that were clearly GFP-positive or GFP-negative were used for FRAP experiments. Prior to starting the FRAP experiment an image was taken of every cell which included a green channel to discriminate HN and LN cells and a PMT-trans channel in bright field mode was included to ensure only morphologically normal cells were included in the measurements.

2.7.3. FRAP Data Analysis

Image Analysis

For image analysis the Fiji software was used. First, the individual FRAP-series were exported from the .lif files produced by the Leica imaging software using Fiji's LOCI plugin [Linkert et al. 2010]. For each individual cell, the Stackreg plugin [Thévenaz et al. 1998] using the 'Rigid Body' option was run to correct for movements of the cell in the x- and y-axis and rotations. Measurements with strong movements or focus drift were excluded from the analysis.

To measure the intensities for the quantitative analysis, the FRAP Norm plugin by FA Meys for ImageJ was used. The plugin allows the simultaneous measurement of several regions in an image stack and the different regions were defined. The selections were chosen in a way that only the intensities of regions that stayed in place over the whole image series were measured. The regions were defined as follows:

- FRAP region: bleached region of the nucleus, I_t
- Background: a region outside the cell, B_t
- Whole cell: the whole area of the nucleus including the bleached area, N_t
- Reference: an unbleached region of the nucleus

The measurement mode was set to 'Automatic' and the 'Double normalization' (DN) method was chosen. The normalization procedure is based on the method described by Phair et al. [Phair and Misteli 2000; Phair et al. 2004]. Before normalization, the background signal B_t for each time-point is subtracted from the measured values for each time-point. The first normalization step normalizes the signal of the FRAP region to its pre-bleach value (I_t/I_0). The fluorescence intensity of the whole nucleus for each timepoint is then compared to the averaged prebleach value to calculate a correction factor to account for signal intensity lost during the bleach pulse and also during the imaging process (N_0/N_t). The relative (double normalized) intensity of the FRAP region is then calculated as

$$I_{\mathrm{DN}} = \frac{(N_0 - B_0)(I_t - B_t)}{(N_t - B_t)(I_0 - B_0)}\,. \tag{2.3}$$

For easier graphical comparison, we then normalized the curves so that the first post-bleach value was set to zero by subtracting all values with the DN-signal of $t = 0$ (triple normalization).

2.8. Quantitative Analysis of HP1α-Distributions in the Nucleus

2.8.1. Immunofluorescence Staining for HP1α

The following HP1α-staining protocol is modified from Bártová et al. [2007]. To prepare for the stainings, cells were trypsinized, sorted (optionally) and resuspended in LIF+ medium. The cells were counted and diluted to a concentration of 1.2E5 cells/ml. 2 ml of suspended cells were seeded in gelatinized 35 mm dishes and incubated. Optional treatments with TSA (400 nM, 2 h) or $MgCl_2$+$CaCl_2$ (2 mM each, 30 min) were performed immediately before fixation. When the cells reached about 70 % confluency, typically 24–36 h after seeding, cells were washed twice with 2 ml of prewarmed PBS and fixed for 10 min at RT in prewarmed 4 % formaldehyde in PBS. The dishes were then washed twice with PBS and processed immediately or stored covered with 2 ml PBS at 4 ℃. For permeabilization, we incubated the cells first with 0.1 % triton X-100 diluted in PBS for 8 min and then with 0.1 % saponin for 12 min. The dishes were washed twice with PBS for 10 min and then blocked for 1 h with 1 % BSA dissolved in PBS and washed for 15 min in PBS afterwards. The anti-HP1α antibody (Millipore, 05-689) was diluted 1:200 in 1 % BSA in PBS and after removing all excess liquid, 60 µl of diluted antibody were pipetted into the middle of the dish. The middle of the dish was carefully covered with a round 22 mm coverslip and the dish was incubated o/n (overnight) at 4 ℃ in a moist chamber in the dark. To remove the coverslip, 1 ml of PBS was slowly pipetted against the wall of the dish so that the coverslip would float up. The cells were washed twice for 5 min in PBS and then incubated with 60 µl of a 1:200 dilution (in 1 % BSA in PBS) of an Alexa Fluor 633 (A633) goat anti-mouse (Invitrogen A21126 lot. 774900) for 1h at RT in the same way as with the primary antibody. The stained cells were washed three times for 5 min with PBS. To mount the cells, all liquid was removed and one drop of FluorSave reagent (Calbiochem 345789) was dropped on a 22 mm coverslip which was carefully dropped on the cells with the mounting medium facing the cells. The dishes were kept on RT in the dark for 2 h to allow the mounting medium to dry and then imaged immediately or stored at 4 ℃.

2.8.2. Confocal Microscopy

The stained cells were imaged using a Leica SP5 II microscope. The images were recorded with the 63x 1.4 NA oil objective using an additional zoom factor of 1.7. The resulting pixel size was 141.5 nm and to obtain good quality images the imaging speed was reduced to 200 Hz and 3 lines and frames were averaged. Two channels were recorded where the eGFP was excited at 488 nm and the A633-coupled AB at 633 nm. Laser intensities were kept the same for all experiments.

Gain settings were kept the same for all samples of one experiment but were adjusted using the 'autogain' function of the microscope software for each experimental day. In each experiment multiple replicates (2–5) of stained dishes were imaged, and 5–7 different regions from each replicate were imaged and analyzed.

2.8.3. Image Processing and Analysis

The image analysis for the HP1α-stainings was optimized to find differences in the spatial distribution of HP1α. The analysis of fractal dimension D_F was found to be a good way to quantify the staining patterns, as it was also demonstrated by Tóth et al. [2004] in a similar way. Generally, D_F is a measure for complexity and is defined as the scaling rule for how the detail of a pattern changes with scale [Karperien 2007]. It defines the relationship between N, the number of pieces, and ϵ, the scale used to get the new pieces as given in

$$N \propto \epsilon^{-D_F} . \tag{2.4}$$

For digital image analysis of immunohistochemistry stains we used the box counting dimension D_B which can be calculated from the relation between the box count N_ϵ and box size ϵ in box counting as

$$D_B = \lim_{\epsilon \to 0} \frac{\log N_\epsilon}{\log \epsilon} . \tag{2.5}$$

The limit is found as the slope of the regression line [Karperien 2007]. For the sake of clarity, the calculated box counting dimension is referred to as fractal dimension or D_F in text and figures.

In the analysis routine, all individual nuclei from a single microscopy image were cropped using the magic wand tool in Fiji and saved as individual files as a first step. A Matlab program was used to threshold the individual images of nuclei. The median pixel value was used as a threshold. To finally get the fractal dimension, the ImageJ plugin Fraclac [Karperien 2007] was used. A standard box count was run for all nuclei of a given sample and the relevant options were set to allow autothresholding to binary and to use white as background color. The number of grid positions was set to 4 and the default options for calculating grid calibers were applied (default box sizes, minimum size 2 pixels and maximum box size 45 % of ROI). The values for D_B were imported to Origin software and plotted as histograms or as average of the means of several replicates with SD as error. Statistical analysis was done using two-tailed Student's t-tests and 2-way-ANOVA tests.

2.9. Equipment List

Table 2.3 lists the items used in general lab routine, optical stretching experiments and confocal/epifluorescence microscopy.

Table 2.3. – Equipment used in stretching experiments, microscopy and general lab routine

Optical Stretcher Equipment		
Item	**Specification**	**Company**
Microscope	Eclipse TE2000-U	Nikon
Objective	Plan Fluor ELWD 40x/0.60 NA	Nikon
1064 nm Laser	YLM-5-1070-LP	IPG Photonics, UK
Camera	ORCA-05G	Hamamatsu
Camera	Marlin F146B	AVT
Mercury lamp		Olympus
Software	LabVIEW, custom-made	National Instruments
Leica TCS SP5 II Microscope		
Item	**Specification**	**Company**
Stage	DM 6000 CFS	Leica Microsystems
Stage control	CTR 6500	Leica Microsystems
Camera	DFC 350 FX	Leica Microsystems
Lasers	Argon and HeNe 633	Leica Microsystems
WLL Laser	TCS SP5 X	Leica Microsystems/Koheras
Environmental chamber heating	Cube	Life Imaging Services
Objective	HC PL Fluotar 10x0.3 NA dry	Leica Microsystems
Objective	HC PL Fluotar 20x0.5 NA dry	Leica Microsystems
Objective	HCX PL Fluotar L 40x0.6 NA dry	Leica Microsystems
Objective	HCX PL APO CS 40x1.25-0.75 NA Oil UV	Leica Microsystems
Objective	HCX PL APO CS 63x1.4-0.6 Oil UV	Leica Microsystems
Objective	HCX PL APO CS 100x1.4-0.60 NA Oil UV	Leica Microsystems
Software	LAS AF 2.2.0	Leica Microsystems
Cell culture and general lab equipment		
Item	**Specification**	**Company**
Rocking platform	Unimax 1010	Heidolph Instruments
Heating/stirring platform		Fisher Scientific
ddH_2O system	Synergy	Millipore
−80 ℃ freezer	VX 380 E	Thermo Electron Corporation
Liquid nitrogen strorage device	Arpege 40	Air Liquide
Incubator (cell culture)	Hera cell	Heraeus
Incubator (cell culture)		Binder
Incubator (bacteria)	Heraeus function line	Thermo Scientific
Centrifuge	5810 R	Eppendorf
Centrifuge	Fresco 17	Thermo Scientific
Cell culture hood	Hera safe	Thermo Scientific/Heraeus
Microscope	AE 31	Motic
Camera	DMK 21F04	Imaging Source
Mercury lamp	MHG-100B	Motic
Software	IC capture 2.1	IC capture
PCR cycler	TC-512	Techne
Agarose gel chamber	T-V-Gel	Fisherbrand
Electrophoresis power supply	MP-250 V	Cleaver Scientific Ltd.
UV imaging chamber	GelDoc-It	UVP
Spectrophotometer	Nanodrop 2000	Thermo Scientific
Balance	PM 4600	Mettler
Balance	AG 135	Mettler Toledo
pH meter	PH 210	Hanna Instruments

3. Results

Most of the work described in this section was done by myself, however, as the project was done in close collaboration with K. Chalut, some of the results he obtained are presented here as well. In particular, much of the work presented in section 3.4 was done by K. Chalut, although I was involved in setting up the method of nuclear stretching. Also, data taken for fig. 3.11 were taken by him. I found it necessary to include relevant experiments as some of my work would be out of context otherwise.

3.1. Mechanical Changes in Mouse Embryonic Stem Cells Correlate with Nanog Expression

The project I was involved in for my diploma thesis resulted from a collaboration of our laboratory with the group of Alfonso Martinez Arias (Department of Genetics, Cambridge University). In this project we aimed to investigate the mechanisms that are involved in the regulation of pluripotency and the transition to a differentiation-prone state in mouse embryonic stem cells. While the research interests of our collaborators were mainly focussed on the biochemical regulation and specifically the transcription factor networks controlling pluripotency [Kalmar et al. 2009], we concentrated on the biophysical aspects of pluripotency. For our experiments, we used an mES cell line that was generated in the lab of Austin Smith and allowed monitoring of Nanog expression via the expression of an *eGFP*-reporter gene that was inserted into one of the *Nanog*-loci [Chambers et al. 2007]. This modification made it possible to use fluorescence activated cell sorting (FACS) to separate cells with high expression levels of Nanog (HN) from cells with low Nanog expression levels (LN) [Chambers et al. 2007; Kalmar et al. 2009]. Preliminary results by K. Chalut indicated that the expression of the Nanog transcription factor was correlated to mechanical properties of the cells. In particular, LN cells were shown to be more compliant than HN cells. Several factors of the setup I used (cell passage number, serum, equipment setup) had changed since those experiments and so I first aimed to reproduce those findings. For cell mechanics measurements we used an optical cell stretcher (OS) [Guck et al. 2001].

Direct comparison of HN and LN cell mechanics measurements revealed that low Nanog cells were more deformable on average (fig. 3.1). When creep compliance measurements using a step stress were performed I found significant differences in the peak deformation (peak strain, PS) after 3 sec of stretching (fig. 3.1). The relative differences between HN and LN cells were small and not significant within individual experiments (except exp. 5) but were reproducible and statistical analysis of 5 experiments resulted in a highly significant negative correlation between Nanog expression levels and cell deformability (fig. 3.1 B and C). HN cells showed peak strains of 0.0425 ± 0.0045 and LN cells showed peak strains of 0.0487 ± 0.0077 (average of the means of 5 experiments ± SD, fig. 3.1 C).

From these OS measurements I calculated the creep compliance of HN and LN cells according to the models described for the calculation of stress on the cell surface and the conversion of strain measurements to compliance using the global geometrical factor F_{gg} [Boyde et al. 2009; Ananthakrishnan et al. 2006; Lautenschläger 2011] (see section 2.3.4). To this end, the refractive index (n_{cell}) for HN and LN cells was determined by digital holographic microscopy by K. Chalut and the radii (r) for HN and LN cells were measured (see section 3.3). Both values were identical within a 95 % confidence interval for HN and LN cells and I used $n_{cell} = 1.3768$ and $r = 6.08\,\mu\text{m}$ as averaged input values for my calculations. The global geometrical factor was calculated to be $F_{gg} = 1.643\,\text{Pa}$. By division of the peak strain by the F_{gg} I got peak compliance values of $D = 0.0259 \pm 0.0028$ for HN cells and $D = 0.0296 \pm 0.0047$ for LN cells. This is equivalent to an increase in compliance of 14.5 % from HN to LN cells. The compliance $D(t)$ is indicated in the plots of fig. 3.1 as the secondary y-axis.

Preliminary studies had suggested that cells with low Nanog expression are more deformable than cells with high Nanog expression and I reproduced this result using an entirely new setup. Starting from this observation I investigated which components of the cells caused the differences in cell compliance.

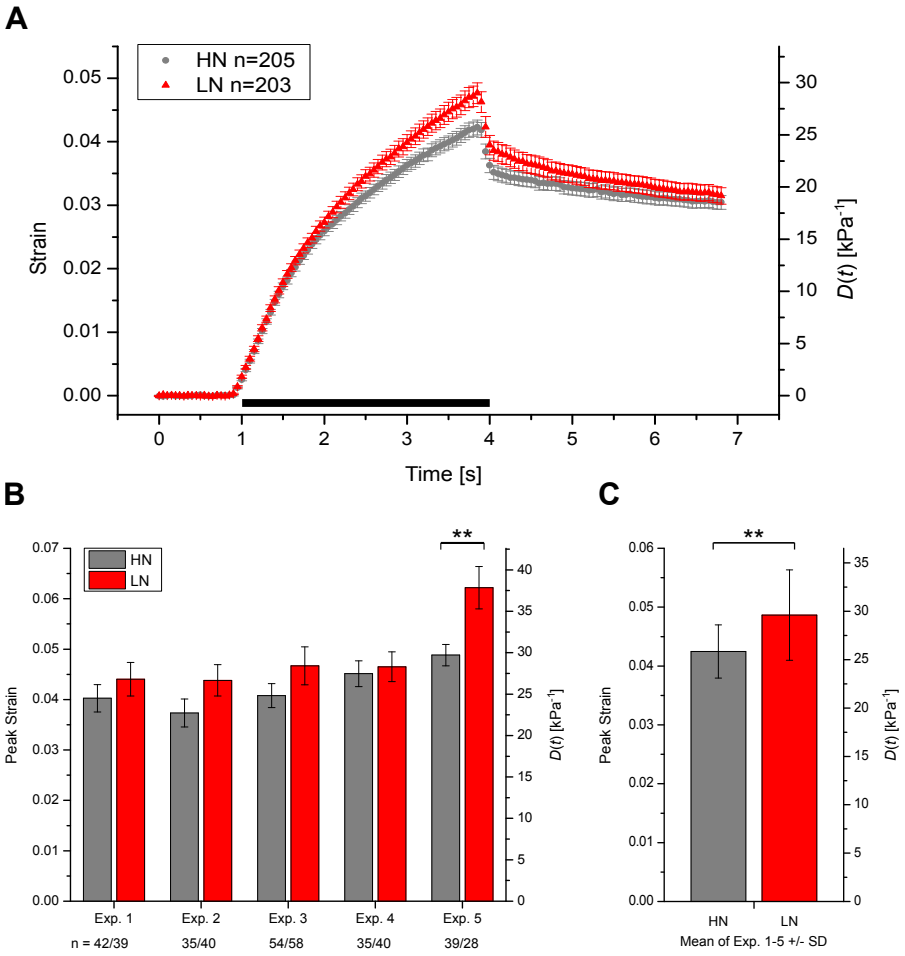

Figure 3.1. – Optical stretcher measurements of TNGA mouse embryonic stem cells sorted into high Nanog (HN) and low Nanog (LN) cells. (A) Averaged deformation curves of HN (grey circles) and LN (red triangles) cells from 5 experiments with standard error of the mean (SEM). The primary y-axis gives the relative deformation (strain) while the secondary y-axis gives the compliance $D(t)$. The black bar along the x-axis highlights the time when the laser was on stretch-power (2.2 W); total laser power during initial trapping and relaxation was 0.4 W. These values apply for all OS measurements in this study. (B) Bar diagram of the peak strain values of HN and LN cells from 5 independent experiments. Cell numbers for each experiment are indicated (HN/LN). Error bars indicate SEM. (C) Summary of 5 experiments as the averaged mean values ± SD. (**) indicates $p \leq 0.01$ and (*) $p \leq 0.05$ in all figures.

3.2. The Role of Cytoskeletal Elements in Cell Mechanics of mES Cells

Mechanical properties of cells are generally thought to be dominated by the cytoskeleton [Alberts et al. 2002]. It has been shown in other studies with the optical cell stretcher that especially the filamentous actin (f-actin) network is important for cell compliance [Lautenschläger et al. 2009; Ananthakrishnan et al. 2006] as well as the microtubule (MT) network [Lautenschläger et al. 2009; Lautenschläger 2011]. I used chemical treatments that were shown to influence the polymerization behavior of actin and tubulin to modify these cytoskeletal networks.

In order to disrupt filamentous actin, I used cytochalasin D (cytoD). The treatment resulted in a great increase in deformability for both HN and LN cells (fig. 3.2 A). For both populations, the peak strain was increased about 2.7-fold (fig. 3.2 A and C) in comparison to untreated cells. Interestingly, I still found that the low Nanog population of cells (mean PS $= 0.1305 \pm 0.00543$ SD) was more deformable than the high Nanog population (PS $= 0.1146 \pm 0.00246$ SD). The relative difference (+13.9 %) was almost unchanged from experiments with untreated cells.

After treatment with nocodazole to inhibit tubulin polymerization, I found a softening for both HN and LN cells on average (fig. 3.2 B and C). Nevertheless, these experiments were not very reproducible and in two out of four experiments the high Nanog cells were more deformable than the low Nanog cells (fig. 3.2 B). On average, the LN cells were 7.6 % more deformable in 4 experiments (not significantly).

As the disruption of the filamentous actin led to such drastic changes in cell deformability, I investigated the structure of the actin network in mES cells. To see the structure of the network in the suspended state in which cell mechanics were probed, I trypsinized the cells and only then fixed and stained them. With a phalloidin-staining, which is specific for filamentous actin, I found that subcortical actin aligns smoothly underneath the cell membrane (fig. 3.3 (A) and (B)). No stress fibers were observed, except for cells that started attaching to the surface of the cover-slip. In contrast to this, I found that the smooth actin network was completely destroyed in cells treated with cytoD (3.3 (C) and (D)). The cell mechanics data together with the stainings are in agreement with previous findings that the subcortical actin network plays a crucial role for cell compliance [Lautenschläger et al. 2009; Ananthakrishnan et al. 2006].

Preliminary studies of collaborators (S. Muñoz-Descalzo) suggested that there might be differences in the subcellular organization of the actin and MT network in correlation to pluripotency and Nanog expression. Particularly, f-actin seemed to be down-regulated when cells were cultured in conditions that kept cells in a stably pluripotent state (HN). Therefore, I examined the cytoskeletal network of HN and LN cells in the attached state by confocal and epifluorescence

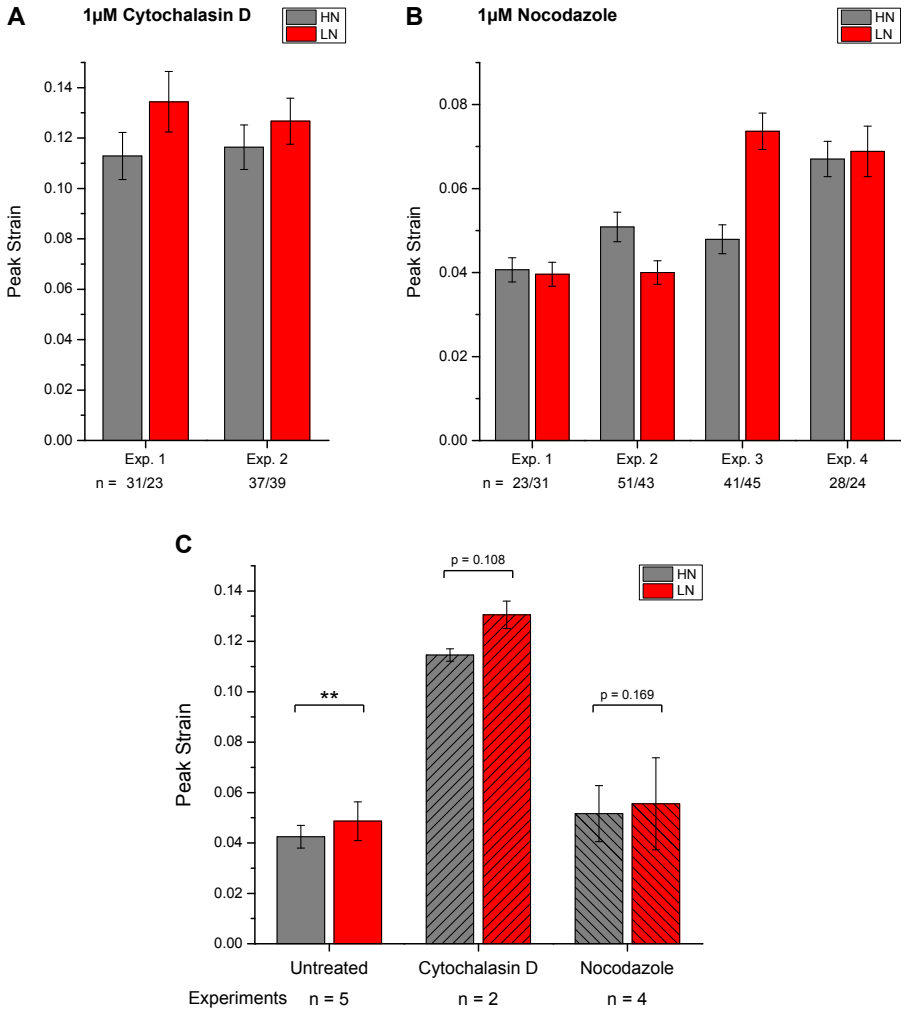

Figure 3.2. – The effect of cytoskeleton disrupting chemicals on mES cell deformability. (A) and (B) Mean peak strain values for individual experiments (± SEM). (A) Cells sorted into HN and LN cells were treated with 1 µM cytochalasin D and OS measurements were performed. (B) Peak strains of OS measurements for HN and LN cells treated with 1 µM nocodazole for 30 min. (C) Summarized results from cytochalsin D and nocodazole treatment experiments (striped bars) in comparison with untreated cell measurements (smooth bars) as presented in section 3.1 (Averaged means of several experiments ± SD).

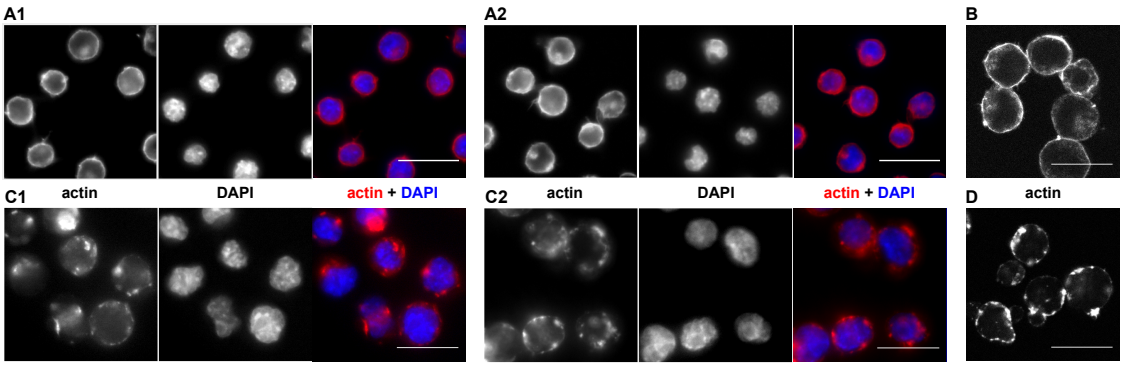

Figure 3.3. – Trypsinized cells stained for actin and DNA. (A) Phalloidin-A546/Hoechst 33342 stainings of HN (A1) and LN (A2) cells. A green channel is not shown due to strong leak-through of A546. (C) Actin stainings of cells that were treated with cytochalasin D (Cyto D). The apparent size change with cytochalasin D treatment is due to the usage of a different mounting medium for stains shown in panel (C). (B), (D) High resolution confocal images of trypsinized cells without and with cytoD treatment, respecitvely. All scale bars 20 µm.

microscopy. Mouse embryonic stem cells do not proliferate properly when cultured on glass and so most staining protocols involve centrifugation of trypsinized cells on coated glass cover-slips prior to fixation (cytospin). I wanted to investigate the cytoskeleton in normal culture conditions, so this procedure seemed not suitable for my purposes. Therefore, I developed a staining protocol that allowed staining of mES cells in regular culture dishes combined with high resolution confocal imaging.

Figure 3.4 shows confocal and epifluorescence images of both HN and LN cells. The typical growth pattern in colonies that arise from individual (or very few) cells is clearly visible (see also fig. 3.6 A). At the bottom part of a colony where cells attach to the substrate (fig. 3.4 panels A1 and B1, column labelled '0 µm') focal adhesions that appear as small bright spots are visible. Also, small protrusions that contain actin fibers (presumably stress fibers) can be found especially around the edges of the colonies. Confocal slices taken further away from the substrate (fig. 3.4 panels A1 and B1, column labelled '2 µm') reveal that at this height, there is almost exclusively subcortical actin that aligns at the edges of the cells and at cell boundaries. The DAPI-counter-staining in the epifluorescence images (fig. 3.4 panels C and D) shows that most of the volume within the cell boundaries where no actin filaments are visible is occupied by the nucleus.

Three replicates of sorted HN and LN cells were stained for f-actin as well as mixed TNGA populations. I did not find any apparent differences in the f-actin structure and no consistent changes in signal intensity were observed.

Figure 3.5 shows the organization of the MT-network in HN and LN cells. Very similar to the the actin-network, the MTs are dispersed at the bottom of the colonies and also protrude into cell processes. Further away from the substrate, the MT align to the edges of the cells and embed

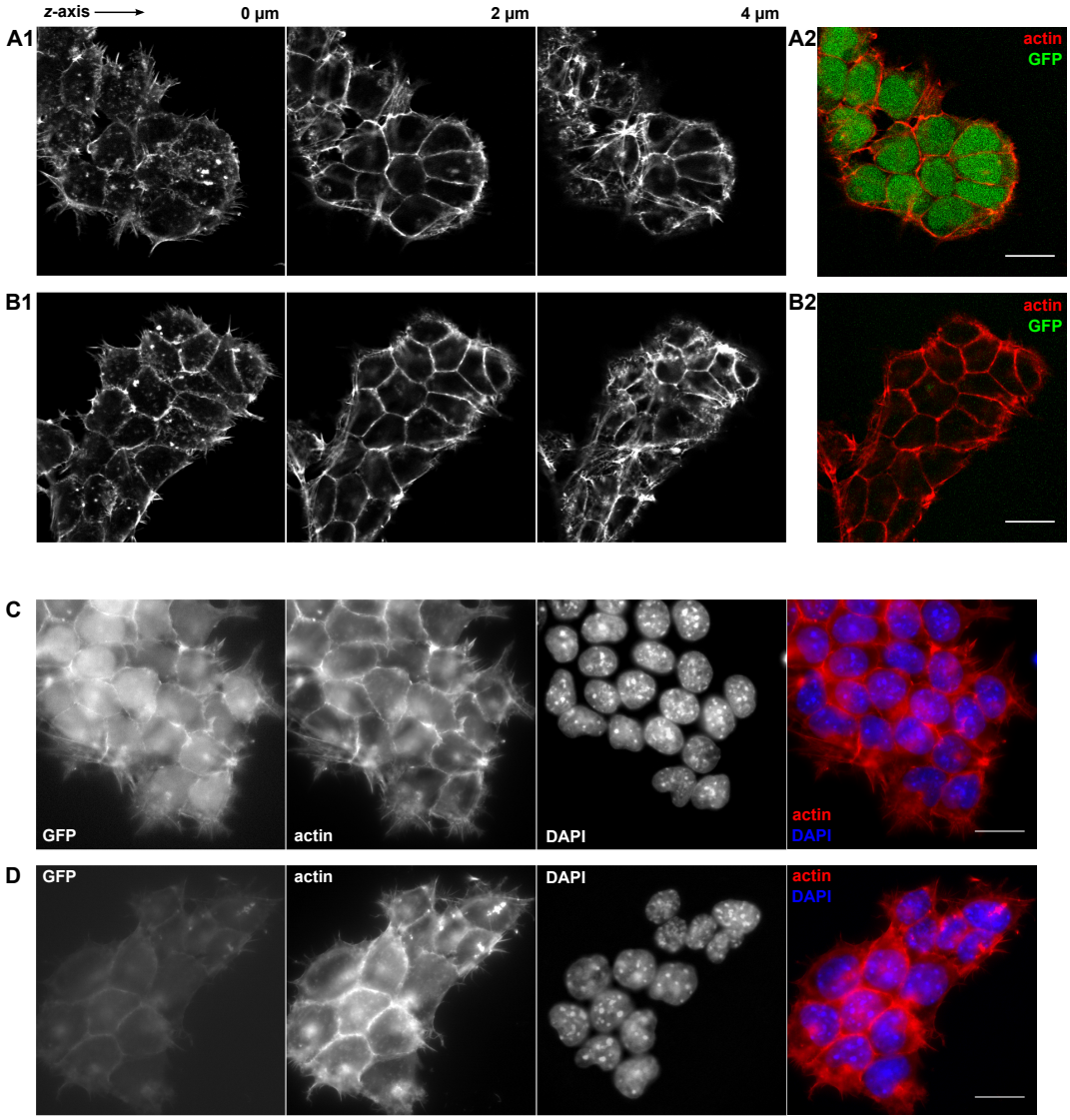

Figure 3.4. – Actin stainings of mES cells with phalloidin-Alexa 546. (A1) and (B1) Single sections of confocal z-stacks spaced by 2 µm for sorted HN and LN cell colonies, respectively. 3 sections from the bottom, where cells attach to the substrate (left, labelled 0 µm) to the top part of a colony (right, labelled 4 µm) are shown. (A2) and (B2) Overlays of the middle sections (2 µm) of (A1) and (B1) with the green channel to highlight the *eGFP*-reporter gene expression. (C) and (D) Epifluorescence images of sorted HN and LN populations. For the merged images only the actin- and DAPI-channels were included for clarity as there is a strong leak-through of the A546 signal to the green channel. DAPI-stained nuclei could not be imaged in confocal mode because UV-excitation was not available. All scale bars 20 µm.

the nucleus. At the top part of the colonies, the MT network again appears more dispersed. As for f-actin I did not observe any consistent structural differences in the MT cytoskeleton.

Optical stretching experiments demonstrated that the actin-cytoskeleton is crucial for mES cell mechanics in the suspended state while MTs seem to play only a minor role. Stainings of f-actin showed that actin occurs mainly as a smooth sub-cortical network in suspended cells. Confocal imaging of cytoskeletal networks in attached cells did not reveal any changes from the HN to the LN state. Taken together, we did not find any indications that the actin or MT networks were responsible for the changes in cell mechanical properties from HN to LN cells.

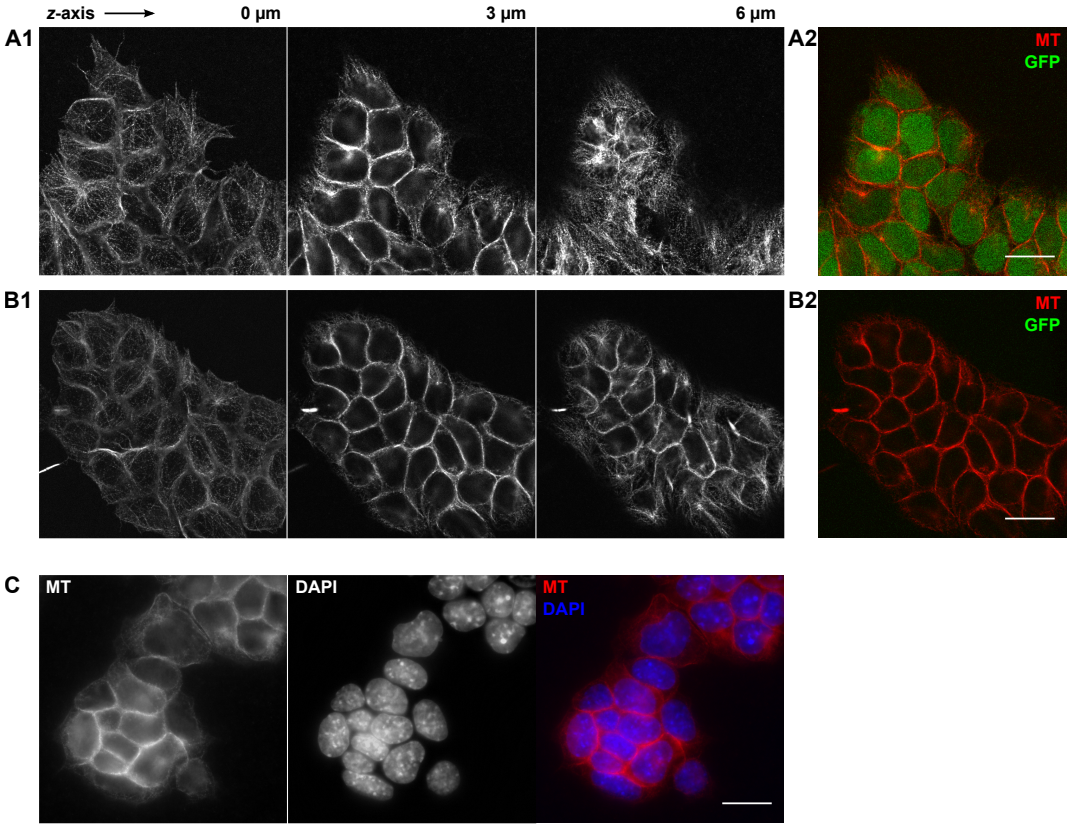

Figure 3.5. – Stainings for microtubules of sorted HN and LN cells. (A1) and (B1) Single sections of confocal z-stacks of HN and LN colonies, respectively. Three sections spaced by 3 µm from the bottom (left) to the top part (right) of a colony are shown. (A2) and (B2) Overlays of the middle sections with a green channel that was recorded simultaneously. (C) MT-staining of unsorted TNGAs counterstained with DAPI in epifluorescence. All scale bars 20 µm.

3.3. Cell Cycle Analysis and Cell-Morphology Examination

There are a number of properties of a cell apart from cytoskeletal networks that have been shown to alter cell deformability. These are in particular the cell cycle stage of a cell [Tsai et al. 1996], and the size of a cell, which can change the stress distribution on the cell surface in OS measurements [Boyde et al. 2009; Ananthakrishnan et al. 2006]. Furthermore, it became apparent in the cytoskeleton stainings that the nucleus occupies a large proportion of the total cell volume in mES cells. As it is the biggest and usually stiffest organelle in the cell [Guilak et al. 2000; Caille et al. 2002], I hypothesized that changes in the ratio between the nuclear volume and the total cell volume (nuclear to cytoplasmatic (N/C)-ratio) would influence cell compliance in OS experiments. I therefore investigated all of these factors in a quantitative manner.

When culturing TNGA cells, I did not observe any morphological differences in how the cells grew in culture dishes between pure HN, LN and unsorted TNGA cultures (fig. 3.6 A). Also, no differences in the proliferation rates of the cells were observed. The cell doubling time was calculated to be around 16 h based on a 1:8 split every 48 h in routine cell culture work. I did a cell cycle analysis based on DNA-content measurements using FACS to get a more quantitative comparison of the proliferation rate of HN and LN cells. I stained the cells with a live cell DNA-specific dye (Hoechst 33342) and quantified the fluorescence signal. Simultaneous recording of the Nanog-correlated GFP-signal of the cells allowed to discriminate between HN and LN cells. The distorted single peak I found (fig. 3.6 B1) is in accordance to the literature on proliferating mouse ES cells where about 75 % were found to be in S-phase and no clear G0/G1- or G2/M-peaks could be distinguished [Savatier et al. 2002]. Two replicates of live cells gave equal results and two replicates of cells that were fixed prior to FACS analysis also showed a very similar profile. To test the validity of the method with another cell line, I performed the same analysis for HL-60 cells, a human promyelocytic leukemia cell line that was available in our lab (courtesy of A. Ekpenyong). I found the expected two-peaked distribution for these cells, with still a relatively high percentage of cells in S-phase which is in agreement with data in the literature on this HL-60 cell line. (fig. 3.6 B2).

In follow-up studies, cell cycle analysis for TNGA cells was repeated using alternative protocols (DAPI or propidium iodide (PI) stainings). These experiments revealed a two-peaked distribution for TNGAs, however, there were still many cells in S-phase (K. Chalut, personal communication). These more recent results indicate that the Hoechst-staining method I initially used was not as accurate, possibly due to a non-linear relation of fluorescence intensity to DNA-content. However, in all these measurements we did not find any differences between the HN, LN or TNGA populations. Therefore, we ruled out that differences in the relative cell cycle stage distribution caused the mechanical differences we had found.

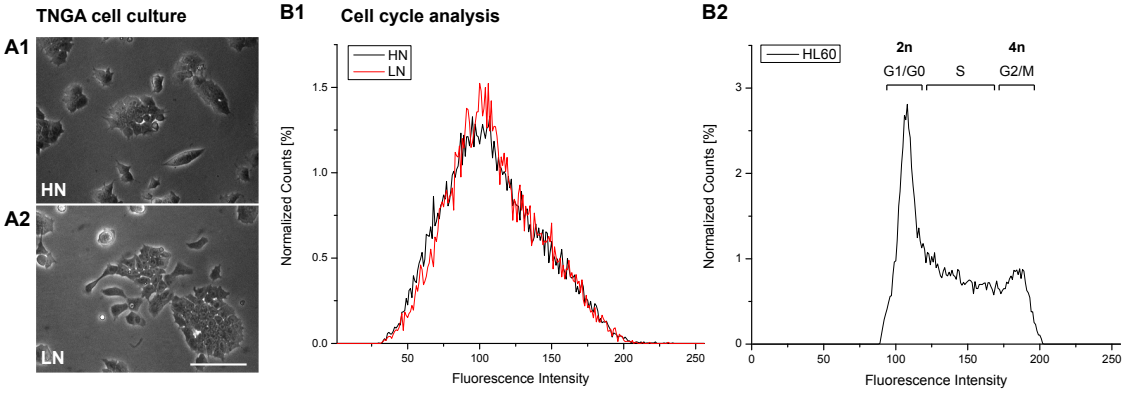

Figure 3.6. – Cell morphology and cell cycle analysis. Panel (A) Representative images of sorted HN and LN clutures after 24 h of incubation. Scale bar 100 µm. (B) Cell cycle analysis of TNGA (B1) and HL60 (B2) cells. Cultured cells were stained with a DNA-specific dye and the DNA content of single cells was analyzed using flow cytometry (fluorescence intensity, x-axis). The *eGFP*-reporter gene allowed easy discrimination between HN and LN cells. For the plot shown 2 replicates were averaged. (B2) Cell cycle analysis of HL60 cells. HL-60 cells proliferate slower than ES cells and show a bimodal distribution with a G1/0-phase peak, a peak with mitotic/G2-phase cells and cells with intermediate DNA content that are in S-phase. Relative DNA-amounts are indicated.

To investigate if any changes in the cellular or nuclear size or the ratio between these two parameters occurred in correlation with Nanog expression, I developed a protocol to measure cellular and nuclear sizes simultaneously in suspended live cells. Pilot studies revealed that fixation changed the sizes of the cells considerably and so I used a live cell staining and imaging protocol (fig. 3.7 A). From the projected cellular or nuclear area, the respective radii were calculated based on the approximation that trypsinized cells and nuclei are spherical objects (fig. 3.7 B). Mean cell radii were calculated as 6.09 ± 0.16 µm and 6.08 ± 0.12 µm for HN and LN cells, respectively. The corresponding nuclear radii were 4.80 ± 0.02 µm and 4.78 ± 0.05 µm, respectively. Statistical analysis showed that there were no significant differences. The calculated ratio of nuclear to cytoplasmic volume was close to ∼0.49 for both cell populations (fig. 3.7 C).

Reports in the literature describe that the disruption of cytoskeletal filaments can have dramatic effects on the nuclear size in attached cells [Mazumder and Shivashankar 2010]. F-actin applies tensile forces on the nucleus and its disruption with cytoD leads to nuclear shrinking (ca. −30 %) while MTs apply pushing forces and their disruption with nocodazole leads to nuclear swelling (ca. +20 %) [Mazumder and Shivashankar 2010]. When I treated cells with cytoD or nocodazole and measured nuclear and cellular sizes, I did not find these effects in trypsinized cells. While cell sizes stayed almost constant, slight changes in nuclear size led to a small increase in the N/C-ratio of cytoD treated cells (+3.9 % for HN and +2.5 % for LN cells). For nocodazole treatment I measured a small decrease of the N/C-ratio (HN: −5.9 %, LN: −5.4 %).

I noted, however, that the nuclei of trypsinized cells projected a much smaller area than nuclei

inside cells in the attached state (compare figs. 3.4 C/D and 3.7). This was probably partly due to the more rounded shape in the suspended state as opposed to a more flattened shape in attached cells. Additionally, the lack of tensile forces that depend on matrix-attachment could lead to a relative shrinking of nuclei. The fact that nuclei look much more wrinkled in suspended cells compared to a smooth outline in attached cells supports this hypothesis.

Taken together, it was ruled out that differences in cell morphology or proliferation speed caused the observed changes in cell mechanics that correlate with Nanog expression. Furthermore, the nucleus takes up around 50 % of the total cell volume in TNGA cells; therefore, I hypothesized that the nucleus could be responsible for the observed differences in whole cell mechanics.

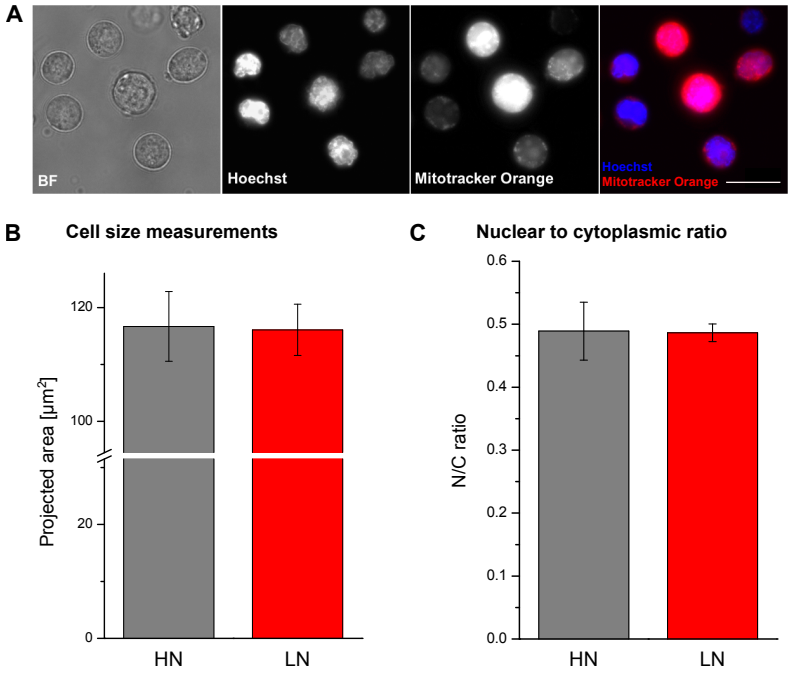

Figure 3.7. – Analysis of cellular and nuclear size. (A) Representative images of the stains that were used for cell size analysis. Cells were incubated with the live cell dyes Hoechst 33342 for DNA and Mitotracker Orange for the whole cells and imaged immediately. Scale bar 20 µm. (B) Projected cell area for HN and LN cells. Mean ± SD from two replicates with at least 100 cells each. (C) Volumes of cells and nuclei were calculated from the projected areas and the proportion of the nucleus from the whole cell (N/C ratio) is presented for HN and LN cells. The average from 2 replicates ± SD is shown.

3.4. Measurement of Nuclear Mechanics

Several techniques for the investigation of nuclear mechanics are described in the literature. In preliminary studies, atomic force microscopy was used to probe intact TNGA cells and their nuclei (K. Franze and K. Chalut). These experiments did not yield conclusive results and so we searched for other ways to measure mechanical parameters of cell nuclei. The first approach was to isolate nuclei from intact mES cells and perform rheological studies on those isolated nuclei. To this aim, I developed a protocol to extract nuclei from mouse embryonic stem cells (see appendix A). In optical stretching, the forces on cells depend on a change in the refractive index from the surrounding medium to the cell. The nucleus has an even higher refractive index than cytoplasm [Brunsting and Mullaney 1974] and so OS measurements could in principle be possible. We performed optical stretching experiments on isolated nuclei, but we found that heat effects dominated the behavior of isolated nuclei in OS measurements. These effects are caused by local heating (ca. 10–20 °C) due to the high intensity of the laser light and so this strategy was not successful to measure nuclear mechanics (see appendix A). AFM measurements were performed for isolated nuclei by K. Franze but did not show significant differences between HN and LN nuclei.

We hypothesized that, if nuclear mechanics affected whole cell mechanics, they would deform within intact cells in OS measurements. To investigate this assumption, we stained cells with a DNA-specific live cell dye (Hoechst 33342) and performed stretching experiments where we imaged the blue fluorescence of the DNA-dye instead of phase contrast. Supporting our hypothesis, we found that nuclei within intact cells did stretch along the laser axis. Strikingly, we found that the nuclei of LN cells deformed to a significantly higher degree (+31.7 %) than nuclei of HN cells (fig. 3.8). The response of the nuclei to the applied step-stress was different in its nature to that of the cells (compare figs. 3.8 A and 3.1 A). The nuclei showed a more elastic response and contracted slightly during the stretching period after reaching their peak deformation. In contrast to the cells, the nuclei almost completely relaxed to their initial size after 3 sec of the recovery period. However, the magnitude of the deformation of nuclei was comparable to that of cells (ca. 25 % less peak strain, fig. 3.8).

To investigate the behavior of nuclei when the whole cell is deformed by a considerable higher degree and to investigate the dependence of nuclear deformation on cytoskeletal structures, we treated the cells with cytochalasin D and measured nuclear deformation. We found an 1.25-fold increase in nuclear peak strain on average for HN and LN cells (fig. 3.8 C and D) in contrast to a 2.7-fold increase we found in whole cell measurements (fig. 3.2). When treated with cytoD, we also observed a high percentage of nuclei that rotated during the measurements, possibly hinting

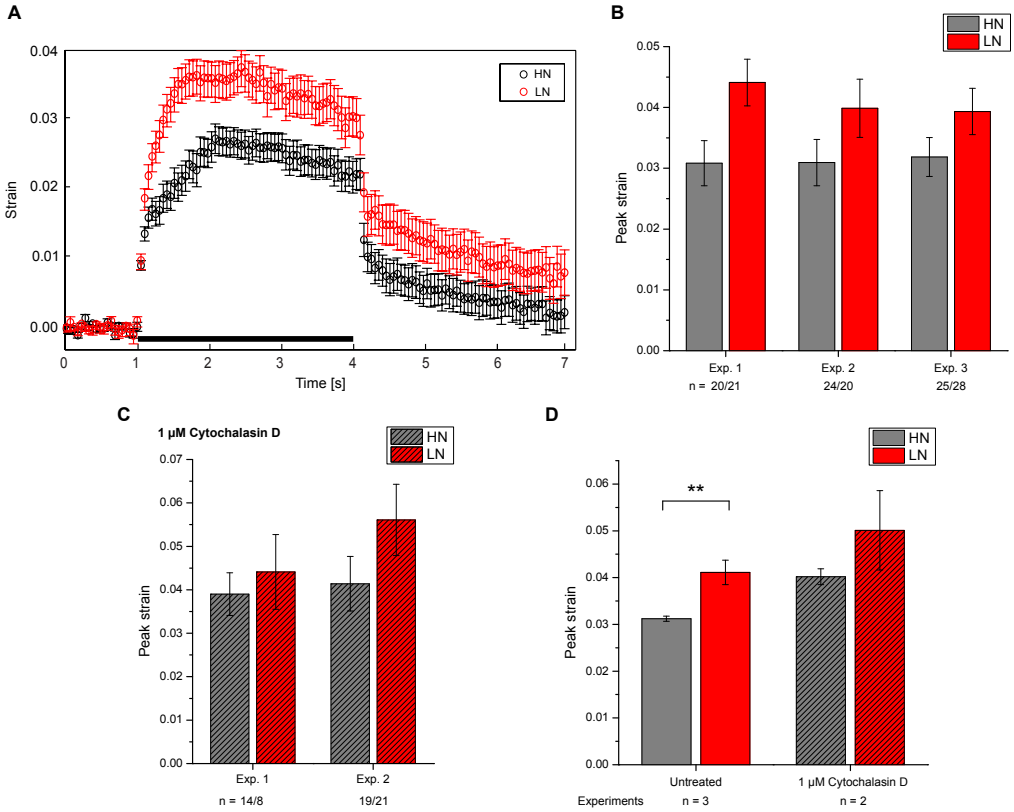

Figure 3.8. – Deformability measurements of nuclei inside living cells. (A) Relative deformation of Hoechst-stained nuclei along the laser-axis in optical stretcher measurements as a function of time. The red bar indicates when the step-stress is applied by increasing the laser power. Mean values for each timepoint ± SEM. (B) Overview over the average peak strains from 3 independent experiments. Means ± SEM. (C) Equivalent experiments with 1 µm cytochalasin D treatment. (D) Summary of the results for nuclear deformability of HN and LN cells with and without cytochalasin D treatment. Means of the individual experiments were averaged and are presented with SD as errors.

at a disruption of nuclear to cytoplasmatic connections. We concluded that the actin cytoskeleton has only minor influences on nuclear deformation but is crucially involved in mechanically connecting the nucleus with the cell membrane; we then investigated what structural elements would dominate nuclear mechanics of mES cells.

The intermediate filaments lamin A/C were shown to have a major impact on nuclear rheology in knock-down studies [Pajerowski et al. 2007]. Expression of lamin A/C was correlated with a stiffening of the nucleus. However, these structural proteins are not expressed in pluripotent stem cells and only emerge in the course of differentiation [Constantinescu et al. 2006].

We therefore hypothesized that the chromatin itself could be responsible for the changes in cell and nuclear mechanics we observed. We suspected the global state of chromatin condensation is responsible for these differences. To test our hypothesis, we influenced chromatin compaction on a global level using the histone deacetylase (HDAC) inhibitor trichostatin A (TSA) to decondense chromatin [Yoshida et al. 1990; Tóth et al. 2004]. To globally condense chromatin we used divalent cations ($MgCl_2$+$CaCl_2$). Interestingly, we found that divalent cations caused a significant decrease while TSA caused a significant increase in nuclear deformability (fig. 3.9 A and B). Assuming that nuclear mechanics influenced whole cell mechanics in ES cells, we also measured cellular deformability for $MgCl_2$+$CaCl_2$ and TSA treated cells (fig. 3.9 C and D). Like for the nuclei, divalent salts caused stiffening of the cells while TSA caused a softening of the cells. The effects were of comparable magnitude in cells and nuclei.

It has to be noted, however, that Mg^{2+} and Ca^{2+} ions are important in many other cell functions and singalling pathways as well. Unspecific effects apart from chromatin condensation could contribute to nuclear and cellular stiffening with divalent cation treatments. Therefore, an alternative method to condense chromatin in a more specific way is desirable as an additional control.

With these experiments we showed that the state of chromatin compaction influences nuclear as well as whole cell mechanics. Therefore, we investigated whether chromatin compaction on a global state changed with the downregulation of Nanog in LN cells.

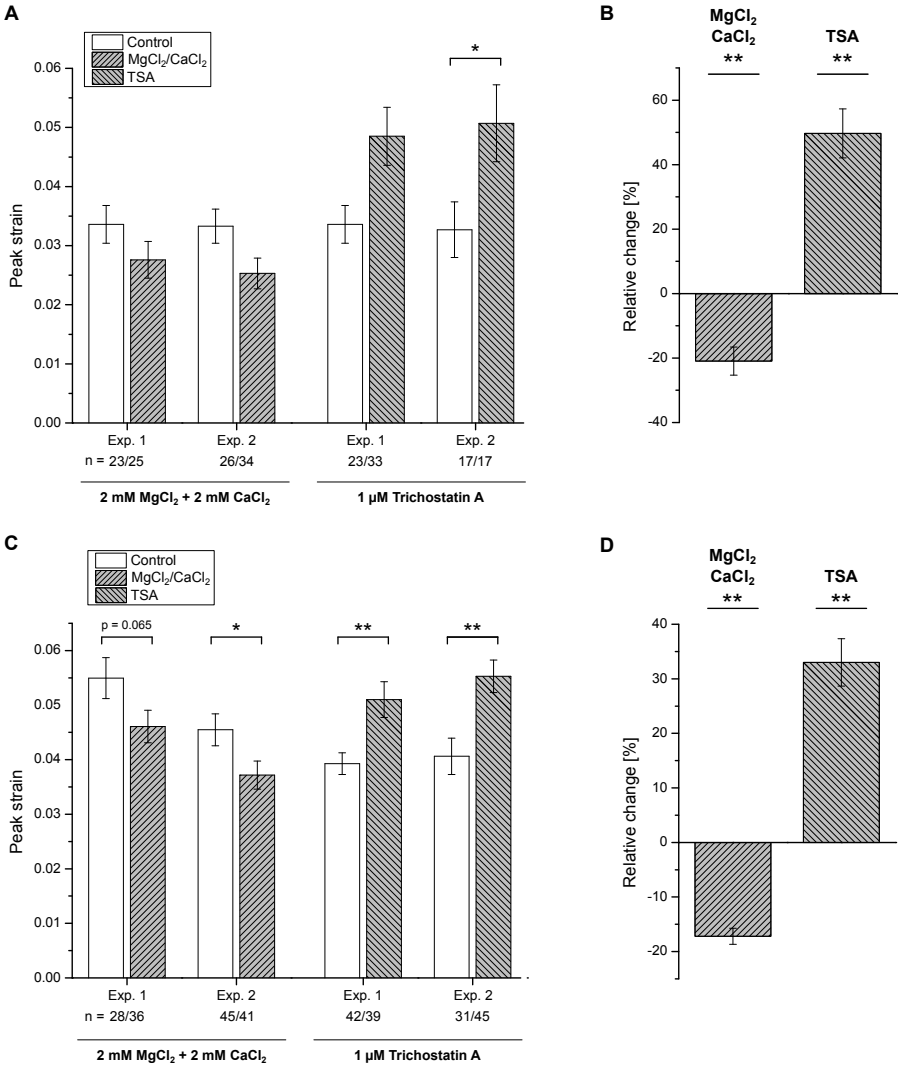

Figure 3.9. – Deformability measurements of nuclei (A+B) and cells (C+D) treated with divalent cations or trichostatin A. (A) Mean peak strain values (± SEM) for nuclei of 2 independent experiments when cells were treated with $MgCl_2$+$CaCl_2$ or TSA. For these experiments unsorted TNGA populations were used. (B) Average relative difference to the nuclear deformability of the corresponding control population for 2 experiments each. Error bars are SD. (C) Results for peak strain measurements of cells in experiments that were performed in the same way as for nuclei in (A). (D) Equivalent to (B) for whole cell measurements.

3.5. Histone H2B Dynamics Measured Using FRAP

Histone H2B is one of the core histone proteins that form the protein part of nucleosomes. While the histones H3 and H4 were observed to be stably bound to chromatin, a degree of dynamic exchange of histone H2B was observed using fluorescence recovery after photobleaching for tagged histones [Kimura and Cook 2001]. For histone H2B in HeLa cells it was reported that a small fraction of the protein (3 %) diffuses rapidly within seconds, 40 % of the bleached fluorescence recovered at slower rates ($t_{1/2} = 130$ min) while the rest of the protein did not diffuse [Kimura and Cook 2001]. However, more recent studies showed that in mES cells, there is a fast initial recovery to 30–50 % of the pre-bleach signal intensity with a plateau after around 200 sec [Meshorer et al. 2006; Bhattacharya et al. 2009]. Similar recovery kinetics have been reported for histone H3 [Meshorer et al. 2006]. These studies also suggested a correlation of histone dynamics with differentiation and chromatin compaction.

To measure histone dynamics in TNGA cells, I transiently transfected cells with an RFP-tagged histone H2B and performed fluorescence recovery after photobleaching experiments. The transfected protein was exclusively located in nucleus (fig. 3.10 A), cells looked viable and transfected cells were observed to divide. Initial experiments showed that the tag-protein was not ideal in its photo-bleaching properties. I found that TagRFP had a dark state that could be observed when several images were taken in short sequence (e. g. in the two left-most images in 3.10 C) until an equilibrium state of fluorescence intensity was reached. Furthermore, the protein bleached very easily during image acquisition and imaging quality was a problem, especially when the expression levels of the protein were low. The nuclei of TNGA cells showed considerable movement and rotations and therefore I recorded z-stacks in pilot studies over long time-scales. These studies revealed that after 60 min a large fraction of the bleached fluorescence recovered (fig. 3.10 B). Careful adjustment of the bleaching and imaging settings finally allowed us to quantify recovery after bleaching a certain area of the nucleus (fig. 3.10 D and E). For initial quantitative measurements, I bleached a 4 µm thick bar across the middle part of a nucleus and observed the recovery over 30 min (fig. 3.10 C and D). After normalization of the signal so that the relative intensity of the bleached region was set to 0 in the first post-bleach frame, I saw an initial drop in relative signal intensity. This was due to the described dark-state properties of the protein (fast frame-sequences). I found a recovery of around 15 % relative to the pre-bleach value after 30 min for both HN and LN cells. LN cells recovered slightly but non-significantly faster than HN cells. Control measurements on fixed cells, where diffusion is not possible, were done to rule out that the observed recovery was an artifact (3.10 D, blue curve). The control measurement shows that the normalization underestimates the real recovery slightly as the relative signal drops while it

should stay constant.

As the recovery seemed to show an almost linear behavior and cell movements complicate long measurements, I decided to observe only a 20 min period in following experiments (fig. 3.10 E). Problems with the dark-state properties of the cells could be solved by modifying the imaging sequence. However, I could not reproduce the faster recovery for LN cells.

To investigate whether there was an initial fast recovery as reported in other studies, I also did measurements with a 79 ms time-resolution for a small part of the nucleus. I recorded a 20.5x2.5 µm strip across the nucleus and a central spot was bleached (fig. 3.10 F). 200 to 300 pre-bleach frames were recorded till an equilibrium state between the fluorescent and a dark state of the protein was reached (not shown). No recovery in the first 16 sec was observed.

Further optimization of the transfection protocol, the observation of a 10 min time-period and the bleaching of a round spot in the middle of the cell led to better results (fig. 3.11). We observed faster recovery kinetics using this setup than with the strategies taken in previous experiments. Strikingly, in four independent experiments, we found that cells with low Nanog levels showed faster recovery kinetics than HN cells (fig 3.11 A). The combined data showed a highly significant difference at the end of the observed recovery period. To find out whether a forced chromatin decondensation also led to faster recovery kinetics we treated HN cells with TSA. The recovery was significantly faster in TSA-treated HN cells than in untreated HN control cells and also slightly faster than in LN cells from the same experiment (fig. 3.11 B).

These data show that histone H2B diffuses faster in LN cells than in HN cells, suggesting a more decondensed chromatin in LN cells. Furthermore, TSA-treatment led to faster recovery indicating that chromatin decondensation leads to higher histone mobility, which is in good agreement with the literature [Meshorer et al. 2006; Bhattacharya et al. 2009].

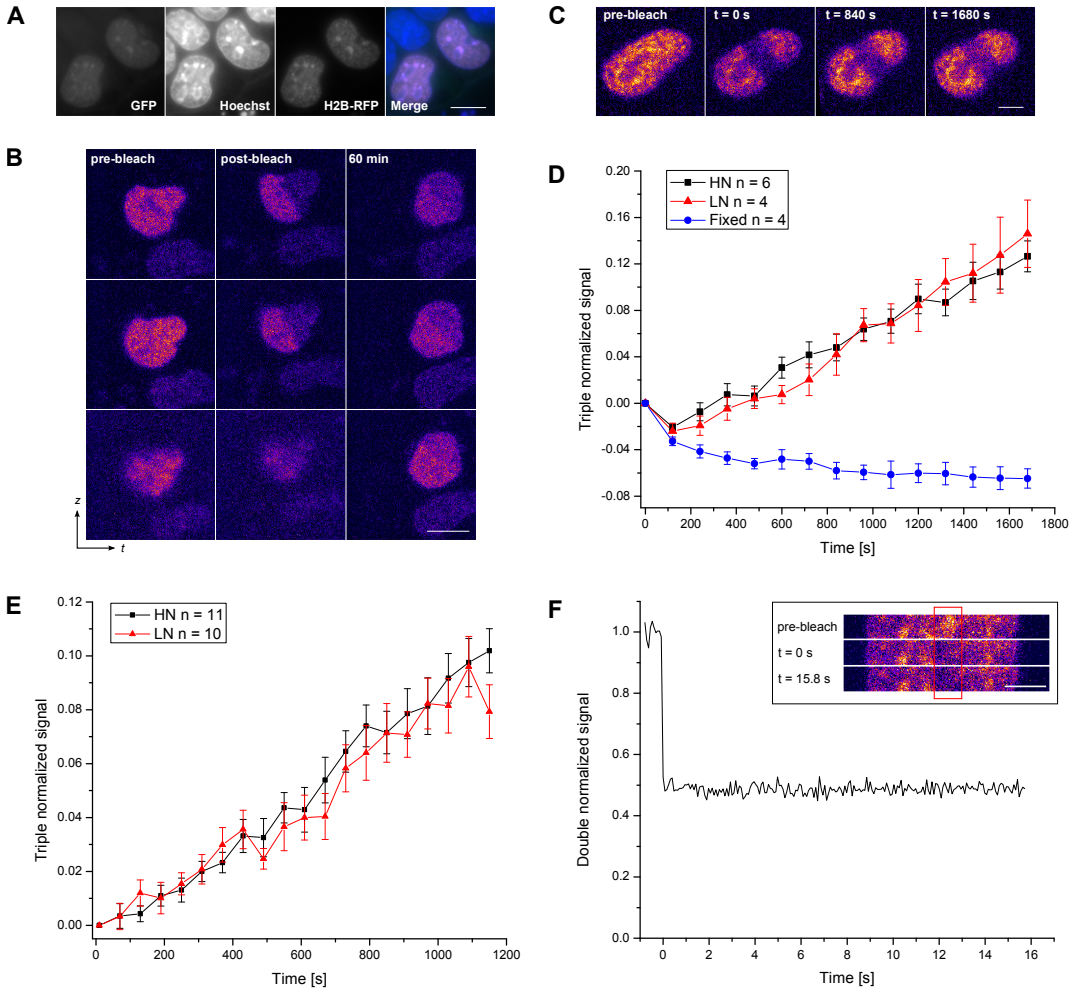

Figure 3.10. – Fluorescence recovery after photobleaching for histone H2B-RFP. (A) Epi-fluorescence images of TNGA cells transfected with H2B-RFP that were fixed and counter-stained with Hoechst 33342. H2B-RFP is exclusively located in the nucleus. Scale bar 10 µm. (B) 3 slices (2 µm apart) of confocal z-stacks that were recorded before and after bleaching as well as 60 min later. The RFP-channel of a nucleus of which approximately half the area was bleached is shown. No correction for cell movement was done for this panel and movements of the cell in x, y and z as well as changes in nuclear shape can be observed. Images are false-colored for better contrast. Scale bar 10 µm. (C) illustrates how measurements for plots (D) and (E) were performed by bleaching a 4 µm thick bar across a nucleus. Scale bar 5 µm. (D) FRAP experiments for HN and LN cells as well as for fixed cells over 30 min with one frame every 120 sec. Individual curves were normalized to the pre-bleach value, corrected for acquisition bleaching and normalized to the first post-bleach value. (E) Similar experimental conditions as in (D) but with a higher resolution in time. The first post-bleach frame was taken 10 sec after the bleach pulse. (F) FRAP experiment with 79 ms time resolution for a small part of the nucleus over a short period. The curve shows the double normalized signal averaged over 4 measurements (prebleach value = 1). The inset shows the recorded area of one measurement. The bleached area is highlighted by the red rectangle. Scale bar 5 µm.

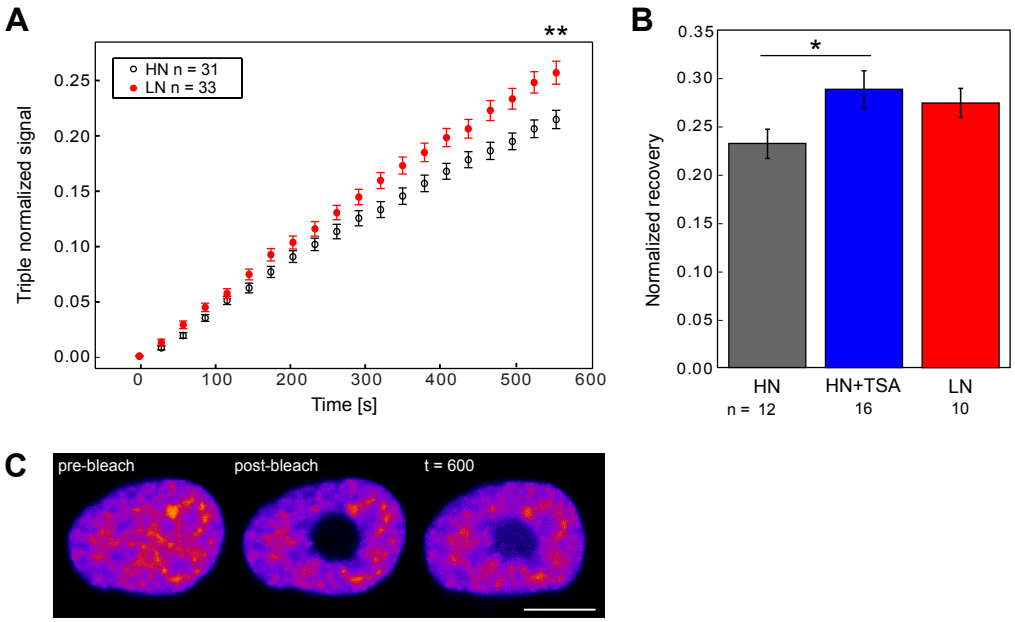

Figure 3.11. – FRAP experiments with a circular bleach area over 10 min. (A) Triple normalized recovery of H2B-RFP for HN and LN cells. The data were taken in four independent experiments. Mean ± SEM for each time-point. (B) Comparison of the normalized total recovery after 10 min of HN cells, HN cells treated with 300 nM TSA for 2 h and LN cells from a single experiment. Error bars indicate SEM. (C) false-colored images of a representative nucleus in a FRAP experiment. Scale bar 5 µm.

3.6. Quantitative Analysis of the HP1α-Distribution in Nuclei

To validate the results from FRAP-experiments that implicated a less condensed chromatin state in the differentiation-prone LN cells, I used an independent method to analyze chromatin compaction. HP1α locates to heterochromatic foci of chromatin; these foci get smaller and more distinct, and their number per nucleus has been shown to increase in the course of differentiation (fig. 1.2 C, [Meshorer et al. 2006]). To quantify the distribution of HP1α in mES cells, the cells were immunostained using an HP1α specific anti-body (fig. 3.12 A, B, E and F). I consequently imaged the cells and analyzed the fractal dimension D_F of the HP1α distribution for nuclei individually. The D_F is a way for the quantification of the complexity of a given pattern (see also section 2.8). In the case I analyzed, a high D_F means a more diffuse staining pattern for HP1α [Tóth et al. 2004]. Therefore, nuclei with distinct foci have a low D_F while nuclei with a dispersed staining pattern have a high D_F (fig. 3.12 A, B).

When I compared the fractal dimension of single HN- and LN-nuclei, I found that the distribution of D_F values was shifted to higher values for LN cells compared to HN cells (fig. 3.12 C). The mean fractal dimension was significantly increased by 3.27 % (±0.578 SD) on average from HN to LN cells in two independent experiments. Differences in the absolute D_F-values in the two experiments were most probably due to slight differences in the imaging settings and deviations in the staining intensity that can influence the analysis. The overall staining intensities were also compared between HN and LN cells and no differences were found.

I further investigated whether the divalent cation- and TSA-treatment we used for chromatin compaction and decompaction, respectively, would influence the HP1α-distribution. I did not find a decrease in D_F when the cells were treated with $MgCl_2$+$CaCl_2$. However, a significantly higher average signal intensity was observed. Divalent salts lead to a stronger binding of structural proteins such as histones to the DNA and to increased nucleosome-to-nucleosome interactions [de Frutos et al. 2001]. Therefore, I speculated that divalent cations led to a genome-wide chromatin compaction without changing the HP1α-distribution. Furthermore, I did not keep the divalent salts on the cells during washing and fixation and so reversible changes might not be detected using this protocol. However, treatment with the HDAC-inhibitor TSA did lead to a highly significant increase in D_F as compared to an untreated control population (fig. 3.12 E-H). The average increase in two experiments was 6.85 % (±0.996 SD). For TSA-treated cells, no increase in signal intensity was observed. While a difference in the staining pattern was not easy to see by eye for HN versus LN cells, a more diffuse staining pattern for HP1α after TSA treatment

was very obvious compared to a control population. Therefore, D_F-analysis provides a valuable tool to quantify such patterns.

Taken together, both the FRAP-experiments and the HP1α-distribution analysis suggested a significant decondensation of chromatin in the transition from HN to LN in mES cells. Chromatin was shown to be more condensed on a global scale in the stable pluripotent HN state. TSA-treatment was used to demonstrate that we could detect changes in chromatin decondensation with FRAP for a tagged histone and D_F-analysis of HP1α-patterns.

Note: Follow-up studies by K. Chalut on chromatin compaction using immunohistochemistry stainings for repressive H3K9me3-marks and H3K27me3-marks further strengthened our findings that chromatin is more compact in HN cells. As for HP1α, the distribution of H3K9me3-foci was found more diffuse in LN cells. The H3K27me3 was smooth for both cell populations, however signal quantification showed a strong correlation with Nanog expression, indicating that there are overall more repressive marks in HN cells than in LN cells. Both histone modifications are implicated in heterochromatin formation, stabilization and gene silencing [Ringrose et al. 2004; Bernstein et al. 2006; Mikkelsen et al. 2007]

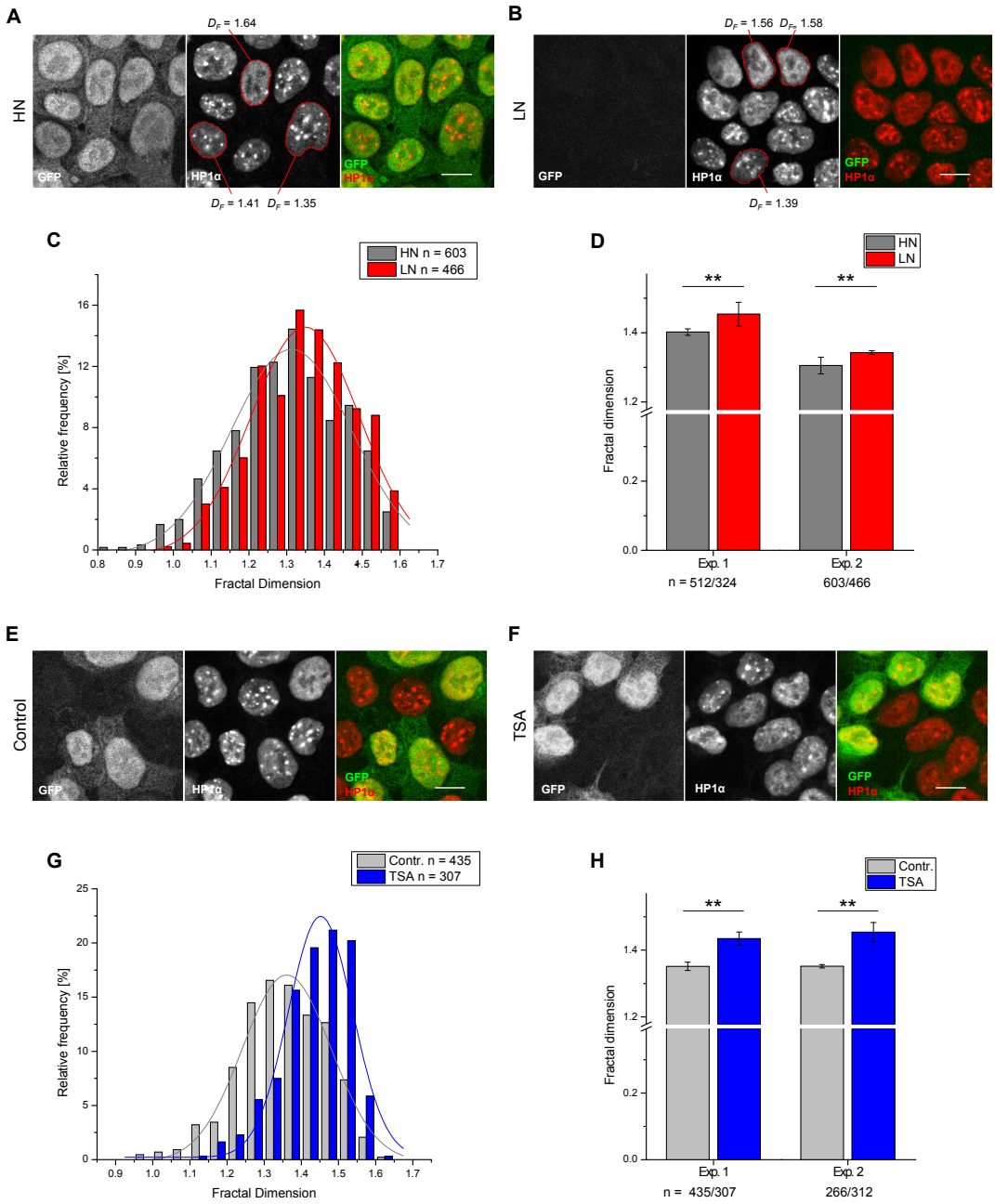

Figure 3.12. – Quantitative analysis of HP1α-distribution. (A) and (B) Confocal microscopy images of HN and LN populations that were stained for the heterochromatin protein HP1α. Single nuclei are highlighted in red and the fractal dimension D_F is indicated. Scale bars 10 µm. (C) Histogram of the relative frequency of D_F-values in one of the experiments where HN and LN cells were compared. Data were fitted to a gaussian distribution to obtain the curves presented; histogram bins are in steps of 0.05. (D) Mean D_F for HN and LN populations in 2 independent experiments. The mean values of all replicates (Exp. 1: 2 replicates, Exp. 2: 4/5 replicates) of one experiment were averaged and are presented with SD as errors. (E-H) Equivalent experiments as in (A-D) were performed for TNGA control populations versus populations treated with 400 nM trichostatin A for 2 h (3/2 replicates in Exp. 1/2)). Scale bars in panels (E) and (F) are 10 µm.

4. Discussion

4.1. Cellular and Nuclear Mechanics in Pluripotent Stem Cells

Heterogeneous Cell Mechanics in Pluripotent ES Cells

In this study, we present evidence that biophysical properties of pluripotent mouse embryonic stem cells change as a function of their differentiation potential. We found that cells expressing low levels of Nanog, which renders them differentiation-prone [Chambers et al. 2007; Kalmar et al. 2009], show a higher compliance in optical stretcher measurements than cells expressing high Nanog levels. This result is surprising as there are a number of studies that used atomic force microscopy showing that mES cells get stiffer when they differentiate [Pillarisetti et al. 2011; Chowdhury et al. 2010]. However, these studies investigated pluripotent ES cell populations in comparison with cell populations in which differentiation was induced by either LIF-withdrawal alone or in parallel with chemical induction of differentiation for at least 48 h. In contrast to that, we investigated subtle changes in pluripotent mES cells that occur in correlation with Nanog expression before lineage commitment. Also, AFM probes mechanical properties locally whereas optical stretching probes whole cell mechanics [Guck et al. 2010]. Pillarisetti et al. [2011] report a 2.2-fold stiffening of ES cells after 6 days of LIF-withdrawal while we measured a decrease of the stiffness (inverse of compliance) of 14.5 % for LN versus HN cells. The stiffening of cells in the course of differentiation was explained by the emergence of a more defined cytoskeleton [Pillarisetti et al. 2011; Chowdhury et al. 2010]. In particular, increased cell-spreading and actin-myosin II dependent contractility was observed [Chowdhury et al. 2010]. Interestingly, the authors also claim that mES cells have a high nuclear-to-cytoplasmic ratio and that changes in nuclear structure such as the expression of the nuclear lamina proteins lamin A/C could contribute to overall cell mechanics [Pillarisetti et al. 2011].

In our investigation of the role of the actin- and MT-cytoskeleton in stem cell mechanics we ruled out the possibility that these filamental networks account for the mechanical differences in correlation with Nanog expression. Mechanical differences between the two states persisted upon

disruption of f-actin using cytochalsin D, which also caused a dramatic softening of cells. Our data on the role of f-actin are in good agreement with the literature where the actin-cytoskeleton was shown to be the major determinant for the response of cells to externally applied forces [Wakatsuki et al. 2001; Petersen et al. 1982] and that in particular the subcortical actin network is crucial to the response of a cell to mechanical stress in the optical stretcher [Lautenschläger 2011; Ananthakrishnan et al. 2006]. Disruption of MTs using nocodazole caused a slight overall softening of the cells. The results varied among individual experiments and further experiments, possibly using other drugs, are needed to make well-informed statements about the role of MTs. Nevertheless, on average the LN cells were softer than HN cells also with nocodazole treatment. Previous studies on the role of MTs in optical stretching experiments for the human NB4 cell line and mouse fibroblasts (3T3 cell line) also report that MTs have only minor influence on the peak deformation of cells [Lautenschläger 2011].

IFs were shown to play only a minor role for cell elasticity in small deformations [Janmey et al. 1991; Wang 1998]; therefore we did not investigate the role of IFs in ES mechanics.

F-actin and microtubule stainings of attached TNGA cells revealed that both types of filaments mainly align close to the cortex of the cells. In this context, it is noteworthy that mES cells grow in densely packed colonies where there is not much space between the nuclei of adjacent cells. Actin filaments are bundled in focal adhesions where cells attach to the substrate and f-actin as well as MTs spread out more on the bottom and at the edges of colonies. Mouse ES cells do not attach easily to substrates, e. g. they do not adhere to glass surfaces and need gelatin-coated surfaces to grow. Thus, it is not surprising that we did not observe long and thick stress-fiber bundles that appear in cells that spread out more on substrates. Stainings presented in other studies show a similar structure of f-actin in mES cells [Pillarisetti et al. 2011].

Our stainings of trypsinized cells clearly show that the cortical actin is intact in the suspended state and that treatment with cytochalsin D completely disrupts the structure of the filaments. Although our study gives insight into the structure of the cytoskeleton in mES cells, the mechanical differences between HN and LN cells can not be explained by changes of the MT or actin cytoskeletal organization.

Contribution of Nuclear Mechanics

While the nuclear-to-cytoplasmic ratio is small in a fertilized egg, the relative amount of cytoplasm decreases in early embryonic development due to cleavage divisions where cells divide without growing in terms of volume [Wolpert et al. 2011]. In mES cells, which are derived from the inner cell mass, we measured a value for the N/C ratio of about 0.5 in the suspended state. In the attached state, they appear densely packed and the more spread out nucleus comprises a large

part of the cell in comparison to other attached cell types ([Pillarisetti et al. 2011], reviewed in [Dahl et al. 2008]). The nuclear volume was reported to decrease by about 50 % from pluripotent to differentiated cells [Niwa 2007]; we found no differences in the relative or absolute size of nuclei between the pluripotent HN and LN cells, however.

In the course of this study, we developed a method to measure nuclear mechanics in a comparative manner. We found that nuclei of LN cells deformed more than nuclei of HN cells. Also, forced decondensation of chromatin lead to a significant softening of nuclei. Treatment with divalent cations led to stiffening of nuclei. The same effects were observed when we measured whole cell mechanics for these conditions.

The approach we chose allowed a contact free probing of nuclei inside intact suspended cells. This is in contrast to other methods such as micropipette aspiration, microplate manipulation, atomic force microscopy or cellular strain experiments (reviewed in [Verstraeten and Lammerding 2008] and [Lammerding et al. 2007]), which involve physical contacts to the cells or nuclei, thereby deforming them often to an unphysiological degree. Also, the extraction of nuclei from cells involves the disruption of nuclear to cytoplasmatic bonds and nuclei are taken out of their physiological context. It has to be noted though, that our method is only applicable to cells in suspension which involves taking attached cells out of their regular cell culture environment.

To this point, we lack theoretical models that could be used to calculate rheological parameters of nuclei from our nuclei stretching data. Therefore, it is hard to compare our measurements quantitatively to other techniques. A better characterization of the method in the future will be needed and ideally, our results should be confirmed using another, well-established technique. So far it is not entirely clear what causes the deformation of the nuclei: One possibility is that connections from the cell membrane that mechanically link the nucleus and chromatin via the cytoskeleton and the LINC complex [Crisp et al. 2006] cause the deformation when optical forces are applied to the cell membrane. A second possibility is that the change in refractive index from the cytoplasm to the nucleus causes a momentum transfer to the nuclear membrane so that they deform within the cell. A considerable change in the refractive index from $n = \sim 1.37$ to ~ 1.39 from cytoplasm to nuclei has been reported (for other cell types) by Brunsting and Mullaney [1974]. These possibilities are not mutually exclusive, of course. F-actin disruption led to a 2.7-fold increase in cellular deformability but only a 1.25-fold increase in nuclear deformability. This implicates that nuclei do not only deform passively following whole cell deformation, but are stretched independently to some degree, which favors the second possibility.

It has been suggested previously that nuclear mechanics could contribute to the mechanical properties of ES cells due to the high nuclear-to-cytoplasmic ratio [Pillarisetti et al. 2011]. This assumption is further backed up by studies that showed that the nucleus is 3–10 times stiffer than

the surrounding cytoplasm [Guilak et al. 2000; Caille et al. 2002]. Structural elements of nuclei that determine their mechanical properties could therefore also influence whole cell mechanics. Micropipette aspiration studies showed that the expression of lamin A/C led to an approximately 2-fold stiffening of nuclei when human hematopoietic stem cells that lack lamin A/C and primary fibroblasts were compared [Pajerowski et al. 2007]. RNA-interference studies where Lamin A/C was knocked down gave similar results for epithelial cells [Pajerowski et al. 2007]. These and other authors also suggested a dependence of nuclear mechanics not only on the lamin scaffold, but also on chromatin organization [Mazumder and Shivashankar 2007, 2010].

In our study, we demonstrated that the rheological properties of mES nuclei that are stretched within living cells critically depend on chromatin compaction. We showed that chromatin decondensation by inhibition of HDACs caused a softening of nuclei while divalent cations added to the medium rendered nuclei stiffer. These findings are in line with our expectations that chromatin compaction changes nuclear mechanics. Studies on single chromatin fibers (reviewed in [Schiessel 2003]), extracted nuclei [Dahl et al. 2005] and laser ablation studies on eu- and heterochromatic areas [Mazumder and Shivashankar 2007, 2010] suggest that condensed chromatin is stiffer and more resistant to mechanical deformations. Both the protein-protein interactions of histones and other DNA-binding proteins [Mazumder et al. 2008] as well as the DNA itself [Dahl et al. 2005] were shown to contribute to the structural integrity of nuclei. As lamin expression is absent in ES cells [Constantinescu et al. 2006], we therefore conclude that changes in chromatin compaction are responsible for the changes in nuclear mechanics and in consequence also affect whole cell mechanics of mES cells.

Our finding that nuclei deform within intact cells and that nuclear mechanics contributes to whole cell mechanics in OS measurements of suspended cells brings up new possibilities for the use of optical stretching devices. Measurements of attached cells requires a suspension step which can lead to artifacts and cell blebbing after trypsinization [Maloney et al. 2010], which is certainly a weakness of the method. However, it provides unique possibilities of contact-free cell mechanics measurements of cells that proliferate in suspension. For example in the maturation of granulocytes, besides changes in nuclear morphology, the fraction that the nucleus occupies from the whole cell volume changes from ~ 0.83 in myeloblasts to ~ 0.33 in neutrophilic segmented cells [Heiserman 2004]. Cell mechanics has previously been shown to change in the course of differentiation in acute promyelocytic leukemia cells [Lautenschläger et al. 2009] and nuclear stretching measurements could shed new light on the role of nuclear mechanics in blood cell differentiation.

Also, changes in nuclear morphology and stiffness were implicated in cancer and metastasis potential (reviewed in [Dahl et al. 2008]). The optical stretcher has been successfully used before

in discriminating normal cells from cancer cells [Remmerbach et al. 2009] and probing nuclear mechanics could provide additional possibilities in this context.

4.2. Chromatin Organization in ES Cells and Differentiation

Our findings on chromatin organization in TNGA cells go well with the above-mentioned assumptions of the influence of chromatin on nuclear mechanics. Using two independent techniques, we showed a more decondensed chromatin organization in LN cells than in HN cells. In fluorescence recovery after photobleaching experiments for an RFP-tagged histone H2B, we found faster recovery kinetics for LN cells than for HN cells. Reports in the literature are contradictory on the exact recovery kinetics of histone H2B in pluripotent stem cells [Meshorer et al. 2006; Bhattacharya et al. 2009]. The authors of both studies agree, however, that differentiated cells show only very slow recovery of bleached areas as compared to ES cells, which is in good agreement with other studies on H2B dynamics in differentiated cells [Kimura and Cook 2001].

In addition to FRAP experiments, we quantitatively analyzed the distribution of the heterochromatin associated protein HP1α in fixed cells using a fractal dimension formalism. As with the FRAP method, our results indicate a globally more condensed chromatin state in HN cells as compared to LN cells. Similar methodological approaches have been demonstrated before [Tóth et al. 2004; Chalut et al. 2011] and a higher fractal dimension, as we found it in LN and TSA-treated cells, was correlated with decondensed chromatin. Studies on the distribution pattern of HP1α report that HP1α foci become more defined in differentiated cells and an increase in the number of foci while the average area decreases [Meshorer et al. 2006]. We found the fractal dimension approach to be particularly useful to measure subtle changes that occur in the HN to LN transition that are hard to quantify by counting individual heterochromatin foci or measuring their area, especially because they are often undefined in ES cells.

The regulation of epigenetic modifications and their implications in gene regulation in differentiation and development was subject of intense research in the last decade (reviewed in [Meshorer and Misteli 2006; Silva and Smith 2008; Orkin and Hochedlinger 2011; Fisher and Fisher 2011]). A number of studies has provided evidence that chromatin is generally less condensed in pluripotent cells while large scale heterochromatinization and gene silencing occurs in the course of differentiation [Meshorer et al. 2006; Bhattacharya et al. 2009]. Several models of how chromatin state could be involved in regulating pluripotency have been proposed [Meshorer and Misteli 2006], amongst which the promiscuous transcription (PT) and the early transcription competence marks (ETCM) models found most support in the recent years. The PT model assumes that, besides highly expressed housekeeping and pluripotency associated genes, large parts of the

genome are transcribed at low levels in ES cells. Evidence for this model was presented e. g. by Efroni et al. [2008] who reported that ES cells were transcriptionally hyperactive and that many coding and non-coding regions were expressed at low levels. The ETCM model proposes that lineage-specific genes are epigenetically marked for activity while being kept inactive in the pluripotent state. Studies that report the existence of so-called 'bivalent domains' of chromatin modifications support this model [Bernstein et al. 2006; Mikkelsen et al. 2007]. Bivalent domains feature both activating (H3K4me3) and repressive (H3K27me3) histone marks. Many of these domains coincide with the loci of developmentally important transcription factor genes.

However, the assumption that chromatin is generally euchromatic in pluripotent cells and large parts get heterochromatinized in differentiated cells is a simplification: various findings demonstrate that the key pluripotency transcriptional network Sox2-Oct4-Nanog plays a crucial role in regulating chromatin condensation, as discussed in section 1.1.3. Our data suggest that the balance between global chromatin condensation and decondensation is shifted in the HN to LN transition. This result fits well into the picture of the described connections between the SON-network and chromatin remodeling regulation. We propose that in a stable pluripotent state (HN), chromatin is packed more condensed on a genome-wide level than in differentiation-prone LN cells. This finding is surprising in the light of the traditional view that the relative amount of heterochromatin goes up form the pluripotent to the differentiated state [Meshorer and Misteli 2006].

Relating our findings to the models presented above, one could speculate, that in the HN state, transcription of lineage specific genes is still tightly controlled, representing the ETCM model. In the LN state, chromatin is decondensed, rendering genes slightly more accessible to the transcriptional machinery. Low-level transcription of many lineage specific genes, like proposed in the PT model, makes cells more prone to differentiate in this state.

Further research should be directed to the investigation of a mechanistic connection between Nanog expression and chromatin remodeling. This can lead to a better understanding of how transcription factor networks, epigenetic mechanisms and transcriptional control contribute to the regulation of pluripotency.

4.3. Implications and Outlook

It will be interesting to test the *in vivo* relevance of our findings that Nanog expression, chromatin condensation and whole cell mechanics are interconnected. Sorting processes in early embryonic development where the extraembryonic tissues trophectoderm (TE) and the primitive endoderm (PE) segregate from apparently uniform cells in the morula are not well understood, yet. In both

TE and PE Nanog is down-regulated while its expression remains high in the epiblast (EPI) [Plusa et al. 2008]. Interestingly though, the inner cell mass (ICM) in the early blastocyst, which segregates into PE and EPI was shown to be a heterogeneous population of cells expressing different levels of developmentally important TFs (e. g. Nanog, Gata6) [Chazaud et al. 2006; Plusa et al. 2008]. This is reminiscent of the heterogeneous Nanog expression of *in vitro* cultured mES cells. A combination of not fully understood sorting processes then leads to the separation of EPI and PE cells in the late blastocyst. Both passive processes such as the relative position to the blastocyst cavity as well as active cell migration were proposed as contributing factors to efficient sorting ([Plusa et al. 2008; Meilhac et al. 2009], reviewed in [Yamanaka et al. 2006; Zernicka-Goetz et al. 2009]). Changes in mechanical proerties of cells and nuclei could potentially play a role in these sorting processes.

Additionally, mechanical properties of the surrounding substrate can be sensed by cells and can change cell behavior and direct differentiation of stem cells [Engler et al. 2006]. Besides biochemical signals that are generated in the cytoplasm and can affect transcriptional activity, there is also increasing evidence for the role of a direct mechanical connection from the cell membrane to chromatin in gene regulation, although mechanistic evidence is still lacking (reviewed in [Dahl et al. 2008; Wozniak and Chen 2009; Shivashankar 2011; Wang et al. 2009]).

A speculative model on how mechanics could influence gene expression more directly could look like the following: Externally applied forces are transduced to the nucleus – in addition to biochemical signals – directly via physical connections and influence gene expression, e. g. by changing the accessibility of genes to TFs. Non-random positioning of chromosome regions relative to each other and in relation to the nuclear membrane determines the susceptibility of genes to mechanical cues. Nuclei of ES cells are softer than those of differentiated cells and physical movements of chromatin appear to be more pronounced [Meshorer et al. 2006; Shivashankar 2011]. As lamin A/C is not expressed in ES cells, chromatin is more important as a structural component. Changes in chromatin condensation, as we observed them between HN and LN cells or the onset of lamin A/C expression would then significantly change the susceptibility to mechanical signals in different cell populations.

Testing how mechanical cues potentially influence mES cell differentiation is a major challenge for future research. A number of different experimental approaches are possible: ES cells could be plated on different substrates with distinct mechanical properties, as demonstrated before for MSCs [Engler et al. 2006]. Also, cells could be mechanically stimulated, e. g. on a single cell level using optical stretching or atomic force microscopy, or on a population level by pulling or pushing the substrate. Monitoring transcription on a global level and how fate decisions are influenced could then shed new light on the role mechanics in differentiation.

Finally, our findings are interesting from a biomedical point of view as ES cells have great potential in regenerative medicine. A number of studies have provided evidence that geometric and mechanic substrate properties are important in stem cell culture [Discher et al. 2009; Chowdhury et al. 2010] and can even direct fate decisions in mesenchymal stem cells [Engler et al. 2006]. A better understanding of ES cell and nuclear mechanics and of the biological mechanisms underlying pluripotency and differentiation will be essential to drive progress in this field. Ultimately, this can lead to the development of new and more efficient methods to direct stem cell differentiation for therapeutic purposes.

5. Conclusions

Embryonic stem cells are an invaluable tool for the investigation of pluripotency and early fate decisions in embryonic development. In this study, we found biophysical changes happening in a heterogeneous ES cell population in correlation with the expression of Nanog, a core transcription factor in the maintenance of pluripotency. We demonstrated that in the differentiation-prone low Nanog state both cells an nuclei get softer. When we investigated the molecular causes of this behavior, we found that chromatin is less condensed in the low Nanog state and that changes in chromatin condensation can influence mechanical properties of cells and nuclei.

Our findings are surprising in a number of ways: First, cells and nuclei are generally thought to get stiffer as ES cells differentiate. Second, chromatin is thought to be globally decondensed in the pluripotent state and that heterochromatinization starts with the onset of differentiation. Here we showed that cells in a stable pluripotent state have a slightly more condensed chromatin while it is opened up in cells that are differentiation-prone. Finally, the connection between chromatin condensation, nuclear and cell mechanics is startling.

In the course of this study, we also developed a novel way to probe nuclear mechanics. Although theoretical models are still lacking, optical stretching of nuclei inside living cells could provide new insight into the rheology of nuclei. Further development of this method could particularly be useful for cells that grow in suspension and where nuclear mechanics influences cell mechanical properties like in white blood cells.

We added a few aspects to the characterization of the pluripotent state, however many questions are still unanswered and our research also raises new ones. Do the changes in chromatin condensation and mechanics also occur *in vivo*? Are they of relevance in the early stages of embryonic development? Live cell imaging of embryogenesis and new *in vivo* approaches to monitor cell mechanics and sorting processes will be needed to investigate these problems. Furthermore, future research should be directed to investigate the connections between the mechanical properties of cells and substrates with the organization and potentially regulation of chromatin states.

Besides purely curiosity driven science, biomedical applications can also profit from our research in the long run. A better understanding of stem cells and the regulation of self-renewal and differentiation capacity will be valuable for regenerative medicine where stem cells offer promising possibilities.

A. Appendix

A.1. FRAP Microscopy Settings

Table A.1. – FRAP settings used for experiments on different time scales

Timescale	**Short (10–30 sec)**	**Intermediate (3 min)**	**Long (20–30 min)**
	Image acquisition settings		
Image resolution	256x32	256x256	512x512
Zoom factor	10	8	5
Image depth	12 bit	12 bit	12 bit
Numerical aperture	1.4	1	1
Pinhole [Airy units]	6.28 (max)	6.28 (max)	6.28 (max)
Scan speed	700 Hz	400 Hz	400 Hz
Scan direction	bidirectional x	bidirectional x	bidirectional x
PMT gain	850–1250 V	850–1250 V	850–1250 V
Excitation λ	555 nm	555 nm	555 nm
Excitation laser intensity	2-3 %	2-3 %	2-3 %
Emission bandwidth	575–673 nm	578–674 nm	579–674 nm
	Time series		
Imaging series	preB/postB	preB/postB	preB/postB1/postB2
Frame numbers	150/300	6/18	3/2/20
Time resolution	0.079/0.079 sec	10/10 sec	60/10/60 sec
	Bleach settings		
Cells in ROI	1	1	2
# of bleach boxes	1	1	2
Bleach box dimensions	2x2.5 µm	4x17 µm	4x10–17 µm
Bleach laser intensity	100 %	100 %	100 %
# of bleach frames	10	3	10

A.2. Isolation of Nuclei

To test mechanical properties of isolated nuclei, I developed protocols for the isolation of nuclei from HL-60 cells and ES cells (TNGA cell line). Initial trial experiments were based upon protocols available in the literature [Dahl et al. 2005; Lammerding et al. 2007; Mazumder et al. 2008] or on personal communication (P. Fraser, T. Kolb). However, the protocols had to be modified and

optimized for the cell types we used. The methods were based on swelling suspended cells in hypotonic buffer and disruption of the cell membrane was achieved by either using detergents or mechanical disruption or both. The protocols that worked best for HL-60 cells and TNGA cells are described below.

A.2.1. Nuclear Isolation from HL-60 cells

HL-60 cells were cultured (by A. Ekpenyong) and harvested in exponential growth phase by centrifugation (5 min, 1000 rpm, RT). Cells were resuspended in regular culture medium and Hoechst 33342 (Invitrogen H3570) was added for a final concentration of 5 $\mu g/ml$ to monitor the quality of extracted nuclei in epifluorescence microscopy. Cells were incubated at 37 °C for 30 min and then centrifuged and resuspended in 10 ml ice-cold PBS. From this step on, all working steps were done with pre-cooled buffers and on ice or in a pre-cooled centrifuge (4 °C). Cells were pelleted again as above and washed once in 10 ml swelling buffer (HD-buffer: 10 mM HEPES pH 7.5 (Sigma-Aldrich H3375), 1 mM DL-Dithiothreitol (DTT, Sigma-Aldrich 43816), protease inhibitor (1 pill on 10 ml, Roche 05892791001)) and then resuspended in 2 ml HD-buffer and incubated for 10 min. The swollen cells were then transferred into a pre-cooled tissue dounce grinder (Sigma-Aldrich D9063) and broken up with five strokes with pestle B (tight pestle, 0.0008-0.0022 in clearance). 10x TKMC buffer was added for a final concentration of 1x (1x concentration: 50 mM Tris-HCl pH 7.6 (Sigma-Aldrich 154563), 25 mM KCl (Sigma-Aldrich P9541), 3 mM each $MgCl_2$ and $CaCl_2$ (Sigma-Aldrich M8266 and 499609)) and nuclei were incubated for 10 min to allow equilibration. This buffer was proposed by Lammerding et al. [2007] to mimic intracellular ion concentrations.

Extracted nuclei appeared wrinkled and were smaller than in living cells, which is in good agreement with the literature where tensional prestress was proposed to act on nuclei inside cells [Mazumder and Shivashankar 2010]. Nuclei expanded and were less wrinkled upon addition of 3 mM EDTA, which chelates divalent cations. This is in good agreement with reports that divalent cations condense chromatin [Dahl et al. 2005].

A.2.2. Nuclear Isolation from ES Cells

Isolation Protocol

The protocol described for HL-60 cells did not work for TNGA cells: Cells and nuclei seemed much more fragile and cells and nuclei disrupted in the swelling buffer even without using the dounce homogenizer. Most of the nuclei were disrupted and only debris was left after the procedure.

I developed a more gentle isolation method that resulted in extraction of a high percentage of relatively clean-looking nuclei.

TNGA cells were cultured in T25 flasks to a confluency of about 90 %, incubated for 30 min with 5 $\mu g/ml$ Hoechst and trypsinized as described in section 2.1. Suspended cells (ca. 6E6 cells) were washed in PBS once and resuspended in 4.75 ml TM2 buffer (10 mM Tris-HCl pH 7.6, 2 mM $MgCl_2$, protease inhibitor as above). Cells were then incubated for 5 min on RT and ice each. Triton-X 100 (Sigma-Aldrich T8787) was added for a final concentration of 0.5 % and cells were kept on ice another 5 min. The cells were then sheared by passing them through a syringe needle ten times (BD microlance 21 G, 304432). Nuclei were centrifuged (5 min, 1000 rpm) and resuspended in ice-cold PBS or 1x TKMC buffer (both supplemented with protease inhibitor). See fig. A.1 for nuclei imaged at the individual steps.

Results and Discussion

As for HL-60 nuclei, size and shape of isolated nuclei depended on buffer conditions. Dahl et al. [2005] reported swelling of 170 % of nuclei when the concentration of divalent cations was reduced from 6 mM to 0 mM. We did not quantify the effect, however, the size changes of the nuclei were in a similar regime (compare the three rightmost images in fig. A.1 (A)). These and other authors suggest that the volume of an isolated nucleus is critically dependent on chromatin compaction and reduction of histone tail interactions by withdrawal of divalent cations or digestion of histones was shown to have a swelling effect [Dahl et al. 2005; Mazumder et al. 2008; Mazumder and Shivashankar 2010]. This effect was proposed to occur due to the entropic pressure of chromatin when it is decondensed [Mazumder and Shivashankar 2010].

Nuclei in the optical stretcher could be trapped successfully, however, nuclei behaved different to cells when the laser power was increased to stretching power. Nuclei resuspended in PBS without any divalent cations were easier to trap and they expanded as a whole when the laser power was increased from to 3 W (fig. A.1 B). Based upon an estimated increase of the radius of 15 %, this would mean a 50 % increase in volume. Interestingly, nuclei resuspended in different buffer conditions (1x TKMC, including 6 mM divalent cations in total), did not expand but rather contracted by about 8 % in terms of volume (fig. A.1 C). Therefore, although optical forces act on the nuclei (otherwise they would not be trapped), they behave completely different in the OS than nuclei resuspended in PBS.

Since changes in the ratio of major versus minor axis were negligible compared to the overall size changes, we speculated that other effects than optical forces acting on the nuclear membrane would dominate the observed behavior. To test whether a temperature increase, which is known to occur in the OS when the laser power is increased, could cause the effect, I used a laser with a

higher wavelength ($\lambda = 1480\,\mathrm{nm}$) that can be used in the same setup in parallel to the 1064 nm laser. This laser does not cause any optical stretching since it is only coupled into one of the fibers, but was shown to increase the temperature inside the trap. Using the two lasers in parallel, one for trapping and one to increase the temperature, I found the same effects as for nuclei that were subjected to a 3 W stretch power: Nuclei in PBS expanded while nuclei in TKMC buffer contracted upon heating. This clearly demonstrates that heat effects cause the changes in nuclear size when the laser intensity is increased.

It remains subject of speculation why nuclei in PBS expand while nuclei in TKMC contract upon heating. Chromatin has been shown to act as an entropic spring and the spring properties were proposed to be of relevance e. g. in the formation of the mitotic spindle (reviewed in [Bloom 2008]). An entropic spring has the tendency to return to the maximum entropy state upon force application. The spring constant κ of an entropic spring is proportional to $k_B T$/persistence length [Bloom 2008]. This means that the spring constant increases with temperature and decreases with increasing persistence length. The persistence length, a measure that describes the resistance of a polymer to thermal force, is dependent on packaging with histones for DNA [Bloom 2008]. Therefore, changes in temperature or chromatin packaging can affect the spring constant of chromatin.

We did not follow up these effects in heating of nuclei, however, our data stress the critical dependence of mechanical properties of extracted nuclei on buffer conditions. We found that nuclei do stretch within intact cells and chose this method to characterize chromatin condensation in ES cells. However, more systematic experiments with extracted nuclei, e. g. with varying salt conditions, enzymatic digestion of DNA or histone proteins or chemically induced chromatin (de-)condensation, could shed light on the strange effect that we observed. Further experiments could also provide insight into the structural role of chromatin inside nuclei.

A.3. Disclaimer

Ich habe mich bemüht, sämtliche Inhaber der Bildrechte ausfindig zu machen und ihre Zustimmung zur Verwendung der Bilder in dieser Arbeit eingeholt. Sollte dennoch eine Urheberrechtsverletzung bekannt werden, ersuche ich um Meldung bei mir.

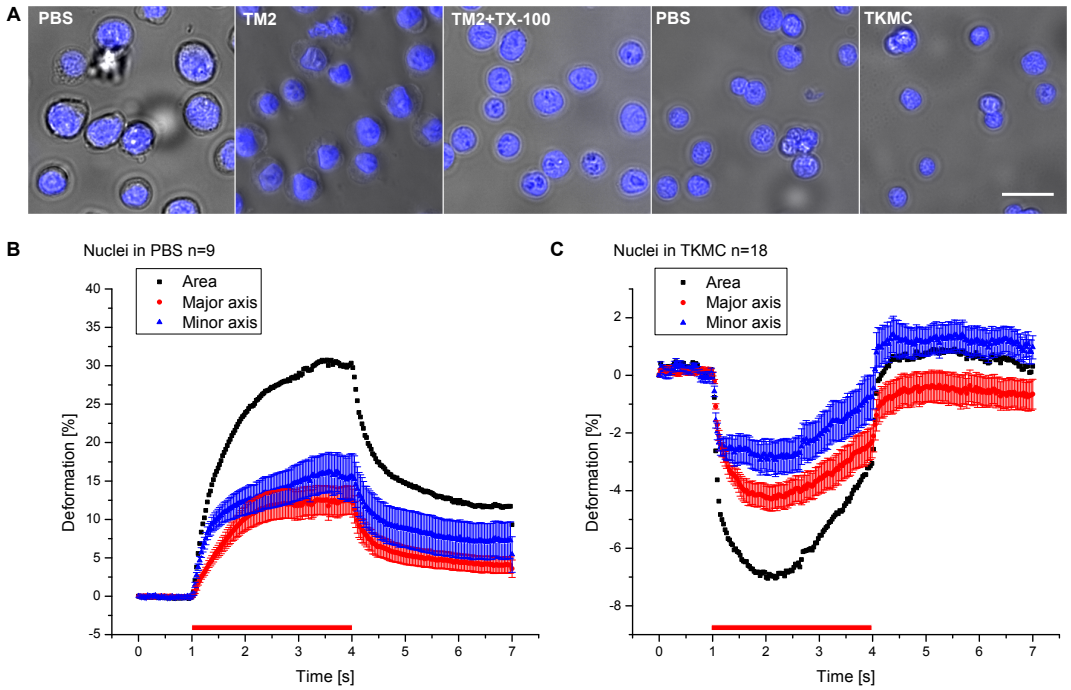

Figure A.1. – Isolation and optical stretching of ES cell nuclei. (A) Nuclei imaged at different stages of the isolation process (bright field and Hoechst channel, overlay). Control cells resuspended in PBS and cells in swelling buffer TM2 still have cytoplasm around the nuclei. After the addition of triton-X 100, the the cell membrane bursts. Nuclei were then pelleted and resuspended in PBS or 1x TKMC buffer (see text for details). Note the considerable size changes of the nuclei in dependence on buffer conditions. Scale bar 20 µm. (B and C) Nuclei were trapped and stretched in and optical stretcher. The red bar indicates the time when the laser was on stretching power (3 W). (B) Nuclei expand as a whole when resuspended in PBS, indicated by an increase of both the major (laser axis) and minor axis length (perpendicular to the major axis). The black curves represent the calculated projected area. (C) Nuclei resuspended in 1x TKMC buffer (containing 3 mM $MgCl_2$ and $CaCl_2$) contract in both the major and the minor axis.

B. Curriculum Vitae

Personal

Name	Markus Höpfler
Date of Birth	24^{th} of November 1986
Place of Birth	Wels, Austria
Citizenship	Austria
Contact	hoepflerm@gmx.at

Schooling

1992-1996	Primary School Frauenstein, Upper Austria
1996-2004	Grammar School Stiftsgymnasium Kremsmünster, Upper Austria
June 2004	Matura passed with distinction

University

since 2005	Diploma Studies Molecular Biology, University of Vienna
13^{th} of Jan. 2009	1^{st} diploma examination Molecular Biology passed with distinction
Speicialization	Cell biology, Genetics, Microbiology
Lab practices	Dr. Thomas Marlovits, IMBA Vienna
	Prof. Michael Jantsch, University of Vienna
	Prof. Wolfram Weckwerth, University of Vienna
	Prof. Matthias Horn, University of Vienna
Diploma thesis	with Dr. Jochen Guck, University of Cambridge, UK, Cavendish Laboratory
2010/2011	Title: 'Connections between Cell Mechanics and Chromatin Condensation in Embryonic Stem Cells'

Additional Experiences and Scholarships

2007	Performance Scholarship, Medical University of Vienna
2008–2010	Performance Scholarship, University of Vienna
2010	Scholarship 'Förderungsstipendium', University of Vienna
2010	Tutor for the lab course 'Metabolomics'

Conferences Attended

Sep. 2011	Physics of Living Matter, Cambridge UK

Scientific Publications

In preparation: K. Chalut*, M. Höpfler*, F. Lautenschläger, A. Martinez-Arias, J. Guck. *Unlocking pluripotency: chromatin decondensation and nuclear softening key for differentiation.*

*Authors contributed equally to this work.

Foreign Languages

French: Basic knowledge, English: Excellent knowledge

Computer Software Skills

Good knowledge: Office Package, Latex, ImageJ, Origin Software

Basic experience: Matlab

References

B. Alberts, A. Johnson, J. Lewis, M. Raff, K. Roberts, and P. Walter. *Molecular Biology of the Cell*. Garland Science, New York, 4th edition, 2002.

R. Ananthakrishnan, J. Guck, F. Wottawah, S. Schinkinger, B. Lincoln, M. Romeyke, T. Moon, and J. Käs. Quantifying the contribution of actin networks to the elastic strength of fibroblasts. *Journal of Theoretical Biology*, 242(2):502–16, Sept. 2006.

A. Ashkin. Acceleration and Trapping of Particles by Radiation Pressure. *Physical Review Letters*, 24 (4):156–159, 1970.

A. A. Avilion, S. K. Nicolis, L. H. Pevny, L. Perez, N. Vivian, and R. Lovell-Badge. Multipotent cell lineages in early mouse development depend on SOX2 function. *Genes & Development*, 17(1):126–40, Jan. 2003.

E. Bártová, J. Pacherník, A. Kozubík, and S. Kozubek. Differentiation-specific association of HP1alpha and HP1beta with chromocentres is correlated with clustering of TIF1beta at these sites. *Histochemistry and Cell Biology*, 127(4):375–88, Apr. 2007.

B. E. Bernstein, T. S. Mikkelsen, X. Xie, M. Kamal, D. J. Huebert, J. Cuff, B. Fry, A. Meissner, M. Wernig, K. Plath, R. Jaenisch, A. Wagschal, R. Feil, S. L. Schreiber, and E. S. Lander. A bivalent chromatin structure marks key developmental genes in embryonic stem cells. *Cell*, 125(2):315–26, Apr. 2006.

D. Bhattacharya, S. Talwar, A. Mazumder, and G. V. Shivashankar. Spatio-temporal plasticity in chromatin organization in mouse cell differentiation and during Drosophila embryogenesis. *Biophysical journal*, 96(9):3832–9, May 2009.

K. S. Bloom. Beyond the code: the mechanical properties of DNA as they relate to mitosis. *Chromosoma*, 117(2):103–10, Apr. 2008.

L. Boyde, K. J. Chalut, and J. Guck. Interaction of Gaussian beam with near-spherical particle: an analytic-numerical approach for assessing scattering and stresses. *Journal of the Optical Society of America. A, Optics, image science, and vision*, 26(8):1814–26, Aug. 2009.

J. P. Brody, Y. Han, R. H. Austin, and M. Bitensky. Deformation and flow of red blood cells in a synthetic lattice: evidence for an active cytoskeleton. *Biophysical Journal*, 68(6):2224–32, June 1995.

J. L. V. Broers, H. J. H. Kuijpers, C. Ostlund, H. J. Worman, J. Endert, and F. C. S. Ramaekers. Both lamin A and lamin C mutations cause lamina instability as well as loss of internal nuclear lamin organization. *Experimental Cell Research*, 304(2):582–92, Apr. 2005.

A. Brunsting and P. F. Mullaney. Differential light scattering from spherical mammalian cells. *Biophysical journal*, 14(6):439–53, June 1974.

N. Caille, Y. Tardy, and J. J. Meister. Assessment of strain field in endothelial cells subjected to uniaxial deformation of their substrate. *Annals of Biomedical Engineering*, 26(3):409–16, 1998.

N. Caille, O. Thoumine, Y. Tardy, and J.-J. Meister. Contribution of the nucleus to the mechanical properties of endothelial cells. *Journal of Biomechanics*, 35(2):177–87, Feb. 2002.

H. Cedar and Y. Bergman. Linking DNA methylation and histone modification: patterns and paradigms. *Nature Reviews. Genetics*, 10(5):295–304, May 2009.

K. J. Chalut, K. Kulangara, A. Wax, and K. W. Leong. Stem cell differentiation indicated by changes across scales in subcellular architecture. *Integrative Biology*, 3:863–867, 2011.

I. Chambers, D. Colby, M. Robertson, J. Nichols, S. Lee, S. Tweedie, and A. Smith. Functional Expression Cloning of Nanog, a Pluripotency Sustaining Factor in Embryonic Stem Cells. *Cell*, 113:643–655, 2003.

I. Chambers, J. Silva, D. Colby, J. Nichols, B. Nijmeijer, M. Robertson, J. Vrana, K. Jones, L. Grotewold, and A. Smith. Nanog safeguards pluripotency and mediates germline development. *Nature*, 450(7173): 1230–4, Dec. 2007.

C. Chazaud, Y. Yamanaka, T. Pawson, and J. Rossant. Early lineage segregation between epiblast and primitive endoderm in mouse blastocysts through the Grb2-MAPK pathway. *Developmental Cell*, 10 (5):615–24, May 2006.

F. Chowdhury, S. Na, D. Li, Y.-c. Poh, T. S. Tanaka, and N. Wang. Material properties of the cell dictate stress-induced spreading and differentiation in embryonic stem cells. *Nature Materials*, 9(1): 82–88, 2010.

P. Cicuta and A. M. Donald. Microrheology: a review of the method and applications. *Soft Matter*, 3 (12):1449, 2007.

P. Collas. Programming differentiation potential in mesenchymal stem cells. *Epigenetics*, 5(6):476–82, Aug. 2010.

D. Constantinescu, H. L. Gray, P. J. Sammak, G. P. Schatten, and A. B. Csoka. Lamin A/C expression is a marker of mouse and human embryonic stem cell differentiation. *Stem Cells*, 24(1):177–85, Jan. 2006.

M. Crisp, Q. Liu, K. Roux, J. B. Rattner, C. Shanahan, B. Burke, P. D. Stahl, and D. Hodzic. Coupling of the nucleus and cytoplasm: role of the LINC complex. *The Journal of Cell Biology*, 172(1):41–53, Jan. 2006.

K. Cui, C. Zang, T.-Y. Roh, D. E. Schones, R. W. Childs, W. Peng, and K. Zhao. Chromatin signatures in multipotent human hematopoietic stem cells indicate the fate of bivalent genes during differentiation. *Cell Stem Cell*, 4(1):80–93, Jan. 2009.

K. N. Dahl and A. Kalinowski. Nucleoskeleton mechanics at a glance. *Journal of Cell Science*, 124(Pt 5):675–8, Mar. 2011.

K. N. Dahl, A. J. Engler, J. D. Pajerowski, and D. E. Discher. Power-law rheology of isolated nuclei with deformation mapping of nuclear substructures. *Biophysical Journal*, 89(4):2855–64, Oct. 2005.

K. N. Dahl, A. J. S. Ribeiro, and J. Lammerding. Nuclear shape, mechanics, and mechanotransduction. *Circulation Research*, 102(11):1307–18, June 2008.

M. de Frutos, E. Raspaud, A. Leforestier, and F. Livolant. Aggregation of nucleosomes by divalent cations. *Biophysical Journal*, 81(2):1127–32, Aug. 2001.

S. Deguchi, K. Maeda, T. Ohashi, and M. Sato. Flow-induced hardening of endothelial nucleus as an intracellular stress-bearing organelle. *Journal of Biomechanics*, 38(9):1751–9, Sept. 2005.

D. E. Discher, D. J. Mooney, and P. W. Zandstra. Growth factors, matrices, and forces combine and control stem cells. *Science*, 324(5935):1673–7, June 2009.

D. Dorner, J. Gotzmann, and R. Foisner. Nucleoplasmic lamins and their interaction partners, LAP2alpha, Rb, and BAF, in transcriptional regulation. *The FEBS Journal*, 274(6):1362–73, Mar. 2007.

C. G. dos Remedios, D. Chhabra, M. Kekic, I. V. Dedova, M. Tsubakihara, D. A. Berry, and N. J. Nosworthy. Actin binding proteins: regulation of cytoskeletal microfilaments. *Physiological Reviews*, 83(2):433–73, Apr. 2003.

S. Efroni, R. Duttagupta, J. Cheng, H. Dehghani, D. J. Hoeppner, C. Dash, D. P. Bazett-Jones, S. Le Grice, R. D. G. McKay, K. H. Buetow, T. R. Gingeras, T. Misteli, and E. Meshorer. Global transcription in pluripotent embryonic stem cells. *Cell stem cell*, 2(5):437–47, May 2008.

J. C. Eissenberg and S. C. R. Elgin. The HP1 protein family: getting a grip on chromatin. *Current Opinion in Genetics & Development*, 10:204–210, 2000.

A. J. Engler, S. Sen, H. L. Sweeney, and D. E. Discher. Matrix Elasticity Directs Stem Cell Lineage Specification. *Cell*, 126:677–689, 2006.

C. L. Fisher and A. G. Fisher. Chromatin states in pluripotent, differentiated, and reprogrammed cells. *Current Opinion in Genetics & Development*, 21(2):140–6, Apr. 2011.

D. a. Fletcher and R. D. Mullins. Cell mechanics and the cytoskeleton. *Nature*, 463(7280):485–92, Jan. 2010.

R. a. Foty, C. M. Pfleger, G. Forgacs, and M. S. Steinberg. Surface tensions of embryonic tissues predict their mutual envelopment behavior. *Development*, 122(5):1611–20, May 1996.

S. Gabriele, A.-M. Benoliel, P. Bongrand, and O. Théodoly. Microfluidic investigation reveals distinct roles for actin cytoskeleton and myosin II activity in capillary leukocyte trafficking. *Biophysical Journal*, 96(10):4308–18, May 2009.

M. L. Gardel, K. E. Kasza, C. P. Brangwynne, J. Liu, and D. A. Weitz. Chapter 19: Mechanical response of cytoskeletal networks. *Methods in Cell Biology*, 89:487–519, Jan. 2008.

A. Gaspar-Maia, A. Alajem, F. Polesso, R. Sridharan, M. J. Mason, A. Heidersbach, J. a. Ramalho-Santos, M. T. McManus, K. Plath, E. Meshorer, and M. Ramalho-Santos. Chd1 regulates open chromatin and pluripotency of embryonic stem cells. *Nature*, 460(7257):863–8, Aug. 2009.

S. F. Gilbert. *Developmental Biology*. Sinauer Associates, Sunderland, MA, 9th edition, 2010.

J. Guck, R. Ananthakrishnan, H. Mahmood, T. J. Moon, C. C. Cunningham, and J. Käs. The optical stretcher: a novel laser tool to micromanipulate cells. *Biophysical journal*, 81(2):767–84, Aug. 2001.

J. Guck, F. Lautenschläger, S. Paschke, and M. Beil. Critical review: cellular mechanobiology and amoeboid migration. *Integrative Biology : Quantitative Biosciences from nano to macro*, 2(11-12): 575–83, Nov. 2010.

F. Guilak. Compression-induced changes in the shape and volume of the chondrocyte nucleus. *Journal of Biomechanics*, 28(12):1529–41, Dec. 1995.

F. Guilak, J. R. Tedrow, and R. Burgkart. Viscoelastic properties of the cell nucleus. *Biochemical and Biophysical Research Communications*, 269(3):781–6, Mar. 2000.

J. Head, L. L. Lee, D. J. Field, and J. C. Lee. Equilibrium and Rapid Kinetic Studies on Nocodazole-Tubulin Interaction. *Society*, 260(20):11060–11066, 1985.

D. M. Heiserman. Methods of Hematology, 2004. URL `http://www.free-ed.net/sweethaven/MedTech/Hematology/lessonMain.asp?iNum=0406`.

J. A. Hildebrand and D. Rugar. Measurement of cellular elastic properties by acoustic microscopy. *Journal of microscopy*, 134(Pt 3):245–60, June 1984.

R. M. Hochmuth. Micropipette aspiration of living cells. *Journal of Biomechanics*, 33(1):15–22, Jan. 2000.

W. A. Hofmann, T. Johnson, M. Klapczynski, J.-L. Fan, and P. de Lanerolle. From transcription to transport: emerging roles for nuclear myosin I. *Biochemistry and Cell Biology*, 84(4):418–26, Aug. 2006.

D. E. Ingber. Tensegrity I. Cell structure and hierarchical systems biology. *Journal of Cell Science*, 116 (7):1157–1173, Apr. 2003.

S. Ito, A. C. D'Alessio, O. V. Taranova, K. Hong, L. C. Sowers, and Y. Zhang. Role of Tet proteins in 5mC to 5hmC conversion, ES-cell self-renewal and inner cell mass specification. *Nature*, 466(7310): 1129–33, Aug. 2010.

N. Ivanova, R. Dobrin, R. Lu, I. Kotenko, J. Levorse, C. DeCoste, X. Schafer, Y. Lun, and I. R. Lemischka. Dissecting self-renewal in stem cells with RNA interference. *Nature*, 442(7102):533–8, Aug. 2006.

P. A. Janmey, U. Euteneuer, P. Traub, and M. Schliwa. Viscoelastic properties of vimentin compared with other filamentous biopolymer networks. *The Journal of Cell Biology*, 113(1):155–60, Apr. 1991.

B. Joffe, H. Leonhardt, and I. Solovei. Differentiation and large scale spatial organization of the genome. *Current Opinion in Genetics & Development*, 20(5):562–9, Oct. 2010.

T. Kalmar, C. Lim, P. Hayward, S. Muñoz Descalzo, J. Nichols, J. Garcia-Ojalvo, and A. Martinez Arias. Regulated fluctuations in nanog expression mediate cell fate decisions in embryonic stem cells. *PLoS biology*, 7(7):e1000149, July 2009.

A. Karperien. Fraclac for ImageJ, 2007. URL `http://rsb.info.nih.gov/ij/plugins/fraclac/FLHelp/Introduction.htm`.

R. Keller. Shaping the vertebrate body plan by polarized embryonic cell movements. *Science*, 298(5600): 1950–4, Dec. 2002.

H. Kimura and P. R. Cook. Kinetics of core histones in living human cells: little exchange of H3 and H4 and some rapid exchange of H2B. *The Journal of Cell Biology*, 153(7):1341–53, June 2001.

S. M. Kooistra, V. van den Boom, R. P. Thummer, F. Johannes, R. Wardenaar, B. M. Tesson, L. M. Veenhoff, F. Fusetti, L. P. O'Neill, B. M. Turner, G. de Haan, and B. J. L. Eggen. Undifferentiated embryonic cell transcription factor 1 regulates ESC chromatin organization and gene expression. *Stem Cells*, 28(10):1703–14, Oct. 2010.

M. Krieg, Y. Arboleda-Estudillo, P.-H. Puech, J. Käfer, F. Graner, D. J. Müller, and C.-P. Heisenberg. Tensile forces govern germ-layer organization in zebrafish. *Nature cell biology*, 10(4):429–36, Apr. 2008.

T. Kuroda, M. Tada, H. Kubota, H. Kimura, S.-y. Hatano, H. Suemori, N. Nakatsuji, and T. Tada. Octamer and Sox elements are required for transcriptional cis regulation of Nanog gene expression. *Molecular and Cellular Biology*, 25(6):2475–85, Mar. 2005.

J. Lammerding, L. G. Fong, J. Y. Ji, K. Reue, C. L. Stewart, S. G. Young, and R. T. Lee. Lamins A and C but not lamin B1 regulate nuclear mechanics. *The Journal of Biological Chemistry*, 281(35): 25768–80, Sept. 2006.

J. Lammerding, K. N. Dahl, D. E. Discher, and R. D. Kamm. Nuclear mechanics and methods. *Methods in Cell Biology*, 83(07):269–94, Jan. 2007.

F. Lautenschläger. *Cell Compliance - Cytoskeletal Origin and Importance for Cellular Function.* Phd thesis, University of Cambridge, 2011.

F. Lautenschläger, S. Paschke, S. Schinkinger, A. Bruel, M. Beil, and J. Guck. The regulatory role of cell mechanics for migration of differentiating myeloid cells. *Proceedings of the National Academy of Sciences of the United States of America*, 106(37):15696–701, Sept. 2009.

P. F. Leblond, P. L. LaCelle, and R. I. Weed. Cellular deformability: a possible determinant of the normal release of maturing erythrocytes from the bone marrow. *Blood*, 37(1):40–6, Jan. 1971.

B. Lincoln, S. Schinkinger, K. Travis, F. Wottawah, S. Ebert, F. Sauer, and J. Guck. Reconfigurable microfluidic integration of a dual-beam laser trap with biomedical applications. *Biomedical Microdevices*, 9(5):703–10, Oct. 2007a.

B. Lincoln, F. Wottawah, S. Schinkinger, S. Ebert, and J. Guck. High-throughput rheological measurements with an optical stretcher. *Methods in Cell Biology*, 83(07):397–423, Jan. 2007b.

M. Linkert, C. T. Rueden, C. Allan, J.-M. Burel, W. Moore, A. Patterson, B. Loranger, J. Moore, C. Neves, D. Macdonald, A. Tarkowska, C. Sticco, E. Hill, M. Rossner, K. W. Eliceiri, and J. R. Swedlow. Metadata matters: access to image data in the real world. *The Journal of Cell Biology*, 189 (5):777–82, May 2010.

S. K. Mallanna, B. D. Ormsbee, M. Iacovino, J. M. Gilmore, J. L. Cox, M. Kyba, M. P. Washburn, and A. Rizzino. Proteomic analysis of Sox2-associated proteins during early stages of mouse embryonic stem cell differentiation identifies Sox21 as a novel regulator of stem cell fate. *Stem Cells*, 28(10): 1715–27, Oct. 2010.

J. M. Maloney, D. Nikova, F. Lautenschläger, E. Clarke, R. Langer, J. Guck, and K. J. Van Vliet. Mesenchymal stem cell mechanics from the attached to the suspended state. *Biophysical Journal*, 99 (8):2479–87, Oct. 2010.

A. J. Maniotis, C. S. Chen, and D. E. Ingber. Demonstration of mechanical connections between integrins, cytoskeletal filaments, and nucleoplasm that stabilize nuclear structure. *Proceedings of the National Academy of Sciences of the United States of America*, 94(3):849–54, Mar. 1997.

Y. Matsui, K. Zsebo, and B. L. Hogan. Derivation of pluripotential embryonic stem cells from murine primordial germ cells in culture. *Cell*, 70(5):841–7, Sept. 1992.

A. Mazumder and G. V. Shivashankar. Gold-nanoparticle-assisted laser perturbation of chromatin assembly reveals unusual aspects of nuclear architecture within living cells. *Biophysical Journal*, 93(6): 2209–16, Sept. 2007.

A. Mazumder and G. V. Shivashankar. Emergence of a prestressed eukaryotic nucleus during cellular differentiation and development. *Journal of the Royal Society, Interface / the Royal Society*, 7 Suppl 3(March):S321–30, June 2010.

A. Mazumder, T. Roopa, A. Basu, L. Mahadevan, and G. V. Shivashankar. Dynamics of chromatin decondensation reveals the structural integrity of a mechanically prestressed nucleus. *Biophysical Journal*, 95(6):3028–35, Sept. 2008.

L. Mazzarella, H. F. Jø rgensen, J. Soza-Ried, A. V. Terry, S. Pearson, G. Lacaud, V. Kouskoff, M. Merkenschlager, and A. G. Fisher. Embryonic stem cell-derived hemangioblasts remain epigenetically plastic and require PRC1 to prevent neural gene expression. *Blood*, 117(1):83–7, Jan. 2011.

S. Medjkane, C. Perez-Sanchez, C. Gaggioli, E. Sahai, and R. Treisman. Myocardin-related transcription factors and SRF are required for cytoskeletal dynamics and experimental metastasis. *Nature Cell Biology*, 11(3):257–68, Mar. 2009.

S. M. Meilhac, R. J. Adams, S. a. Morris, A. Danckaert, J.-F. Le Garrec, and M. Zernicka-Goetz. Active cell movements coupled to positional induction are involved in lineage segregation in the mouse blastocyst. *Developmental Biology*, 331(2):210–21, July 2009.

E. Meshorer and T. Misteli. Chromatin in pluripotent embryonic stem cells and differentiation. *Nature reviews. Molecular cell biology*, 7(7):540–6, July 2006.

E. Meshorer, D. Yellajoshula, E. George, P. J. Scambler, D. T. Brown, and T. Misteli. Hyperdynamic plasticity of chromatin proteins in pluripotent embryonic stem cells. *Developmental Cell*, 10(1):105–16, Jan. 2006.

T. S. Mikkelsen, M. Ku, D. B. Jaffe, B. Issac, E. Lieberman, G. Giannoukos, P. Alvarez, W. Brockman, T.-K. Kim, R. P. Koche, W. Lee, E. Mendenhall, A. O'Donovan, A. Presser, C. Russ, X. Xie, A. Meissner, M. Wernig, R. Jaenisch, C. Nusbaum, E. S. Lander, and B. E. Bernstein. Genome-wide maps of chromatin state in pluripotent and lineage-committed cells. *Nature*, 448(7153):553–60, Aug. 2007.

F. Mohn, M. Weber, M. Rebhan, T. C. Roloff, J. Richter, M. B. Stadler, M. Bibel, and D. Schübeler. Lineage-specific polycomb targets and de novo DNA methylation define restriction and potential of neuronal progenitors. *Molecular Cell*, 30(6):755–66, June 2008.

M. Monk and A. McLaren. X-chromosome activity in foetal germ cells of the mouse. *Journal of embryology and experimental morphology*, 63:75–84, June 1981.

P. Navarro, I. Chambers, V. Karwacki-Neisius, C. Chureau, C. Morey, C. Rougeulle, and P. Avner. Molecular coupling of Xist regulation and pluripotency. *Science*, 321(5896):1693–5, Sept. 2008.

J. Nichols and A. Smith. The origin and identity of embryonic stem cells. *Development*, 138(1):3–8, Jan. 2011.

J. Nichols, B. Zevnik, K. Anastassiadis, H. Niwa, D. Klewe-Nebenius, I. Chambers, H. Schöler, and A. Smith. Formation of pluripotent stem cells in the mammalian embryo depends on the POU transcription factor Oct4. *Cell*, 95(3):379–91, Oct. 1998.

H. Niwa. How is pluripotency determined and maintained? *Development*, 134(4):635–46, Feb. 2007.

H. Niwa, J. Miyazaki, and A. G. Smith. Quantitative expression of Oct-3/4 defines differentiation, dedifferentiation or self-renewal of ES cells. *Nature Genetics*, 24(4):372–6, Apr. 2000.

S. Orkin and K. Hochedlinger. Chromatin Connections to Pluripotency and Cellular Reprogramming. *Cell*, 145(6):835–850, 2011.

J. D. Pajerowski, K. N. Dahl, F. L. Zhong, P. J. Sammak, and D. E. Discher. Physical plasticity of the nucleus in stem cell differentiation. *Proceedings of the National Academy of Sciences of the United States of America*, 104(40):15619–15624, 2007.

E. Paluch and C.-P. Heisenberg. Biology and physics of cell shape changes in development. *Current Biology*, 19(17):R790–9, Sept. 2009.

M. Pardo, B. Lang, L. Yu, H. Prosser, A. Bradley, M. M. Babu, and J. Choudhary. An expanded Oct4 interaction network: implications for stem cell biology, development, and disease. *Cell Stem Cell*, 6(4): 382–95, Apr. 2010.

T. Pederson and U. Aebi. Nuclear actin extends, with no contraction in sight. *Molecular Biology of the Cell*, 16(11):5055–60, Nov. 2005.

N. Petersen, W. B. Mcconnaughey, and E. L. Elson. Dependence of locally measured cellular deformability on position on the cell, temperature, and cytochalasin B. *Proceedings of the National Academy of Sciences of the United States of America*, 79(September):5327–5331, 1982.

R. D. Phair and T. Misteli. High mobility of proteins in the mammalian cell nucleus. *Nature*, 404(6778): 604–9, Apr. 2000.

R. D. Phair, S. a. Gorski, and T. Misteli. Measurement of dynamic protein binding to chromatin in vivo, using photobleaching microscopy. *Methods in Enzymology*, 375(2000):393–414, Jan. 2004.

A. Pillarisetti, J. P. Desai, H. Ladjal, A. Schiffmacher, A. Ferreira, and C. L. Keefer. Mechanical Phenotyping of Mouse Embryonic Stem Cells: Increase in Stiffness with Differentiation. *Cellular Reprogramming*, 13(4):110705113105009, July 2011.

B. Plusa, A. Piliszek, S. Frankenberg, J. Artus, and A.-K. Hadjantonakis. Distinct sequential cell behaviours direct primitive endoderm formation in the mouse blastocyst. *Development*, 135(18):3081–91, Sept. 2008.

G. Posern and R. Treisman. Actin' together: serum response factor, its cofactors and the link to signal transduction. *Trends in Cell Biology*, 16(11):588–96, Nov. 2006.

W. Rasband. ImageJ. URL `http://imagej.nih.gov/ij/`.

W. Reik, W. Dean, and J. Walter. Epigenetic reprogramming in mammalian development. *Science*, 293 (5532):1089–93, Aug. 2001.

T. W. Remmerbach, F. Wottawah, J. Dietrich, B. Lincoln, C. Wittekind, and J. Guck. Oral cancer diagnosis by mechanical phenotyping. *Cancer Research*, 69(5):1728–32, Mar. 2009.

L. Ringrose, H. Ehret, and R. Paro. Distinct Contributions of Histone H3 Lysine 9 and 27 Methylation to Locus-Specific Stability of Polycomb Complexes. *Molecular Cell*, 16:641–653, 2004.

N. Rougier, D. Bourc'his, D. M. Gomes, A. Niveleau, M. Plachot, A. Pàldi, and E. Viegas-Péquignot. Chromosome methylation patterns during mammalian preimplantation development. *Genes & Development*, 12(14):2108–13, July 1998.

F. Samson, J. A. Donoso, I. Heller-Bettinger, D. Watson, and R. H. Himes. Nocodazole action on tubulin assembly, axonal ultrastructure and fast axoplasmic transport. *The Journal of Pharmacology and Experimental Therapeutics*, 208(3):411–7, Mar. 1979.

P. Savatier, H. Lapillonne, L. Jirmanova, L. Vitelli, and J. Samarut. Analysis of the cell cycle in mouse embryonic stem cells. *Methods in Molecular Biology*, 185(3):27–33, Jan. 2002.

H. Schiessel. The physics of chromatin. *Journal of Physics: Condensed Matter*, (15):R599–R774, 2003.

E. C. Schirmer and R. Foisner. Proteins that associate with lamins: many faces, many functions. *Experimental Cell Research*, 313(10):2167–79, June 2007.

G. V. Shivashankar. Mechanosignaling to the cell nucleus and gene regulation. *Annual Review of Biophysics*, 40:361–78, June 2011.

J. Silva and A. Smith. Capturing pluripotency. *Cell*, 132(4):532–6, Feb. 2008.

J. Silva, J. Nichols, T. W. Theunissen, G. Guo, A. L. van Oosten, O. Barrandon, J. Wray, S. Yamanaka, I. Chambers, and A. Smith. Nanog is the gateway to the pluripotent ground state. *Cell*, 138(4):722–37, Aug. 2009.

A. M. Singh, T. Hamazaki, K. E. Hankowski, and N. Terada. A heterogeneous expression pattern for Nanog in embryonic stem cells. *Stem Cells*, 25(10):2534–42, Oct. 2007.

P. Skoglund, A. Rolo, X. Chen, B. M. Gumbiner, and R. Keller. Convergence and extension at gastrulation require a myosin IIB-dependent cortical actin network. *Development*, 135(14):2435–44, Aug. 2008.

K. Takahashi and S. Yamanaka. Induction of pluripotent stem cells from mouse embryonic and adult fibroblast cultures by defined factors. *Cell*, 126(4):663–76, Aug. 2006.

T. W. Theunissen and J. C. R. Silva. Switching on pluripotency: a perspective on the biological requirement of Nanog. *Philosophical transactions of the Royal Society of London. Series B, Biological sciences*, 366(1575):2222–9, Aug. 2011.

P. Thévenaz, U. E. Ruttimann, and M. Unser. A pyramid approach to subpixel registration based on intensity. *IEEE transactions on image processing : a publication of the IEEE Signal Processing Society*, 7(1):27–41, Jan. 1998.

O. Thoumine and A. Ott. Time scale dependent viscoelastic and contractile regimes in fibroblasts probed by microplate manipulation. *Journal of Cell Science*, 110 (Pt 17:2109–16, Sept. 1997.

K. F. Tóth, T. a. Knoch, M. Wachsmuth, M. Frank-Stöhr, M. Stöhr, C. P. Bacher, G. Müller, and K. Rippe. Trichostatin A-induced histone acetylation causes decondensation of interphase chromatin. *Journal of Cell Science*, 117(Pt 18):4277–87, Aug. 2004.

M. A. Tsai, R. E. Waugh, and P. C. Keng. Cell cycle-dependence of HL-60 cell deformability. *Biophysical Journal*, 70(4):2023–9, Apr. 1996.

Y. Tseng, J. S. H. Lee, T. P. Kole, I. Jiang, and D. Wirtz. Micro-organization and visco-elasticity of the interphase nucleus revealed by particle nanotracking. *Journal of Cell Science*, 117(Pt 10):2159–67, Apr. 2004.

V. L. R. M. Verstraeten and J. Lammerding. Experimental techniques for study of chromatin mechanics in intact nuclei and living cells. *Chromosome Research*, 16(3):499–510, Jan. 2008.

T. Wakatsuki, B. Schwab, N. C. Thompson, and E. L. Elson. Effects of cytochalasin D and latrunculin B on mechanical properties of cells. *Journal of Cell Science*, 114(Pt 5):1025–36, Mar. 2001.

J. Wang, S. Rao, J. Chu, X. Shen, D. N. Levasseur, T. W. Theunissen, and S. H. Orkin. A protein interaction network for pluripotency of embryonic stem cells. *Nature*, 444(7117):364–8, Nov. 2006.

N. Wang. Mechanical interactions among cytoskeletal filaments. *Hypertension*, 32(1):162–5, July 1998.

N. Wang, J. D. Tytell, and D. E. Ingber. Mechanotransduction at a distance: mechanically coupling the extracellular matrix with the nucleus. *Nature reviews. Molecular cell biology*, 10(1):75–82, Jan. 2009.

J. Widom. Physicochemical studies of the folding of the 100 A nucleosome filament into the 300 A filament: Cation dependence. *Journal of Molecular Biology*, 190(3):411–24, Aug. 1986.

S. Wiesner, K. R. Legate, and R. Fässler. Integrin-actin interactions. *Cellular and Molecular Life Sciences*, 62(10):1081–99, May 2005.

L. Wolpert, C. Tickle, P. Lawrence, E. Meyerowitz, E. Robertson, J. Smith, and T. Jessell. *Principles of Development*. Oxford University Press, Oxford, 4th edition, 2011.

H. J. Worman and G. Bonne. "Laminopathies": a wide spectrum of human diseases. *Experimental Cell Research*, 313(10):2121–33, June 2007.

M. a. Wozniak and C. S. Chen. Mechanotransduction in development: a growing role for contractility. *Nature reviews. Molecular cell biology*, 10(1):34–43, Jan. 2009.

J. Xu, M. M. Zutter, S. A. Santoro, and R. A. Clark. A three-dimensional collagen lattice activates NF-kappaB in human fibroblasts: role in integrin alpha2 gene expression and tissue remodeling. *The Journal of Cell Biology*, 140(3):709–19, Feb. 1998.

Y. Yamanaka, A. Ralston, R. O. Stephenson, and J. Rossant. Cell and molecular regulation of the mouse blastocyst. *Developmental Dynamics*, 235(9):2301–14, Sept. 2006.

Q. Ye and H. J. Worman. Interaction between an integral protein of the nuclear envelope inner membrane and human chromodomain proteins homologous to Drosophila HP1. *The Journal of Biological Chemistry*, 271(25):14653–6, June 1996.

M. Yoshida, M. Kijima, M. Akita, and B. Teruhiko. Potent and Specific Inhibition of MammalianHistone Deacetylase Both in Vivo and in Vitro by Trichostatin A. *The Journal of Biological Chemistry*, 265 (28):17174–17179, 1990.

K. G. Young and R. Kothary. Spectrin repeat proteins in the nucleus. *BioEssays*, 27(2):144–52, Feb. 2005.

M. Zernicka-Goetz, S. a. Morris, and A. W. Bruce. Making a firm decision: multifaceted regulation of cell fate in the early mouse embryo. *Nature reviews. Genetics*, 10(7):467–77, July 2009.